Alma Mater Studiorum - Università di Bologna

School of Science
Department of Physics and Astronomy
Master Degree Programme in Astrophysics and Cosmology

Constraining the magnetic field in the galaxy cluster Abell 2142 using MeerKAT L-band polarisation data

Graduation Thesis

Presented by:

Annalisa Pagliotta

Supervisor:

Prof.ssa
Annalisa Bonafede

Co-supervisor:

Dott.
Christopher J. Riseley

Academic year 2023-2024
Graduation date III

Abstract

Magnetic fields are ubiquitous in the Universe, from the smallest objects to the largest gravitationally bound systems known, galaxy clusters. Cosmological simulations predict that structure formation can be responsible for small-scale dynamo amplification of primordial seed magnetic fields (e.g. Vazza et al., 2014) and that subsequent accretion-driven turbulence and shocks dissipate part of their energy into the (re-)acceleration of relativistic electrons and the further amplification of magnetic fields in galaxy clusters (e.g. Botteon et al., 2022). Magnetic fields have relevant implications on the thermodynamical properties of galaxy clusters, but the level of amplification through compression and dynamos is still unknown, as there are few clusters for which the magnetic field is well constrained. **Thus, the aim of this thesis is to use new observations to study the magnetic field in Abell 2142 galaxy cluster**.

The intracluster medium (ICM), that fills much of the cluster volume, is a hot ($10^7 - 10^8$ K), rarefied ($10^{-4} - 10^{-2}$ cm^{-3}) and magnetised plasma. Consequently, the linearly polarised emission from radio galaxies embedded in the cluster or behind it experiences an effect known as *Faraday rotation* as it passes through the ICM: the polarisation angle of the radiation will rotate by a quantity called *Rotation Measure* (RM), where RM $\propto \int_{\rm LOS} n_e B_\parallel {\rm d}l$. Intensities of few μG are measured in the center of these objects, with values exceeding ~ 10 μG in relaxed cool-core clusters (e.g. Vacca et al., 2012), and decreasing down to fractions of μG in the periphery.

Abell 2142 (A2142) is a massive cluster with $M_{500} = (8.8 \pm 0.2) \times 10^{14}$ M$_\odot$, located in the Local Universe at redshift $z = 0.0894$. Studies carried out with both X-ray telescopes (e.g. Rossetti et al., 2013) and radio interferometers (e.g. Riseley et al., 2024) have demonstrated in recent years the disturbed nature of this object, that shows evidence of both a past intermediate-mass-ratio merger and minor mergers. Therefore, A2142 has been catalogued as a *warm-cool-core* cluster (Markevitch et al., 2000).

The aim of this work is to study the magnetic field (MF) properties of A2142, by performing RM analysis on background and cluster polarised synchrotron sources. We present here high-sensitivity MeerKAT L-band (1283 MHz) data in polarisation, to which we have applied the RM synthesis technique in order to reconstruct the Faraday dispersion function cubes.

Our analysis reveals a bubble-like structure seen in projection in the north-east of the cluster, which has no diffuse Stokes I counterpart and seems to be associated to the Milky Way interstellar medium. Therefore, we have referred it as 'Galactic bubble' throughout the rest of the work. The RM of the radio galaxies displays gradients according to the different intensity and orientation of the MF along the LOS and a patchy appearance. The extracted average RM module, $|\langle {\rm RM} \rangle|$, decreases as a function of the projected distance from the cluster center, suggesting that the MF becomes less intense toward larger distances. Only the central source presents lower values in $|\langle {\rm RM} \rangle|$ than expected, possibly explained by its position in the cluster and by the local contribution of the source evident from the Faraday spectrum. We find that the radial trend of the RM dispersion, $\sigma_{\rm RM}$, shows $100s$ rad m^{-2} in the central regions, declining down to $10s$ rad m^{-2} in the periphery, in line with other clusters (e.g. Stuardi et al., 2021). At the cluster periphery, two sources show a lower values of the RM dispersion, possibly due to fluctuations in the MF spectrum. An additional check has been performed by using the X-ray surface brightness map as a proxy of the gas number density distribution. $\sigma_{\rm RM}$ becomes shallower in the external regions, where the medium is expected to be more diluted. Finally, the fractional polarisation radial

profile confirms that radio galaxies near the cluster center suffer higher depolarisation than peripheral ones as may be found in literature (e.g. Osinga et al., 2022). All these trends are consistent with a magnetic field profile that decreases with increasing distance from the cluster center.

We compare the RM dispersion profiles with mock RM maps obtained with 3D simulations, assuming a 3D gas density model for NCC clusters found by Ghirardini et al., 2019 and a 3D magnetic field model from the post-merger power spectrum (ID E1) derived by Domínguez-Fernández et al., 2019. We left free to vary two parameters out of six available, namely $\Lambda_{max} = [50, 470, 940]$ kpc and $B_{norm} = [0.7, 1.0, 1.5, 3.0]$ μG, and set the resolution of the simulations at 3.4 kpc in order to match the observations. None of the simulated mean radial profiles perfectly fits the observed values, suggesting that our model it is too simplistic. By computing the reduced χ^2 as in Govoni et al., 2006 for $\sigma_{\rm RM}$, we found that a magnetic field tangled on scales between 7 and 470 kpc, following a power spectrum with a peak at $\sim$ 199 kpc, best describes our data with a mean central magnetic field of 8.9 ± 3.2 μG and $\eta = 0.5$. The average magnetic field in 1 Mpc^3 volume, $\langle B_{\rm 1Mpc^3} \rangle$, is $\sim$ 2.6 μG, whereas the one within 1.2 Mpc is higher with respect to the equipartition estimate. This suggests that the assumption of equipartition cannot be made in the case of A2142 galaxy cluster.

Future perspectives include the exploration of other power spectra taken from simulations. In the end, the average central magnetic field intensity does not allow us to rule out a potential hadronic origin of the radio mini-halo, H1, in A2142.

Contents

Chapter 1

Galaxy Clusters

1.1 Introduction

In the currently adopted Cold Dark Matter cosmological model (ΛCDM), the formation of structures is driven by the growth and the consequent gravitational collapse of primordial small-density fluctuations generated in the final stages of an early inflationary epoch. According to the latter assumption, the small objects, in terms of size and mass, form first and their hierarchical mergers and accretion, guided by gravity and dark matter, give rise to the observed galaxy clusters (Kravtsov & Borgani, 2012). The latter ones are, in fact, the largest gravitationally bound and virialised objects in the Universe, with masses of the order of $10^{14} - 10^{15}$ $M_{\odot}$ and virial radii of $1 - 3$ Mpc. Located at the nodes of the Cosmic Web filaments, galaxy clusters are useful tools to test the evolution of structures over time and, combined with other observational constraints, to probe the most accurate cosmological theory that describes the evolution of our Universe from the Big Bang to nowadays (for a review, see Allen et al., 2011 and references therein).

The first studies conducted by Zwicky on the Coma Cluster in 1933 led to the discovery of a ~ 400 factor of difference between the estimated mass through the velocity dispersion of galaxies and the one derived on the basis of luminous matter observations (Zwicky, 1933). This fact suggested the astronomer to postulate for the first time the existence of an additional component which explains the computed discrepancy, the so-called *dark matter* (DM). Today, it is known to be the major constituent of galaxy clusters with a percentage of $\sim 80\%$, followed by the baryonic matter ($\sim 20\%$; e.g. Ettori & Fabian, 1999; Lin et al., 2003). The latter is composed mainly by:

- the intracluster medium (ICM), hot rarefied gas with temperatures of $10^7 - 10^8$ K and average electron density of 10^{-3} cm^{-3} (Felten et al., 1966; Bahcall, 1999). As the gas falls into the DM potential well, the kinetic energy acquired during the collapse is converted into thermal energy via adiabatic compression and shocks; then, the gas settles into hydrostatic equilibrium and its temperature approaches values close to the virial ones (Gunn & Gott, 1972; Sarazin, 1988);

- $100s - 1000s$ of galaxies. The overall density of the medium determines the population of galaxies in clusters: lenticular (S0) and elliptical morphological types are commonly distributed in high-density environments, e.g. the core of clusters; conversely, spiral and irregular galaxies tend to be located in low-density regions. This trend is also known as the *morphology-density relation* (Oemler, 1977; Dressler, 1980). For this reason, clusters can be classified depending on their galactic content as *elliptical-rich*, e.g. Coma cluster, *spiral-poor* and *spiral-rich*, e.g. Virgo cluster (Bahcall, 1999).

Fig. 1.1 shows an example of galaxy clusters main baryonic constituents.

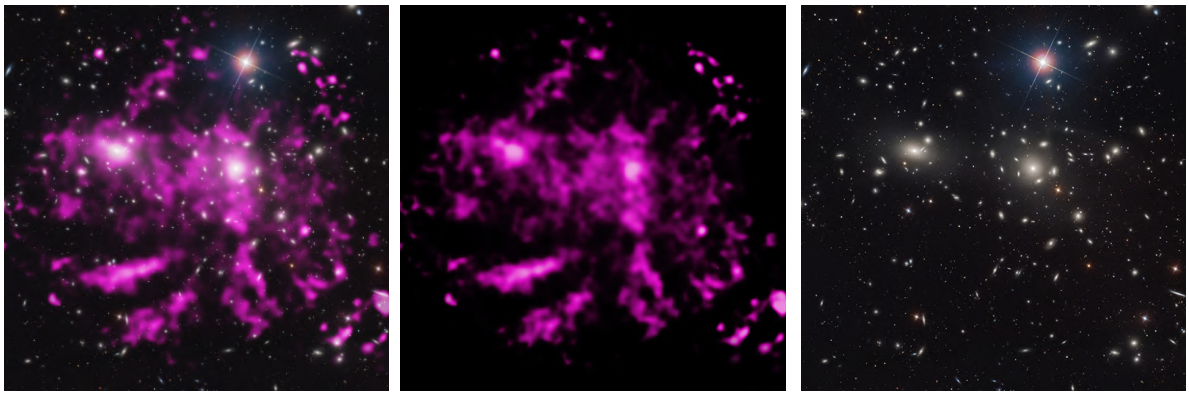

(a) **(b)** **(c)**

Figure 1.1: The Coma cluster. *Panel (a):* composite emission from ICM (*pink*) and from galaxies (*red, green, blue*). *Panel (b):* X-ray emission only. *Panel (c):* optical emission only (X-ray: NASA/CXC/MPE from Sanders et al., 2013; Optical: SDSS).

1.2 Multi-wavelength Emission in Galaxy Clusters

Given the multi-component nature of galaxy clusters and the interaction of every element with the surrounding structures and environment, galaxy clusters can be observed at different wavelengths.

The X-ray energies (Sec. 1.2.1) are dominated by the radiation produced by the hot ICM, whereas the stellar emission from galaxies comes out in the UV, optical and near-infrared bands (NIR; Sec. 1.2.2). At millimeter wavelengths (Sec. 1.2.3) is appreciable the distortion of the CMB spectrum that is caused by the photons interaction with the cluster hot gas, while the relativistic electrons contribute mostly in the low-energy part of the electromagnetic spectrum via radio synchrotron radiation (Sec. 1.2.4). The latter non-thermal component will be discussed in details in Chapter 2 since it represents the founding radiative process of this thesis.

Finally, even if it is not considered as a proper emission mechanism, the gravitational lensing of background sources light could help in determining cluster masses and consequently in the estimate of the DM amount (for a review, see Bartelmann, 2010).

1.2.1 X-ray Thermal Emission

As mentioned before, galaxy clusters are permeated by a hot low-density plasma, which emits in the X-ray energy band due to both continuum and line emission processes. The dominant emission process is the Bremsstrahlung or *free-free* emission, i.e. radiation produced by the acceleration and deflection of charges (e.g. electrons) in the Coulomb field of atomic nuclei (e.g. ions) (Rybicki & Lightman, 1986). Other mechanisms characterising the X-ray spectrum of galaxy clusters are the recombination, *free–bound* transition caused by the capture of an electron by an ion, and the de-excitation of an electron, *bound–bound* transition into a lower quantum level of the same atomic nucleus. Moreover, an exception is the continuum radiation produced by the decay of an electron from the $2s$ to the $1s$ state, which is completely forbidden by the angular momentum conservation, but can occur in low density environments as a very slow two-photon process[1] (Böhringer & Werner, 2010). All these mechanisms are summarised in Fig. 1.2, which displays the X-ray spectra for solar abundance at different plasma temperatures.

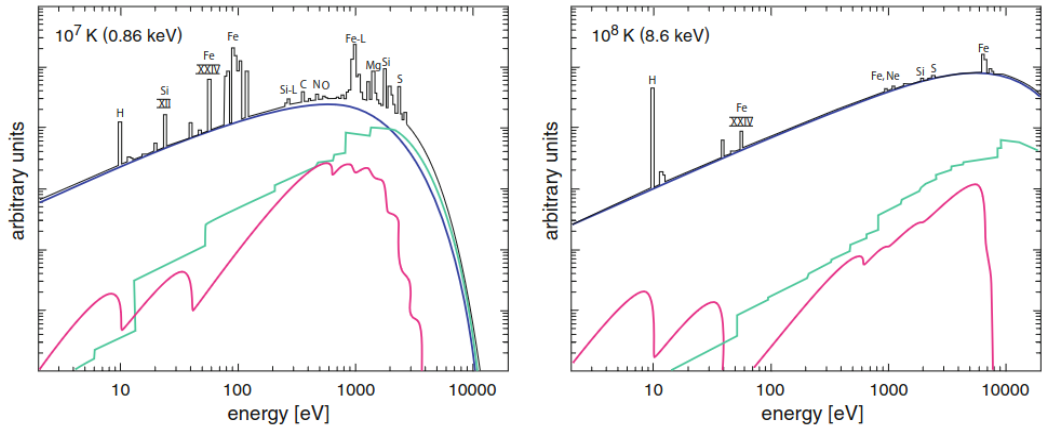

Figure 1.2: Theoretically calculated X-ray spectra for solar abundance at different plasma temperatures (from *left* to *right*: 10^7 and 10^8 K). The continuum contributions are from Bremsstrahlung (*blue*), recombination radiation (*green*) and 2-photon radiation (*red*). The major emission lines (*black*) are indicated with the elements from which they originate (from Böhringer & Werner, 2010).

As it is possible to observe, the spectral features are less prominent at the highest temperatures, where Bremsstrahlung is the dominant emission. In the case of thermal equilibrium, the velocities of the particles follow the *Maxwell-Boltzmann distribution*[2] and, as the shape of the X-ray spectrum is determined by the temperature and by the chemical composition of the plasma, this mechanism acquires the appellation of

[1] this 'two-photon radiation' involves a distribution function of the ratio of the two electrons energies and thus gives rise to continuum radiation (for details, see Spitzer & Greenstein, 1951).

[2] $\mathrm{d}P \propto v^2 e^{-m_e v^2/2k_B T_g} \mathrm{d}v$, where v is the velocity of the particles, m_e is the electron mass, k_B is the Boltzmann constant and T_g is the gas temperature.

thermal. The Bremsstrahlung specific emissivity, ϵ_ν^{ff}, at a given gas temperature, T_g, is defined as the emitted energy per unit frequency, ν, and volume, V,

$$\epsilon_\nu^{ff} = \frac{\mathrm{d}E}{\mathrm{d}t\mathrm{d}V\mathrm{d}\nu} = 6.8 \times 10^{-38} Z^2 n_e n_i T_g^{-1/2} e^{-h\nu/kT_g} \bar{g_{ff}}(T_g, \nu) \quad \frac{\mathrm{erg}}{\mathrm{s\ cm^3\ Hz}}, \tag{1.1}$$

where Z is the ion effective charge, n_e and n_i are respectively the ions and electrons number density and $\bar{g_{ff}}(T_g, \nu)$ is the average Gaunt factor, which corrects for quantum mechanical effects (Sarazin, 1988). By integrating over the X-ray emission energy range, the gas distribution and the cluster volume, the typical X-ray luminosity of galaxy clusters is $L_X \sim 10^{43} - 10^{45}$ erg s^{-1}.

The Bremsstrahlung spectrum is then characterised by a flat trend (neglecting the self-absorption at low frequencies) with a sharp cut-off occurring at the higher energies, which reflects the exponential term in eq. 1.1. When detected, the latter component can be used for the ICM temperature estimate. Regarding the chemical composition of the plasma, the abundances of the metals can be derived from the intensity of the lines. Observations have shown that the ICM of local clusters has an average metallicity of ~ 0.3 Z$_\odot$ (De Grandi & Molendi, 2001) and the most prominent signature is the Fe line at 7 keV (Mitchell et al., 1976). Moreover, the relative abundance ratio gives a clue to the elements origin: the lightest ones, C and N, come primarily from winds of asymptotic giant branch (AGB) stars, the $\alpha-$elements from *core-collapse* supernovae (SNe), while the primary products of SNe *type Ia* (thermonuclear explosions of white dwarf stars) are Fe and Ni (Böhringer, 2014).

The cooling time due to thermal Bremsstrahlung depends on the electron number density, n_e, and on the gas temperature, T_g, as

$$t_{cool} \approx 8.5 \times 10^{10} \left(\frac{n_e}{10^{-3}\ \mathrm{cm^{-3}}}\right)^{-1} \left(\frac{T_g}{10^8\ \mathrm{K}}\right)^{1/2} \mathrm{yr}. \tag{1.2}$$

It is on average longer than the age of the Universe, but at the center of some clusters the high n_e and the low T_g can cause the cooling process to be faster (e.g. $t_{cool} < t_H$), thus these objects are believed to host a *cool-core* (see Sec. 1.4.1). This timescale is also longer than the sound crossing time, i.e. the time required for a sound wave to cross a cluster with diameter D,

$$t_s \approx 6.6 \times 10^8 \left(\frac{D}{\mathrm{Mpc}}\right) \left(\frac{T_g}{10^8\ \mathrm{K}}\right)^{-1/2} \mathrm{yr}, \tag{1.3}$$

leading to consider an hydrostatic gas distribution. Moreover, the galaxies are assumed to be in equilibrium with the plasma in the cluster gravitational potential, $\phi(r)$, and to have an isotropic velocity dispersion, σ_r. The gas and galaxies radial distribution,

n_{gas} and ρ_{gal}, can be directly related via the equilibrium equations

$$\frac{1}{n_{gas}}\frac{\mathrm{d}((kT/\mu m_p)n_{gas})}{\mathrm{d}r} = -\frac{\mathrm{d}\phi(r)}{\mathrm{d}r} = \frac{1}{\rho_{gal}}\frac{\mathrm{d}(\sigma_r^2\rho_{gal})}{\mathrm{d}r}, \tag{1.4}$$

that bring to

$$\frac{n_{gas}(r)}{n_{gas}(0)} = \left[\frac{\rho_{gal}(r)}{\rho_{gal}(0)}\right]^{\beta}. \tag{1.5}$$

The exponent β is represented by the ratio of their energies per unit of mass

$$\beta \equiv \frac{\mu m_p \sigma_r^2}{kT_g} = 0.76 \left(\frac{\sigma_r}{10^3 \text{ km s}^{-1}}\right)^2 \left(\frac{T_g}{10^8 \text{ K}}\right)^{-1}, \tag{1.6}$$

where μ is the mean molecular weight and m_p is the proton mass (Sarazin, 1988; Arnaud, 2009). Under these hypotheses and by assuming the King, 1962 analytic approximation to the isothermal sphere, the gas density distribution can be described with the β-model (Cavaliere & Fusco-Femiano, 1976, 1978)

$$n_{gas}(r) = n_{gas}(0)\left[1+\left(\frac{r}{r_c}\right)^2\right]^{-3\beta/2}, \tag{1.7}$$

and, consequently, the X-ray surface brightness profile as

$$S_X(R) = S_X(0)\left[1+\left(\frac{R}{r_c}\right)^2\right]^{-3\beta+1/2}, \tag{1.8}$$

where r_c is the core radius and R is the projected radius (Gorenstein et al., 1978). This model is a good description of the observed profiles with a typical value for β of $\sim 2/3$ (Jones & Forman, 1978). In the end, the ICM density and temperature radial profiles derived from X-ray observations are one of the most used tools to constrain the gas mass in galaxy clusters.

1.2.2 UV, Optical and NIR Emission

The UV, optical and NIR emission observed in clusters come from the cluster member galaxies, whose colors reflect their dominant stellar populations and thus correlate with their morphology (Hubble, 1936). As mentioned in Sec. 1.1, galaxies in clusters are divided in *early-* (e.g. ellipticals and S0s) and *late-types* (e.g. spirals and irregulars) according to the morphology-density relation. The former ones are particularly massive (up to few 10^{12} $M_\odot$), show red colors and evolve passively, i.e. star formation is quenched. In contrast, the latter ones present a disky or an irregular structure and display bluer colors that indicate ongoing star formation. As a consequence, the *color-magnitude relation* of galaxy clusters is characterised by a bimodal distribution (Strateva et al., 2001).

Galaxy spectra are typically characterised by a strong continuum component caused by the combination of stellar *blackbody emission* and by the presence of absorption and emission lines. For ellipticals and S0s, the main spectral features are the Balmer/4000Å break, the Ca H & K (3934Å and 3969Å), Mg (5175Å) and Na (5894Å) absorption lines, which are produced by the metals and the molecules found in old stars atmospheres and by the deficiency of hot, blue stellar types. On the other hand, spiral and irregular galaxies include emission lines, such as the [OII] (3737Å), the [OIII] (4959Å and 5007Å) doublet, the Hα-[NII] complex and the Balmer series (6563Å, 4861Å, ...). All of them are explained by the ongoing star formation and by the young OB stellar population which ionise the surrounding interstellar medium (ISM) (Kennicutt, 1992).

Finally, galaxy clusters contain a population of stars that are not members of individual galaxies, but are bound to the cluster potential and produce diffuse intracluster light (ICL). This component comprises between 5% and 50% of the total optical luminosity (Krick et al., 2006 and references therein).

1.2.3 Thermal Sunyaev-Zeld'ovich Effect

Galaxy clusters interact also with the surrounding environment, especially with the so-called *cosmic microwave background* (CMB), a radiation field that permeates the Universe and is observed at millimiter wavelengths. It is considered as a relic of the Big Bang (Sunyaev & Zel'dovich, 1980) and has a spectrum that is almost a perfect blackbody

$$I_\nu = \frac{2h\nu^3}{c^2}\left(e^{h\nu/kT} - 1\right)^{-1}, \tag{1.9}$$

with a temperature of $T_{\rm CMB} = 2.7260 \pm 0.0013$ K (Fixsen, 2009).

CMB photons passing through the center of a massive cluster have only a $\approx 1\%$ probability of interacting with the ICM electrons and since the latter ones are hotter (i.e. $h\nu << m_e c^2$), the basic process behind the *Sunyaev-Zeld'ovich effect* (SZE; Sunyaev & Zel'dovich, 1972) is the Inverse Compton (IC) scattering. The energy of the CMB photon is boosted by roughly $kT_e/m_e c^2$ causing a small (< 1 mK) distortion in the CMB spectrum (Fig. 1.3a). In this way, the SZE appears as a decrease in the intensity at frequencies < 218 GHz and as an increase at higher frequencies, as it is possible to appreciate from Fig. 1.3b.

The observed distortion of the CMB spectrum is proportional to the thermal electron pressure, P_e, integrated along the line of sight (LOS), that at low frequencies (Rayleigh-Jeans regime) can be approximated as $\Delta I_\nu / I_\nu = -2y$. The term y is the *Compton y-parameter* defined as

$$y \equiv \int_{\rm LOS} n_e \sigma_T \frac{k_B T_e}{m_e c^2} {\rm d}l = \frac{\sigma_T}{m_e c^2} \int_{\rm LOS} P_e {\rm d}l, \tag{1.10}$$

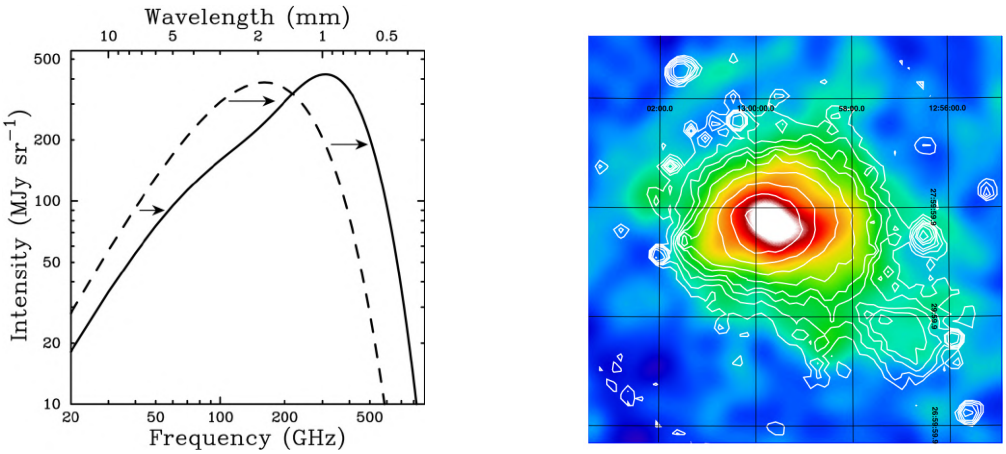

(a) **(b)**

Figure 1.3: *Panel (a):* The CMB spectrum, undistorted (*dashed line*) and distorted by the Sunyaev-Zel'dovich effect (*solid line*) (from Carlstrom et al., 2002). *Panel (b):* Sunyaev-Zel'dovich effect on the Coma cluster (from Planck Collaboration et al., 2011).

where n_e is the electron number density, σ_T is the Thomson cross-section, T_e is the electron temperature, k_B is the Boltzmann constant and $m_e c^2$ is the electron rest mass energy (Carlstrom et al., 2002). This effect is *redshift-independent* and induces spatial secondary anisotropies on arcminute scales (Sunyaev, 1977). The CMB spectrum, combined with the cluster number counts, provides a unique probe of the Universe structure on the largest scales and has been used to measure the clusters gas properties and mass function, as well as some of the global cosmological parameters (for some reviews see Birkinshaw, 1999 and Rephaeli et al., 2006).

1.2.4 Extended Radio Sources and Radio Galaxies

As anticipated, galaxy clusters emission covers the electromagnetic spectrum down to the radio band frequencies, by showing large scale diffuse sources emitting synchrotron radiation up to kpc- and Mpc-scales (for some reviews, see Feretti et al., 2012 and van Weeren et al., 2019). The existence of these structures indicates the presence of both GeV cosmic rays (e.g. electrons) and μG magnetic fields, and is able to trace shocks and turbulence in the ICM, thus the cluster dynamical and evolutionary stage.

Diffuse cluster radio sources are classified depending on their morphology and size and comprise three main groups, *radio halos*, *radio relics* and *mini-halos* (Fig. 1.4). They share some common properties, like not being associated to any optical counterpart, e.g. cluster galaxies, but with the ICM, and having very steep radio synchrotron power-law spectra[3]. In recent years, new observations have discovered that the classification is much more complex, including objects like *mega-halos* (Cuciti et al., 2022), *radio bridges* (e.g. Botteon et al., 2020; Pignataro et al., 2024) and *mini-halo+halos* sources (this thesis; see references in Ch. 3). Since the radiative lifetimes of relativistic

[3] $S_\nu \propto \nu^{-\alpha}$, where ν is the frequency and α is the spectral index (see Sec. 2.1).

electrons due to energy losses (eq. 2.7) are of the order of $\sim 10^8$ yr and the expected diffusion velocity of the same is comparable to the Alfvèn speed[4] (~ 100 km s^{-1}), the distances travelled by relativistic electrons, e.g. from cluster galaxies, are far smaller ($\sim$ pc $-$ kpc) than those observed for radio diffuse sources. The explanations proposed about the possible origin of these electrons are different: the most promising one consists in the re-acceleration of previously energised seed electrons, e.g. by cluster mergers and accretion shocks, or the *in situ* injection by Active Galactic Nuclei (AGN) outflows (e.g. jets) or star-related phenomena (e.g. SNe) occurring in cluster galaxies (e.g. Brunetti et al., 2001); the second scenario is represented by the hadronic model, where radio emitting electrons are produced in the interaction between CR protons and ICM protons (e.g. Dolag & Ensslin, 2000); in this case, observations of gamma-ray photons due to the π^0 decay can be used to confirm this theory and eventually study the contribution of secondary electrons (e.g. Ackermann et al., 2014). Last but not least, radio galaxies embedding the cluster contribute in the total synchrotron budget and their jets polarised radiation can be used to obtain useful information about the cluster magnetic field (see Sec. 2.3).

The main properties of the aforementioned objects are summarised in the following bulleted list:

- **radio halos**: diffuse radio sources of low surface brightness ($\sim 0.1-1$ μJy arcsec^{-2} at 1.4 GHz), permeating the cluster volume with radial extension of 1–2 Mpc; they are typically centrally-located with both regular and irregular morphologies and depolarised down to a few percent level (due to both internal and beam depolarisation; see Sec. 2.1.4); the spectral distribution is patchy with a steepening from the center to the peripheral regions, with spectral indexes ranging between $\sim 1 - 1.5$ (e.g. Feretti et al., 2004); the radio power at 1.4 GHz assumes values between 10^{23} and 10^{26} W Hz^{-1} (e.g. Giovannini et al., 2009) and correlates with the cluster X-ray luminosity (e.g. Govoni et al., 2001); some halos present ultra-steep radio spectra up to $\alpha \sim 2$, thus called *ultra-steep radio halos* (USRHs), indicating an inefficient re-acceleration, that can only be revealed with highly sensitive observations at very low radio frequencies; the corresponding equipartition magnetic field (see Sec. 2.3) has intensities of $\sim 0.1 - 1$ μG (Govoni & Ferretti, 2004). Radio halos are mostly found in merging clusters and the proposed origin of the energetic electrons is based on the turbulent re-acceleration[5] (e.g. Brunetti & Lazarian, 2007); the first ever radio halo has been detected and analysed by Large et al., 1959 65 years ago and the number of confirmed radio halos increases every year thanks to state-of-the-art radio telescopes;

[4] the speed at which magnetic waves propagate through a plasma, defined as $v_A = B/\sqrt{4\pi\rho}$.

[5] based on the *second order Fermi process (Fermi-II)*, a stochastic inefficient process where particles scatter from magnetic inhomogeneities and can both gain and loose energy.

- **radio relics:** diffuse elongated radio sources (arc-like or roundish) with a low surface brightness, similar to radio halos, extending from 0.5 to 2 Mpc, and presenting steep emission spectra ($\alpha \sim 1-1.5$; e.g. de Gasperin et al., 2014), with flatter indexes on the side away from the cluster center, that steepen towards the cluster center; they are located in the cluster peripheral regions and are strongly polarised (with fractional polarisation (eq. 2.9) of $\sim 20-30\%$, in some cases up to 50%; e.g. van Weeren et al., 2010). Relics are mostly found in merging clusters like halos, suggesting that they may be related to major mergers (e.g. van Weeren et al., 2011a); they are expected to come in pairs, as *double relics*, and to be located on opposite sides to the cluster center and perpendicular to the merger axis (e.g. Bonafede et al., 2012). Consequently, selection biases could have an important role. In general, observations of relics indicate the presence of both μG level magnetic fields ($0.5-2$ μG from equipartition estimates, e.g. Ensslin et al., 1997) and relativistic particles in cluster outskirts: the former ones are compressed, where the correspondent vectors result to be aligned parallel to the shock front (e.g. Bonafede et al., 2009), instead the latter ones are accelerated by shock fronts with Mach numbers $\sim 1-3$ (e.g. Ha et al., 2018), following the Diffusive Shock Acceleration (DSA)[6]; deep high-resolution observations have also revealed more details regarding these sources, such as a significant amount of filamentary substructures, possibly originated from the complex shape of the shock surfaces with different Mach numbers (e.g. Rajpurohit et al., 2022);

- **mini-halos:** diffuse roundish radio emission that extends far from the central Brightest Cluster Galaxy (BCG) on a moderate scale ($\sim 100-500$ kpc), thus being considered as a re-scaled down version of radio halos; they have a low surface brightness and a steep spectrum ($\alpha > 1$), as in the case of the previously mentioned radio sources, and present higher volume emissivities (e.g. Murgia et al., 2009). Mini-halos are mostly found in relaxed cool-core clusters and are depolarised for the same reasoning as radio halos; since the emission surrounds the central galaxy, often showing radio lobes, the separation between the AGN and mini-halos can be difficult. Moreover, the origin of mini-halos is still poorly known: Gitti et al., 2002 proposed that they are a consequence of a population of relativistic electrons, possibly injected by the radio BCG and re-accelerated by magneto-hydro-dynamical (MHD) turbulence via Fermi-like processes; this is supported by the correlation observed between the mini-halo radio power and the cooling rate power (Gitti et al., 2004); in some clusters, mini-halos are found to be confined in the cold fronts of cool-core clusters; thus, the gas sloshing[7]

[6] based on the *first order Fermi process (Fermi-I)*, an efficient process where particles gain energy by crossing multiple times a shock front thanks to the magnetic field acting as a mirror.

[7] relative motion of low entropy core gas with respect to the DM-dominated cluster potential that

may generate turbulence in the core and be responsible for the formation of both structures (e.g. Giacintucci et al., 2014). As for radio halos, the electrons could be of secondary origin following the hadronic model (e.g. Pfrommer & Enßlin, 2004); as a consequence, the gamma-ray upper limit can be turned into a lower limit on the magnetic field strength needed to generate the radio emission; future all-sky surveys with the Square Kilometre Array (SKA) will be able to detect up to ~ 330 mini-halos in clusters out to $z \sim 0.6$ (Gitti, 2016);

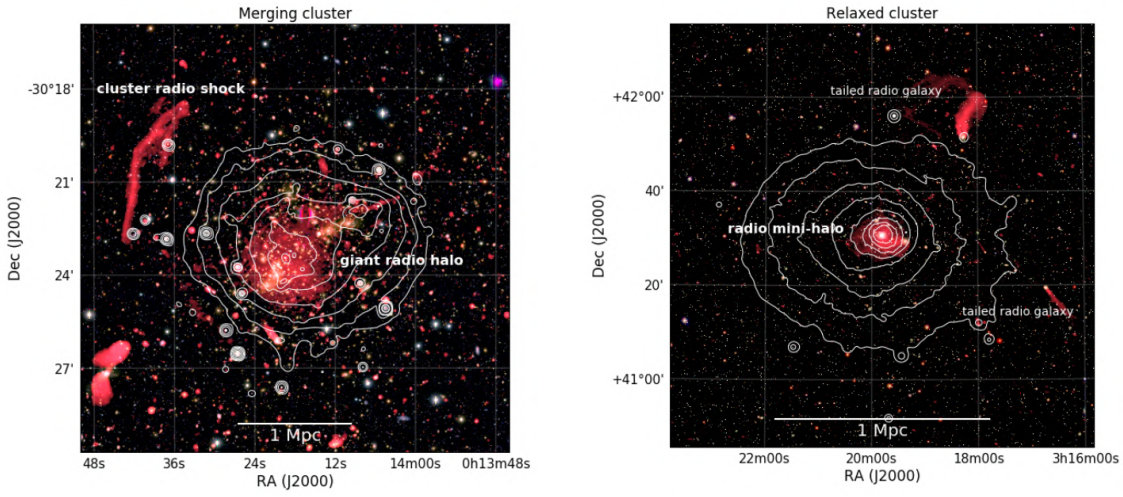

(a) **(b)**

Figure 1.4: Diffuse radio emission in galaxy clusters. *Panel (a):* VLA 1–4 GHz image of the galaxy cluster Abell 2744 with a giant radio halo and a radio shock (*red*). *Chandra* X-ray surface brightness contours are shown in *white* (from Pearce et al., 2017). *Panel (b):* VLA 230–470 MHz image of the Perseus cluster with a mini-halo (*red*). *XMM-Newton* X-ray contours in the 0.4–1.3 keV band are overlaid in *white* (from Gendron-Marsolais et al., 2017).

- **radio galaxies:** the galaxies found in clusters often host an AGN that emits radio synchrotron radiation in form of jets and lobes, thus called *radio galaxies*; these sources are generally classified depending on their morphology according to the Fanaroff & Riley, 1974 classification in FRI and FRII radio galaxies and extend for hundreds of kpc, well beyond the host galaxy. A major difference with the ones found outside the clusters is that the jets and lobes often show signs of interaction with the ICM: the ram pressure, $p = \rho v^2$, of the intracluster gas is able to change the appearance of the radio galaxies by bending and curving the jets. In this way, new categories of objects take form, first mentioned by Ryle & Windram, 1968 and Owen & Rudnick, 1976: *wide-angle-tail* (WAT) and *narrow-angle-tail* (NAT) radio galaxies, classified depending on their luminosity and the degree of bending, and the *head-tail* radio galaxies, where the radio jets appear to be bended in a common direction, resembling a 'tail', with the luminous host galaxy acting as the 'head'.

meets the higher entropy gas at larger radii; in general, caused by a minor merger or an off-center passage.

1.3 Magnetic Fields in Galaxy Clusters

Magnetic fields (MF) are ubiquitous in the Universe, from the smallest objects like atoms to the largest structures as filaments and voids (e.g. Beck et al., 2012; Carretti et al., 2022). Nowadays, it is well known and accepted that magnetic fields permeate the galaxy clusters volume with μG intensities up to Mpc-scales (for some reviews, see Govoni & Ferretti, 2004 and Feretti et al., 2012). The study of this non-thermal component is relevant to understand the physics and energetics in the clusters environment, since magnetic fields provide an additional term of pressure and are crucial in the thermodynamics of the ICM. As mentioned in Sec. 1.1, the latter one is a hot, dilute plasma in which the *mean free path* of the particles, λ_{mfp}, is several orders of magnitude higher than the *gyroradius*, $r = mv_{\perp}/|q|B$. This aspect has significant consequences on the thermal conduction (e.g. Malyshkin, 2001; Roberg-Clark et al., 2016), that happens to be highly anisotropic and suppressed in the direction perpendicular to the magnetic field orientation, even if its intensity is relatively weak. Moreover, magnetic fields play an important role in the acceleration of the particles, in the diffusion of cosmic rays and in the formation of the aforementioned diffuse large scale structures.

Since magnetic fields cannot be measured directly, their presence is well demonstrated by radio observations and the intensity and distribution are estimated and determined through different techniques (Sec. 2.3): from the study of cluster diffuse radio sources (e.g. halos, relics and mini-halos) to Faraday Rotation Measures of polarised radio galaxies located inside or behind galaxy clusters, and eventually adopting simulations (see Ch. 5). Intensities from 5-10 μG are measured in the center of these objects (e.g. Vogt & Enßlin, 2003; Bonafede et al., 2010), with values exceeding 10s μG in the core of cool-core clusters (e.g. Vacca et al., 2012), and decreasing down to fractions of μG in the periphery. The origin of magnetic fields is still an open question and cosmological simulations predict that structure formation, accretion and merger-driven shocks and turbulence are able to compress and amplify seed magnetic fields and (re-)accelerate relativistic electrons (Botteon et al., 2022 and reference therein) (see Sec. 1.3.1). The level of amplification is poorly known, as the magnetic field is well constrained with state-of-art techniques in few clusters. These and other open questions will be the main research topic and goal for future radio telescopes, like SKA (e.g. Johnston-Hollitt et al., 2015).

1.3.1 Magnetic Field Origin and Amplification

The origin of the magnetic fields observed in galaxy clusters is still debated and very little is known about their amplification and evolution (for some reviews, see Ryu et al., 2012 and Donnert et al., 2018). The ICM is considered as a nearly *perfect*, high β *plasma* ($\approx$ 100, i.e. the thermal pressure dominates over the magnetic field

pressure), thus the conductivity, σ, is very high and the diffusivity is very low ($\eta \approx 0$). As a consequence, the *induction equation*

$$\frac{\partial \vec{\mathbf{B}}}{\partial t} = \nabla \times (\vec{\mathbf{v}} \times \vec{\mathbf{B}}) - \eta \nabla \times (\nabla \times \vec{\mathbf{B}}), \tag{1.11}$$

which expresses how the magnetic field, $\vec{\mathbf{B}}$, evolves as a function of time with the flow velocity, $\vec{\mathbf{v}}$, predicts that magnetic fields are 'frozen' into the plasma and are advected with the bulk motions of the medium. Because eq. 1.11 represents the conservation equation for the magnetic flux, the magnetic field in galaxy clusters cannot be created *in situ*, but have to be seeded and then amplified by some mechanisms, also at high redshift, to explain the values and the scales observed in local clusters.
Different scenarios have been proposed for the magnetic fields origin in galaxy clusters. They can be primordial, i.e. generated in the Early Universe before the recombination (for some reviews, see Durrer & Neronov, 2013 and Subramanian, 2016), during the first-order phase transitions, such as the *quark-hadron* and the *electro-weak* transitions (e.g. Kahniashvili et al., 2013), or during the inflation, where electromagnetic quantum fluctuations are amplified (e.g. Giovannini & Shaposhnikov, 2000). The presence of magnetic fields in the Early Universe might be detectable through their effect on the Big Bang nucleosynthesis as proposed by Cheng et al., 1996 and on the CMB radiation. Current observations of anisotropy (high-order fluctuations and non-Gaussianity) in the CMB place weak upper limits of $B < 5 \times 10^{-9}$ G on scales of $\sim$ Mpc (Ade et al., 2016). In addition, the analysis of the inhomogeneities in the matter distribution of the Universe with the *Faraday rotation effect* (Sec. 2.1.3) of distant quasars (QSOs) put limits of $B < 10^{-9} - 10^{-8}$ G (e.g. Blasi et al., 1999).

The second proposed scenario is that magnetic fields are generated in later epochs of the Universe history, i.e. astrophysical origin, through mechanisms such as the *Biermann battery effect*[8] associated with the epoch of the *re-ionisation* (e.g. Gnedin et al., 2000), or generated by the first stars (e.g. Xu et al., 2008), and/or by the (proto-)galaxies (e.g. Beck et al., 2013), and then injected in the interstellar and intergalactic medium by galactic outflows and SNe explosions (e.g. Donnert et al., 2009) or AGN (e.g. Xu et al., 2011). Magnetic fields could be also produced by ionisation fronts around the first stars (e.g. Langer et al., 2005).
A commonly accepted hypothesis is that the values and the scales of the magnetic fields observed in local clusters result from the amplification of weaker pre-existing seed fields via compression and small-scale dynamo mechanism driven by shocks and turbulence, that are injected during structure formation, accretion and merger events (e.g. Roettiger et al., 1999; Ryu et al., 2008; Iapichino & Brüggen, 2012; Botteon

[8] which occurs when the gradients of the electron pressure and the number density are not parallel, thus electrostatic equilibrium is no longer possible. This leads to a thermo-electric current which generates an electric field (and a corresponding magnetic field) that restores force balance.

et al., 2022). Other possible ways to amplify magnetic fields comprise the compression at shocks, small-scale core sloshing in relaxed systems following a minor merger and CR-driven dynamo.

As mentioned above, under the ideal MHD approximation, the magnetic field flux in clusters is conserved and leads to the scaling of the magnetic field intensity with the density, ρ, as

$$B(\rho) = B(z_*)\Big(\frac{\rho}{\langle\rho\rangle}\Big)^{2/3}, \tag{1.12}$$

where $\langle\rho\rangle$ is the average density and z_* is the redshift at which the seed field is injected. Thus, galaxy clusters with overdensities of $\Delta = \rho/\langle\rho\rangle \approx 100$ might present amplified magnetic fields by a factor of ~ 20 through adiabatic compression within the virial radius. Cosmological simulations at central cluster overdensities ($\rho/\langle\rho\rangle \approx 1000$) with seed fields of the order of $10^{-13} - 10^{-12}$ G (at $z_* = 20$; Dolag et al., 2005, 2008) show that the magnetic field intensity reaches $\sim 10^{-2}$ μG in the cores, suggesting that the adiabatic compression of the gas is not enough, and other mechanisms, such as the small-scale dynamo, contribute to the amplification of the magnetic field.

Following the Kolmogorov, 1991 picture, turbulence injected by mergers starts *super-Alfvénic* on the largest scales (i.e. the magnetic field is not dynamically important and the field topology is shaped by the fluid motion) and breaks down into smaller eddies transferring kinetic energy (i.e. an *energy cascade*), until the latter one becomes comparable to the viscous forces. Again, for the magnetic flux conservation, the stretching and the folding of pre-existing magnetic field lines by a random velocity field trigger the so-called *small-scale dynamo* in correspondence of the viscous scale: it amplifies exponentially the magnetic field energy in an *inverse cascade* starting from the smallest scales and pushes the magnetic field components toward larger scales, until the magnetic field back-reacts to the flow at equipartition (i.e. where the magnetic field energy is comparable to the turbulent kinetic energy). Moreover, this process should take almost ≈ 1000 yr to happen and starts only after merger events, since the turbulence injected by the most energetic ones takes even ~ 1 Gyr to cascade from the largest to the smallest scales (Beresnyak & Miniati, 2016). In addition, there are some evidences that high redshift galaxy clusters could have similar magnetic field strengths to local galaxy clusters (e.g. Di Gennaro et al., 2020), implying that magnetic fields are amplified rapidly during cluster formation and loose memory of the original seed field. Finally, as pointed out by Domínguez-Fernández et al., 2019, the magnetic field amplification in galaxy clusters is a result of a more complex scenario, characterised by the combined effect of adiabatic compression and the presence of small-scale dynamo, both driven by minor and major mergers.

In general, high-resolution MHD cosmological simulations are adopted and implemented to study the amplification of magnetic fields during galaxy clusters formation

and evolution (e.g. Bonafede et al., 2011; Vazza et al., 2014, 2017). They start from initial seed fields of $\sim$ nG at high redshift and predict μG−level intensities consistent with equipartition estimates and Faraday rotation measures. Vazza et al., 2018 analysed different models for the origin and amplification of extragalactic magnetic fields extending the study to filaments and voids. Fig. 1.5 shows the predicted present-day distribution of extra-galactic magnetic fields intensity resulting from cosmological MHD simulations and the regime in which different observational methods can probe them and discriminate over the possible magnetogenesis scenarios.

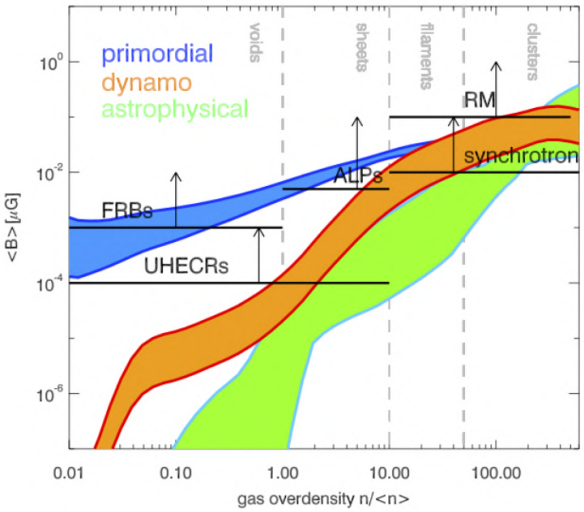

Figure 1.5: Distribution of extra-galactic magnetic fields as a function of the gas overdensity for clusters, filaments, sheets and voids (*grey*). Primordial (*blue*), dynamo (*orange*) and astrophysical (*green*) models are reported with the correspondent magnetic field regime probed by different observational methods in *black* (from Vazza et al., 2018).

1.4 Galaxy Clusters Classification

1.4.1 Cool-core Galaxy Clusters

Dynamically relaxed galaxy clusters (i.e. that are not experiencing a merger or have not undergone a merger in the past few Gyr) present a symmetrical distribution of the X-ray surface brightness with a well defined peak of emission in correspondence to center of the core. The latter region shows in general higher values of the gas number density ($\sim 10^{-2} - 10^{-1}$ cm^{-3}; e.g. Hudson et al., 2010) with respect to the global profile[9], implying cooling times (eq. 1.2) $t_{cool} \lesssim 1$ Gyr, smaller than the Hubble time. Such efficient process is also reflected by the temperature drop in the inner part ($< 1 - 2$ keV; e.g. Vikhlinin et al., 2005). Therefore they are called *cool-core* (CC) galaxy clusters (Molendi & Pizzolato, 2001). In addition, such kind of clusters shows strongly peaked metallicity profiles, with roughly solar abundances outside the central

[9]usually fitted with a double β-model (eq. 1.7; see e.g. Henning et al., 2009).

regions (e.g. De Grandi & Molendi, 2001). All these observations brought to the development of the well-known *cooling flow* (CF) model (e.g. Fabian, 1994), where hot gas from the outer regions of the ICM flows inward to re-establish the pressure support lost by the cool dense core. This model predicts large amounts of deposited cold gas in the range $100 - 1000$ $M_\odot$ yr^{-1} (e.g. Peres et al., 1998), with consequent high star formation, Hα luminosity and multi-phase gas down to the molecular regime.

Observations carried out throughout the years have shown that the star formation rate is only a small fraction of the predicted one (e.g. Rafferty et al., 2008) and the molecular gas detected by CO line emission is at least 20 times lower than expected (e.g. Edge, 2001). Moreover, far less cooling gas is detected below $1 - 2$ keV in rich clusters (e.g. Kaastra et al., 2001), suggesting that the gas in the central regions is not cooling at the rate predicted by the traditional CF model (only $\sim 1 - 10$ %; e.g. Peterson et al., 2003). To explain this scenario, a heating mechanism has been proposed to compensate for the radiative losses. A possible mechanism consists mainly in mechanical energy released by a radio source found in the center of these objects, e.g. an AGN (e.g. McNamara & Nulsen, 2007): outbursts and jet-driven shocks inflate bubbles, the so-called *X-ray cavities*, heating and displacing the gas and preventing the latter to cool down to very low temperatures in clusters cores. Nevertheless, the details on the exact regulation and timescales of the AGN feedback remain unclear till nowadays (e.g. Ubertosi et al., 2023).

As an example, one of the first ever studied cases of CC galaxy clusters is that of the *Perseus cluster* (Abell 426), which presents peculiar structures as shown in Fig. 1.6a. These features are in the form of cold fronts[10] seen as bright spiral-like loops, bay-like regions of hot gas and quasi-circular ripples interpreted as sound waves generated by the cyclical bubbling of the central radio source, NGC 1275 (Fabian et al., 2000; 2006).

Brightest Cluster Galaxy

Another crucial aspect of CC clusters is the fact that they typically host a supermassive ($M_{\rm stars} > 10^{11}$ $M_\odot$) and very bright galaxy ($-23 \lesssim M_V \lesssim -21$; e.g. Bernstein & Bhavsar, 2001), sitting at the bottom of their potential well in proximity of the X-ray surface brightness peak. It is the most luminous galaxy in the cluster, that can even exceed by one or two orders of magnitude the luminosity of the second brightest galaxy. For this reason, it is called *brightest cluster galaxy* (BCG). In general, BCGs are old and red early-type galaxies (elliptical or S0), for instance a 'central dominant' or 'cD' galaxy (i.e. supergiant elliptical galaxy with a large and diffuse halo of stars), that is formed and grows by accretion and by mergers with other galaxies during the formation of the cluster (e.g. Collins et al., 2009). In addition, the BCG exhibits signs

[10] sharp surface brightness discontinuities interpreted as contact edges between cold low entropy gas and hot higher entropy gas.

(a) **(b)**

Figure 1.6: *Panel (a):* Perseus cluster with X-ray close-up of the black hole region in the small square (X-ray: NASA/CXC from Reynolds et al., 2020). *Panel (b):* Color composite image of 4 BCGs in the galaxy clusters SPT-CLJ0106-5943, SPT-CLJ0307-6225, SPT-CLJ0310-4647 and SPT-CLJ0615-5746 (X-ray: NASA/CXC/MIT from Calzadilla et al., 2023; Optical: NASA/ESA/STScI).

of ongoing star formation at a level of $10 - 100$ $M_\odot$ yr^{-1} (e.g. Hoffer et al., 2012) and is the main contributor to the Fe abundance excess found in the ICM core (e.g. De Grandi et al., 2014). Its $[\alpha/Fe]$ ratio is usually higher than its satellite galaxies (e.g. Gu et al., 2018), instead the peculiar velocity shows lower values relative to the cluster mean (e.g. Lauer et al., 2014).

As final remark, most of the BCGs are observed to host a radio-loud AGN (e.g. Best et al., 2007), that plays a key role not only in the BCG evolution, but also in the cluster dynamics. As mentioned above, the AGN feedback is able to break the cooling mechanism expected by CF models, and can eventually affect both the gas entropy distribution (e.g. Cavagnolo et al., 2009) and the spread of high-metallicity gas toward the cluster outskirts (e.g. Liu et al., 2019). Moreover, the radio jets are capable of accelerating and injecting cosmic-ray particles in the surrounding environment, fundamental ingredients for the leptonic and the hadronic models behind radio diffuse emission like *mini-halos* (see Sec. 1.2.4).

Fig. 1.6b presents a collection of 4 BCGs found in 4 clusters observed with the *Chandra* X-ray telescope.

1.4.2 Non-cool-core Galaxy Clusters

To the opposite side of the galaxy clusters classification there are the *non-cool-core* (NCC) galaxy clusters, that, based on the definition given above, do not present a cool-core. NCC clusters make up about a half of the local clusters, showing a disturbed ICM morphology and substructures, indicative of a past or an ongoing merger with

other clusters. Shocks and turbulence injected by these energetic events ($E_k \sim 10^{63} - 10^{64}$ erg) are able to disrupt (totally or partially) the cool-core, heat and mix the gas, increase the entropy, spread the metals toward the cluster periphery, (re)-accelerate particles and amplify the cluster magnetic field. As a consequence, NCC clusters show typically a flat and asymmetrical X-ray surface brightness distribution (or more than one peak associated to the merging clusters cores; e.g. Forman et al., 1981), high central temperature and flatter temperature profiles (e.g. Pratt et al., 2007) and lower values of the density in the central regions ($\sim 10^{-3}$ cm^{-3}; Hudson et al., 2010), thus the cooling time exceeds the Hubble time. In some cases, more than one BCG has been found in these environments and their offset with respect to the X-ray peak is used as a simple but robust indicator of unrelaxed systems (e.g. Rossetti et al., 2016). Moreover, synchrotron diffuse emission, such as radio halos[11] and radio relics (Sec. 1.2.4), could be a possible final product of mergers due to CR electrons interactions with the magnetic field.

One problem with this classification consists in defining the best suited parameter to distinguish a CC cluster from a NCC one. Hudson et al., 2010 found that the *central cooling time* (CCT) shows a significant bimodal distribution between the two families and could be a good metric for low-redshift clusters: as mentioned above, CC clusters have very short CCT (< 1 Gyr), instead NCC ones are characterised by longer CCT (> 9 Gyr). Since most of the time there is no sharp separation between opposite objects, they have added also a transition category, the *weak-cool-core* (WCC) clusters, defined as having moderate CCT ($1 - 9$ Gyr).

Entropy is another powerful property that records the thermal history and the dynamics of galaxy clusters. Cavagnolo et al., 2009 have demonstrated that the entropy profiles are well-represented by a power-law model that approaches a constant value, K_0, in the core. The distribution of K_0 for their full archival sample is again bimodal (CC clusters peak at $K_0 \sim 15$ keV cm^2, whereas NCC clusters at $K_0 \sim 150$ keV cm^2), with a poorly populated in-between region of WCC clusters ($K_0 \sim 30 - 50$ keV cm^2).

A textbook example of a merging system is the well known *Bullet cluster*, identified by Tucker et al., 1995 and widely studied by other authors through the years (see e.g. Markevitch et al., 2002; Hayashi & White, 2006; Brownstein & Moffat, 2007).

[11] the reality is a bit more complex, since radio halos have been found even in CC clusters (e.g. Bonafede et al., 2014) or undetected in double-relic clusters (e.g. Bonafede et al., 2017).

Chapter 2

From Synchrotron Emission to Magnetic Field Estimates

In this Chapter, we will describe the *synchrotron* radiative process (Sec. 2.1) responsible for the radio emission in galaxy clusters (see Sec. 1.2.4) and its polarisation (Sec. 2.1.1, 2.1.2 and 2.1.4). The latter one is a key property of this emission mechanism that experiences the so-called *Faraday Rotation*, fully described in Sec. 2.1.3. This effect is at the basis of a sophisticated technique, the *Rotation Measure Synthesis Technique* (Sec. 2.2), that is used to recover information about the magnetic field intensity and profile in galaxy clusters. In the end, an overall view on the methods adopted for the magnetic field estimate is provided in Sec. 2.3.

2.1 Synchrotron Radiation

Synchrotron radiation is produced by the interaction of relativistic electrons ($\gamma = 1000 - 5000$) with a magnetic field, $\vec{\mathbf{B}}$: charged and accelerated particles of energy $E = \gamma m_e c^2$, where $\gamma \gg 1$ is the *Lorentz factor*[1], feel the influence of the $\vec{\mathbf{v}} \times \vec{\mathbf{B}}$ *Lorentz force*, being deflected and describing an helical path around the magnetic field lines; the photons are emitted into beaming cones of semi-aperture angle $\simeq \gamma^{-1}$ about the electrons instantaneous velocity, and the ones directed toward the observer are detected as continuum radiation. The peak of a single electron spectrum is located around the *critical frequency*

$$\nu_c = \frac{3e}{4\pi m_e^3 c^5}(B \sin(\theta))E^2 \text{ Hz} \qquad (2.1)$$

$$\text{in practical units: } \nu_c \simeq 4.2(B_{[\text{G}]}\sin(\theta))\gamma^2 \text{ MHz},$$

which demonstrates the tight correspondence between the electron energy, the magnetic field strength and the frequency it emits (the term θ is the *pitch angle* between the

[1] $\gamma = (1 - v^2/c^2)^{-1/2}$, where v is the velocity of the electrons and c is the speed of light.

electron velocity vector and the magnetic field one). For instance, for $B \simeq 1$ μG, synchrotron radiation at 100 MHz is produced by relativistic particles with $\gamma \simeq 5000$ (Govoni & Ferretti, 2004). The power emitted by a single electron is derived from the *Larmor formula* and expressed as

$$\begin{aligned} -\left(\frac{\mathrm{d}E}{\mathrm{d}t}\right) &= 2\sigma_T c U_{mag} \beta^2 \gamma^2 \sin^2(\theta) \\ \text{in practical units: } -\left(\frac{\mathrm{d}E}{\mathrm{d}t}\right) &\simeq 1.6 \times 10^{-15} B^2 \beta^2 \gamma^2 \sin^2(\theta) \ \frac{\mathrm{erg}}{\mathrm{s}}, \end{aligned} \tag{2.2}$$

where σ_T is the Thomson cross-section, $U_{mag} = B^2/2\mu_0$ is the magnetic field energy density, μ_0 is the vacuum magnetic permeability and $\beta = v^2/c^2$. Since the distribution of the pitch angles is more likely to be randomised by magnetic field irregularities, it can be assumed to be isotropic and the energy loss rate (eq. 2.2) becomes

$$-\left(\frac{\mathrm{d}E}{\mathrm{d}t}\right) = \frac{4}{3}\sigma_T c U_{mag} \beta^2 \gamma^2, \tag{2.3}$$

once averaged over the distribution of pitch angles, $p(\theta)\mathrm{d}\theta = \frac{1}{2}\sin(\theta)\mathrm{d}\theta$.

This mechanism is called *non-thermal* since the electrons energy distribution (between E and $E + \mathrm{d}E$) is described by a power-law

$$N(E)\mathrm{d}E = N_0 E^{-p}\mathrm{d}E, \tag{2.4}$$

where N_0 is the initial number density of the particles and the exponent p is directly linked to the radio spectral index, α, as $p = 2\alpha + 1$. Therefore, the energy radiated in the frequency range, ν to $\nu + \mathrm{d}\nu$, is related to eq. 2.4 through

$$J(\nu)\mathrm{d}\nu = -\left(\frac{\mathrm{d}E}{\mathrm{d}t}\right) N(E)\mathrm{d}E, \tag{2.5}$$

and by substituting eq. 2.3, the total intensity spectrum of an homogeneous and isotropic population of electrons varies as

$$\begin{cases} S(\nu) \propto K B^{1+\alpha} \nu^{-\alpha}, & \tau_\nu \ll 1 \text{ (optically thin)} \\ S(\nu) \propto \nu^{5/2} B^{-1/2}, & \tau_\nu \gg 1 \text{ (optically thick)}, \end{cases} \tag{2.6}$$

where τ_ν is the optical depth of the synchrotron emitting region (Longair, 2011).

In the end, the spectral shape is related to the physics of the acceleration mechanism and to the electron energy losses, that manifest respectively as a flattening or a steepening of the photons distribution beyond a *break frequency*, whose position is related to the time since the acceleration. As a consequence, the characteristic lifetime,

or *cooling time*, takes into account both the synchrotron (eq. 2.3) and the IC energy losses[2] and is computed as

$$t_{cool} \approx 3.2 \times 10^{10} \frac{B^{1/2}}{B^2 + B_{\rm CMB}^2} [(1+z)\nu]^{-1/2} \text{ yr}, \tag{2.7}$$

where B is the magnetic field strength, z is the source redshift, $B_{\rm CMB} \approx 3.25(1+z)^2$ μG is the equivalent magnetic field strength of the CMB and ν is the observing frequency in MHz. Typical values in galaxy clusters are $t_{cool} \lesssim 10^8$ yr (van Weeren et al., 2019).

The total synchrotron emission from a source provides an estimate of the strength of the magnetic field, while the degree of polarisation is an important indicator of the field uniformity, structure and distribution, as it will be discussed in the next Sections.

2.1.1 Synchrotron Polarisation

Another interesting and useful property of the synchrotron radiation is its polarisation. In general, a polarised wave is represented by an electric and a magnetic field vector, $\vec{\mathbf{E}}$ and $\vec{\mathbf{B}}$, lying at a specific angle with respect to each other on a transverse plane, i.e. the one perpendicular to the propagation direction, and the kind of polarisation is then defined in terms of the pattern traced out on it by $\vec{\mathbf{E}}$ over the time.

Considering the case in which the beaming cone lies precisely along the LOS and points toward the observer, the electron acceleration vector, $\vec{\mathbf{a}}$, is in the direction of the Lorentz force, $\vec{\mathbf{v}} \times \vec{\mathbf{B}}$. Given that the electric field vector $\vec{\mathbf{E}}$ is parallel to $\vec{\mathbf{a}}$, it oscillates describing a line on the transverse plane and is perpendicular to the projection of $\vec{\mathbf{B}}$ onto the plane of the sky (Westfold, 1959). In this way, the synchrotron radiation is classified as *linearly polarised*. On the other hand, when the observation is carried at any angle, the radiation polarisation from a single electron appears to be *elliptical*, since there is a component of the electric field vector parallel to the magnetic field lines, that has a different time dependence within each *pulse*, $\Delta t \approx \gamma^{-2}$, compared to that of the perpendicular one. By considering a distribution of pitch angles, the total polarisation is found by integrating over all the electrons which contribute to the intensity and, because the angle $\simeq \gamma^{-1}$ on either side of the LOS is very small in the ultra-relativistic regime, the components parallel to the projection of $\vec{\mathbf{B}}$ cancel out and the resultant polarisation is again *linear* (Longair, 2011).

The degree of polarisation (i.e. the ratio between the linearly polarised radiation and the total emitted one) at a given angular frequency, ω, is computed as

$$\Pi(\omega) = \frac{I_\perp(\omega) - I_\parallel(\omega)}{I_\perp(\omega) + I_\parallel(\omega)}, \tag{2.8}$$

[2] as mentioned in the previous Chapter, galaxy cluster components interact with the surrounding environment, e.g. CMB radiation.

where $I_\perp(\omega)$ and $I_\parallel(\omega)$ are respectively the power per unit angular frequency emitted perpendicular and parallel to the projection of the magnetic field vector onto the plane of the sky (Rybicki & Lightman, 1986); by integrating over the electron energies, assuming a spectrum as eq. 2.4 and by doing some math, eq. 2.8 becomes

$$\Pi = \frac{p+1}{p+7/3}. \tag{2.9}$$

Since $p = 2\alpha + 1$, it is immediately visible how the above parameter can be directly inferred by measuring the total optically thin intensity spectrum from the observations.

In the end, the intrinsic degree of polarisation (eq. 2.9) depends on the particles energy distribution and can reach at maximum percentages around $75-80\%$ for typical values of $p = 2.5$ (Feretti et al., 2012). In practice, the detected synchrotron radiation in radio sources is partially linearly polarised. Effects producing a further reduction, i.e. *depolarisation*, will be discussed in Sec. 2.1.4.

2.1.2 Stokes Parameters

Consider an electromagnetic wave that is propagating in the z direction with speed of light, c, the electric field vector, $\vec{\mathbf{E}}$, can be written in Euclidean coordinates (x, y, z) as

$$\vec{\mathbf{E}}(t, z) = \vec{\mathbf{E}}(0, 0)\cos(\omega t - kz - \delta), \tag{2.10}$$

where t is the time, ω is the angular frequency, $k = \omega/c$ is the absolute value of the wave vector and δ is the phase. As $\vec{\mathbf{E}}$ is perpendicular to z, eq. 2.10 can be decomposed into the x and y orthogonal components, by assuming that $z = 0$

$$\begin{aligned} E_x(t) &= E_x(0)\cos(\omega t - \delta_x) \\ E_y(t) &= E_y(0)\cos(\omega t - \delta_y), \end{aligned} \tag{2.11}$$

where $E_{x,y}(0)$ and $\delta_{x,y}$ are respectively the amplitude and the phase of $E_{x,y}$ (Trippe, 2014 and reference therein). In general, the tip of the electric field vector follows an elliptical trajectory in the xy plane describing the so-called *ellipse of polarisation* (Fig. 2.1a) with equation

$$\frac{E_x(t)^2}{E_x(0)^2} + \frac{E_y(t)^2}{E_y(0)^2} - \frac{2E_x(t)E_y(t)}{E_x(0)E_y(0)}\cos(\delta) = \sin^2(\delta), \tag{2.12}$$

where $\delta = \delta_y - \delta_x$ (Collett, 2005). The *polarisation angle*, ψ, is the angle between the positive x axis and the semi-major axis a of the ellipse, counted in counterclockwise direction and constant in time. It represents one of the most important features of polarised radiation as it traces the orientation of the electric field, thus the direction of the magnetic field projected onto the plane of the sky (see Sec. 2.1.1).

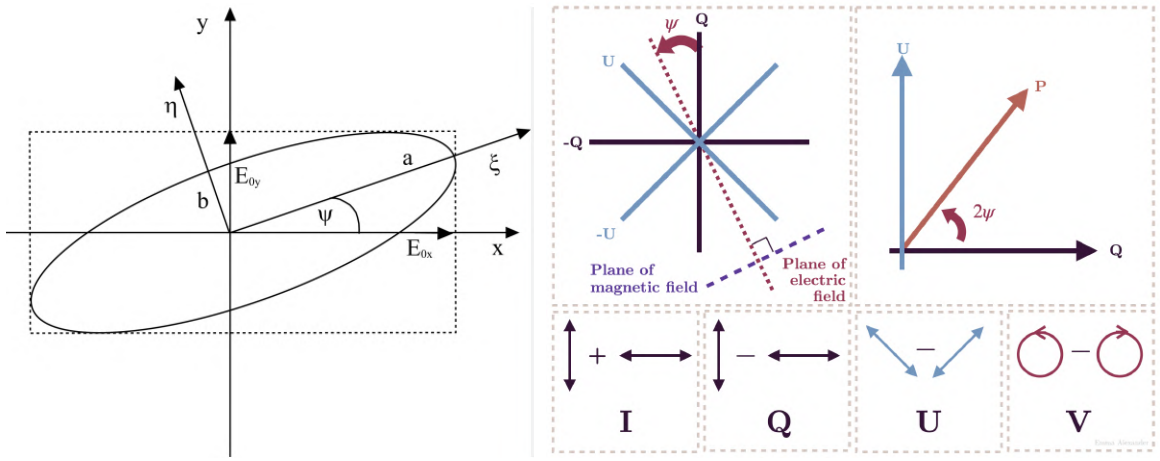

(a) (b)

Figure 2.1: *Panel (a):* The ellipse of polarisation. xy and $\xi\eta$ represent respectively the observer and the ellipse reference frames. The electric field components, $E_{0x,y}$, the semi-major and semi-minor axes, a and b, and the polarisation angle, ψ, are reported (from Perlicki, 2015). *Panel (b):* The Stokes parameters I, Q, U and V. *Left:* Representation of the Stokes Q and U with respect to the polarisation angle ψ, the electric field and magnetic field planes. *Right:* Stokes vector $\vec{\mathbf{P}}$ in the QU plane (by Alexander, 2022 CC-BY 4.0).

To determine the polarisation properties of the wave, time-averaged observable intensities are required, as the polarisation ellipse consists in an instantaneous picture of the polarisation state and the angle ψ is not directly measurable. These quantities can be derived by taking the time average of eq. 2.12, defining that

$$\langle E_i(t), E_j(t)\rangle = \lim_{T\to+\infty} \frac{1}{T}\int_0^T E_i(t)E_j(t)\mathrm{d}t, \ \ (i,j=x,y), \tag{2.13}$$

where T is the total averaging time. This yields the following relations:

$$\begin{aligned} I^2 &= Q^2+U^2+V^2 \ \text{(for totally polarised radiation)} \\ I^2 &> Q^2+U^2+V^2 \ \text{(for partially polarised radiation)}, \end{aligned} \tag{2.14}$$

where I, Q, U and V are the so-called four *Stokes polarisation parameters*, introduced by Stokes in 1852 (Schaefer et al., 2007 and references therein)

$$\begin{aligned} I &= E_x^2(0)+E_y^2(0) \qquad & U &= 2E_x(0)E_y(0)\cos(\delta) \\ Q &= E_x^2(0)-E_y^2(0) \qquad & V &= 2E_x(0)E_y(0)\sin(\delta). \end{aligned} \tag{2.15}$$

By construction, the Stokes parameter I is a measure of the total power of the wave, whereas Q and U represent the linearly polarised component. More precisely, Q describes the preponderance of linearly horizontally polarised light (0°) over the linearly vertically polarised light (90°), and U the one of linear +45° polarised light over linear

$-45°$ (or $135°$) polarised light. Finally, V corresponds to the circularly polarised component (positive counterclockwise and negative clockwise). Notably, the parameters Q, U and V can assume negative values, instead I is always positive. An illustration of the Stokes parameters is shown in Fig. 2.1b.
The linearly polarised intensity can be written therefore as

$$P = \sqrt{Q^2 + U^2}, \tag{2.16}$$

where $V = 0$ given that synchrotron radiation is not intrinsically circularly polarised ($\delta = 0$) and the degree of linear polarisation (eq. 2.9) becomes

$$p = \frac{P}{I} = \frac{\sqrt{Q^2 + U^2}}{I}. \tag{2.17}$$

The latter one can be considered as the amplitude of the complex polarisation, usually known as *Stokes vector*, $\vec{\mathbf{P}}$, defined in the QU plane (Fig. 2.1a) as

$$\vec{\mathbf{P}} = pe^{i2\psi} = Q + iU. \tag{2.18}$$

The phase is represented by the polarisation angle, ψ, in the form

$$\psi = \frac{1}{2}\tan^{-1}\left(\frac{U}{Q}\right) \tag{2.19}$$

and Q and U are respectively the real and imaginary part of the vector (Gardner & Whiteoak, 1966; Saikia & Salter, 1988). In radio observations, the Stokes parameters can be recovered by recording the orthogonal $\vec{\mathbf{E}}$ components ($E_x(0)$ and $E_y(0)$) with the antennas and the receivers.

2.1.3 Faraday Rotation Effect

In astrophysical magnetised plasma, for a given direction of propagation with respect to the magnetic field orientation, two orthogonal modes of an electromagnetic wave can propagate through the medium with different velocities without changing their polarisation state. If the medium contains also free electrons, linearly polarised radiation can be decomposed into two opposite-handed circularly polarised components, *right* (R) and *left* (L), each of them passing through the plasma at their own phase velocity, i.e. the medium has two refractive indices, thus is called *bi-refrangent* (Tinbergen, 1996).

According to the dispersion relation, for a wave of angular frequency, $\omega = 2\pi\nu$, the refractive index of the plasma can assume two possible values, and in the limit $\omega >> \Omega_e$,

$$n_{L,R} \simeq 1 - \frac{1}{2}\frac{\omega_p^2}{(\omega^2 \pm \omega\Omega_e)}, \quad \omega_p = \left(\frac{4\pi n_e^2}{m_e}\right)^{1/2}, \quad \Omega_e = \frac{eB}{m_e c}, \tag{2.20}$$

where ω_p is the plasma frequency and Ω_e is the cyclotron frequency. The difference in time of the two opposite handed waves after travelling a length $\mathrm{d}l$ is

$$\Delta t \sim \frac{\omega_p \Omega_e \mathrm{d}l}{c\omega^3} = \frac{4\pi e^3}{\omega^3 m_e^2 c^2} n_e B \mathrm{d}l \tag{2.21}$$

and the phase difference between the two signals is $\Delta\phi = \omega\Delta t$. Once emerging from a screen with extension L along the LOS, the two modes recombine to give linear polarisation again, but the plane of polarisation is rotated by $\Delta\psi = \frac{1}{2}\Delta\phi$. In an ionised plasma with a magnetic field component along the LOS, i.e. a *magneto-ionic medium*, such rotation of the linearly polarised radiation is called *Faraday rotation* (see Fig 2.2a). In details, the intrinsic polarisation angle, ψ_{int}, results in

$$\psi_{obs}(\lambda^2) = \psi_{int} + \Delta\psi(\lambda^2) = \psi_{int} + \mathrm{RM}\lambda^2, \tag{2.22}$$

where ψ_{obs} is the observed polarisation angle (after the Faraday rotation), λ is the observed wavelength and RM is the *Rotation Measure*. The latter quantity is directly linked to the properties of the rotating region and is defined as

$$\begin{aligned} \mathrm{RM} &= \frac{e^3}{2\pi m_e^2 c^4} \int_0^L n_e(l) B_{\parallel} \mathrm{d}l \\ \text{in practical units: } \mathrm{RM} &= 812 \int_0^L n_e(l)_{[\mathrm{cm}^{-3}]} B_{\parallel[\mu\mathrm{G}]} \mathrm{d}l_{[\mathrm{kpc}]} \ \frac{\mathrm{rad}}{\mathrm{m}^2}, \end{aligned} \tag{2.23}$$

where n_e is the number density of free electrons in cm^{-3}, $B_{\parallel}$ is the component of the magnetic field along the LOS in μG and $\mathrm{d}l$ is the infinitesimal path crossed along the LOS in kpc (Govoni & Ferretti, 2004). It is important to notice that this effect is produced by the projected component of the magnetic field, $B_{\parallel}$, therefore only partial information about the magnetic field 3D geometry will be derived if it is not isotropic. Moreover, once knowing the RM, eq. 2.22 can be inverted to get the intrinsic polarisation angle, ψ_{int}, thus the orientation of the magnetic field projected onto the plane of the sky at the source position.

In principle, to derive the RM from radio observations, a linear fit of eq. 2.22 is performed by plotting ψ_{obs} as a function of λ^2 (see Fig. 2.2b): the RM represents the slope of the best-fit straight line and, by convention, is assumed positive when the magnetic field components are directed towards the observer, whereas negative when they point away (as reported in Fig. 2.2a). Moreover, since angles are handled, ψ_{obs} must be measured at least at three or more wavelengths in order to remove the $n\pi$ *ambiguity*[3], which is responsible for the incorrect determination of the RM. More

[3]the measurements are uncertain by $\pm n\pi$ due to the unknown number of half rotations of the polarisation angle between the source and the observer (Clarke, 2004).

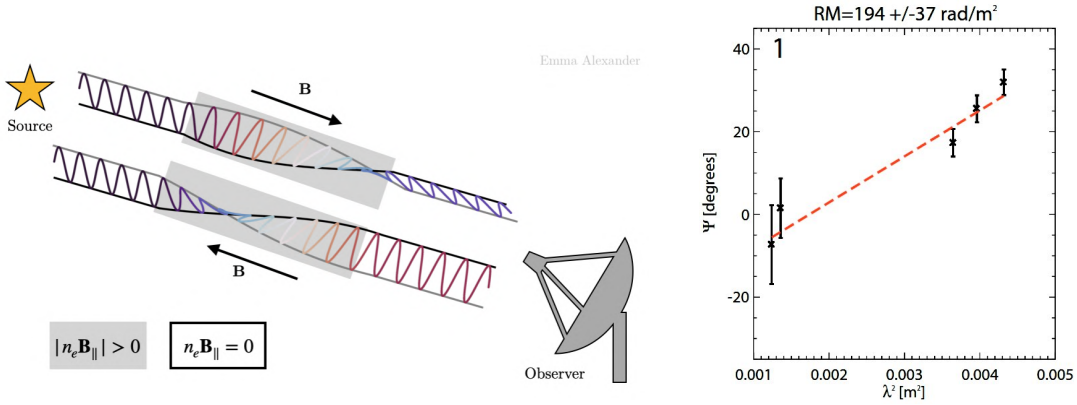

(a) **(b)**

Figure 2.2: *Panel (a):* Simple sketch of the Faraday rotation effect. Two electromagnetic waves are shown propagating from an astrophysical source (*yellow* star) to the observer (antenna). The magneto-ionic medium is traced by the *grey* regions (with same electron number density, n_e, and magnetic field strength, $B_\parallel$): the region with $B_\parallel$ pointing towards the observer rotates the plane of polarisation clockwise, whereas the region with $B_\parallel$ pointing away rotates the polarisation angle by the same amount, but this time counterclockwise (by Alexander, 2022 CC-BY 4.0). *Panel (b):* Example of a linear fit of the polarisation angle in degrees versus λ^2 in m^2. In this case the RM is positive and is reported with the associated error (from Bonafede et al., 2010).

complex scenarios, like sources presenting both synchrotron-emitting and Faraday-rotating regions, need a more sophisticated approach and advanced techniques, as the RM synthesis technique (see Sec. 2.2).

Performing RM analysis on polarised synchrotron sources, e.g. radio galaxies, found in the background or belonging to galaxy clusters, is one of the best tools to get important information about the intracluster magnetic field strength and structure (see Sec. 2.3). In this particular case, the observed RM is a linear sum of all contributions along the LOS between the radio source and the observer, which mainly come from the region local to the object, the ICM and the Milky Way (MW) galaxy:[4]

$$\mathrm{RM}_{obs} = \mathrm{RM}_{source} + \mathrm{RM}_{\mathrm{ICM}} + \mathrm{RM}_{\mathrm{MW}}. \tag{2.24}$$

Several authors have investigated and mapped the RM of the MW using extragalactic radio sources (for a recent work, see Hutschenreuter et al., 2022) and, in general, these studies found that the Galactic foreground rotation can reach values of few $100s$ rad m^{-2} at low galactic latitudes, that quickly drop to few $10s$ rad m^{-2} at higher latitudes (e.g. Clarke, 2004; Taylor et al., 2009). On the other hand, RM arising locally to the radio source is negligible as pointed out in Osinga et al., 2022 (and references therein). Since the focus is on the cluster RM, it is essential to discriminate and remove the contributions from the other sources of Faraday rotation.

[4] all considered as *magneto-ionic* media.

2.1.4 Synchrotron Depolarisation

As anticipated in Sec. 2.1.1, synchrotron radiation is intrinsically partially polarised. Further reduction in the observed degree of linear polarisation can be a consequence of the Faraday rotation, combined both with the instrumental capabilities and the complex configuration of the magnetic field, e.g. *bandwidth* and *beam depolarisation*, as well as the presence of a Faraday-rotating medium emitting itself synchrotron radiation, that is responsible for the so-called *differential Faraday rotation depolarisation* and the *internal Faraday depolarisation*.

To represent the polarisation of synchrotron radiation, the complex polarisation vector (eq. 2.18) has been introduced in Sec. 2.1.2 and, subjected to the Faraday effect, its phase varies according to

$$\vec{\mathbf{P}} = pe^{2i\psi_{obs}(\lambda^2)} = pe^{2i[\psi_{int}+\phi\lambda^2]}, \tag{2.25}$$

where ϕ is the *Faraday depth*. In general, it is defined as the rotation of the polarisation angle originating from an infinitesimal volume, with LOS length $\mathrm{d}\vec{\mathbf{r}}$, in which the medium can be decomposed

$$\phi(\vec{\mathbf{r}}) = \mathrm{K}\int_0^{\vec{\mathbf{r}}} n_e\vec{\mathbf{B}}\cdot\mathrm{d}\vec{\mathbf{r}}, \quad \mathrm{K} = 0.81\ \frac{\mathrm{rad\ cm^3}}{\mathrm{m^2}\ \mu\mathrm{G\ pc}}. \tag{2.26}$$

The RM and the Faraday depth coincide at all wavelengths only when one or several non-emitting regions lie between the source and the observer and in the absence of depolarisation within the observing beam.

Before presenting each effect separately, some quantities should be introduced for a better comprehension. Considering $\epsilon(\vec{\mathbf{r}},\lambda)$ as the synchrotron emissivity, i.e. the energy emitted at wavelength λ and position $\vec{\mathbf{r}}$ per unit time and volume, the observed polarised intensity integrated over the source is expressed as

$$P(\lambda^2) = \frac{\iint_{source} w(\vec{\mathbf{r}})\epsilon(\vec{\mathbf{r}},\lambda)p(\vec{\mathbf{r}})e^{2i\psi(\vec{\mathbf{r}})}\mathrm{d}s\mathrm{d}\Omega}{\iint_{source} w(\vec{\mathbf{r}})\epsilon(\vec{\mathbf{r}},\lambda)\mathrm{d}s\mathrm{d}\Omega}, \tag{2.27}$$

where $p(\vec{\mathbf{r}})$ and $\psi(\vec{\mathbf{r}})$ are respectively the degree of polarisation and the polarisation angle at position $\vec{\mathbf{r}}$, $\mathrm{d}s$ is the infinitesimal path along the LOS and $\mathrm{d}\Omega$ is an element of solid angle. In the following treatment the beam profile, $w(\vec{\mathbf{r}})$, is assumed equal to 1, i.e. flat beam profile. The observed polarised signal is the sum of the emitted polarised radiation produced at all distances, i.e. with all possible Faraday depths. Defining $E(\phi)$ as the fraction of radiation with Faraday depth, ϕ, and $P(\phi)$ as its intrinsic polarisation, eq. 2.27 becomes

$$P(\lambda^2) = \int_{-\infty}^{+\infty} E(\phi)P(\phi)e^{2i\phi\lambda^2}\mathrm{d}\phi, \tag{2.28}$$

where $F(\phi) = E(\phi)P(\phi)$ is the *Faraday dispersion function* (FDF): it is the Fourier transform of the observed polarised intensity and expresses how the intrinsic polarised flux is dispersed at different ϕ (Burn, 1966; Sokoloff et al., 1998). To derive the latter quantity is not sufficient to invert the integral and the alternative approach will be discussed later in Sec. 2.2.

Bandwidth Depolarisation

Bandwidth depolarisation is caused by the rotation of the plane of polarisation of the electromagnetic wave across a finite bandwidth of observation. Since the observed polarisation angle varies with the square of the wavelength (eq. 2.22), it assumes different values at and between the bandwidth edges, i.e. the polarisation vector (eq. 2.25) rotates with different angles resulting in lower polarised signal after the *vector-averaging*. In case of Faraday rotation, the change in the polarisation angle, $\Delta\psi$, across the receiving bandwidth, $\Delta\nu$, with central frequency, ν_0, is given by

$$\Delta\psi = \frac{\mathrm{d}}{\mathrm{d}\nu}(\mathrm{RM}\lambda^2)\Delta\nu = -\psi_0\frac{2\Delta\nu}{\nu_0}, \tag{2.29}$$

where $\psi_0 = \mathrm{RM}\lambda_0^2$ and λ_0 is the central wavelength. With a rectangular passband, the degree of polarisation is reduced by a factor

$$\frac{p(\lambda^2)}{p_i} = \frac{\sin\Delta\psi}{\Delta\psi}, \tag{2.30}$$

below that for monochromatic radiation (Gardner & Daviest, 1966), where p_i is the intrinsic degree of polarisation. This kind of depolarisation is particularly significant in case of very large bandwidths, thus one of the best way to limit it consists in dividing the bandwidth in several channels.

Recently, Fine et al., 2023 found a simple equation that can be used to work out the range of RM in which the bandwidth depolarisation is below a chosen threshold for a given channel configuration, or that can be reversed to determine the approximate strength of depolarisation at a selected RM. Moreover, they developed an algorithm that works similarly to the conventional RM synthesis technique, but uses a different transform. Both of them are implemented within the Canadian Initiative for Radio Astronomy Data Analysis (CIRADA) RM-Tools package[5] under the names `rmtools_bwpredict` and `rmtools_bwdepol` respectively.

Beam Depolarisation

Beam, or *external*, depolarisation is caused by random magnetic field components in a foreground Faraday screen, i.e. a magneto-ionic region between the source of syn-

[5]available at https://github.com/CIRADA-Tools/RM-Tools.

chrotron emission and the observer, that fluctuate on smaller scales than the restoring beam of the instrument. This means that the unresolved magnetic field inhomogeneities of the medium induce unresolved spatial variation in the RM within the resolution element. In details, the superposition of waves with different orientations of their polarisation plane, caused by different Faraday rotation, averages out the polarisation vectors, reducing the degree of linear polarisation observed (Trippe, 2014).

Burn, 1966 provides a law that describes the variation of the degree of polarisation as a function of λ in case of beam depolarisation: consider a cell with size $d << \alpha R$, where α is the angular dimension of the radio source and R is the extension of the screen along the LOS. The Faraday dispersion function introduced in eq. 2.28 can be modelled by a Gaussian with variance $\sigma_{\rm F} = K^2 \langle B_\parallel n_e \rangle^2_{cell} {\rm d}R$, where $\langle B_\parallel n_e \rangle$ is the variance of the product between the electron number density and the parallel component of the magnetic field in a given cell. The degree of polarisation at wavelength λ is therefore

$$p(\lambda^2) = p_i e^{-2K^2 \langle B_\parallel n_e \rangle^2_{cell} \lambda^4 {\rm d}R}. \tag{2.31}$$

Detecting such exponential decline can potentially allow to infer the scale of the magnetic field fluctuating components. Such effect is especially observed in correspondence of radio galaxies seen in projection near the center of galaxy clusters, where the presence of turbulent magnetic field elements is expected. Unfortunately, the reality is much more complex than that and a more developed treatment on external depolarisation is discussed in Tribble, 1991.

Differential Faraday Rotation Depolarisation

Consider a region containing both relativistic and thermal electrons and regular magnetic fields, the polarisation planes of the waves are rotated by different amounts depending on where the corresponding synchrotron-emitting layers are located with respect to the observer (i.e. at different depths): Faraday rotation angles originating from the nearer side of the medium rotate less than those emitted from the farther regions, as the polarised radiation has to travel larger sections of the medium. This effect is known as *differential Faraday rotation* and results in a reduction of the observed degree of polarisation: in case the source is represented by an homogeneous optically thin slab

$$p(\lambda^2) = p_i \frac{|\sin(2\langle {\rm RM} \rangle \lambda^2)|}{|2\langle {\rm RM} \rangle \lambda^2|}, \tag{2.32}$$

where $\langle {\rm RM} \rangle$ is the average observed RM (Arshakian & Beck, 2011). A generalisation of this effect for different models apart from the uniform slab is presented in Sokoloff et al., 1998.

Internal Faraday Depolarisation

The configuration, under which this kind of depolarisation occurs, follows the one presented for the beam depolarisation, i.e. the presence of turbulent magnetic field components, that leads to different amounts of Faraday rotation along different LOSs within the beam. In case additional relativistic electrons are present internal to the screen and emit synchrotron radiation, the caused effect is called *internal Faraday depolarisation*. Assuming Λ_C (in pc) the scale of the cell in which the magnetic field component is tangled and $f = \langle n_e \rangle / n_e$ the cell filling factor, the dispersion of the RM, $\sigma_{\rm RM}$, is defined as

$$\sigma^2_{\rm RM} = 0.81^2 \langle n_e B_\parallel \rangle^2 \frac{L \Lambda_C}{f}. \tag{2.33}$$

In case of a uniform slab with extent L along the LOS, the degree of polarisation becomes

$$p(\lambda^2) = p_i \frac{1 - e^{-S}}{S}, \tag{2.34}$$

where $S = 2\sigma^2_{\rm RM}\lambda^4 - 2i{\rm RM}\lambda^2$ (Arshakian & Beck, 2011). The last expression is the corrected version of the first one proposed by Burn, 1966 and further details are presented by the work of Sokoloff et al., 1998.

2.2 RM Synthesis Technique

As discussed in Sec. 2.1.3, the determination of the RM from the observations is not always an easy task and the assumption that the sources are *Faraday-simple*, i.e. characterised by a single value of ϕ (eq. 2.26) which coincides with their RM, not always holds. Both complex physical configurations and instrumental limitations may come out, e.g. the $n\pi$-ambiguity, the presence of more than one source along a single LOS, or of a Faraday-rotating and synchrotron-emitting medium (i.e. *Faraday-complex*), or of faint sources undetectable even after integrating all channels due to bandwidth depolarisation. In most of the cases, the RM cannot be recovered with a classic linear fit and Brentjens & de Bruyn, 2005 developed a more advanced method, called 'RM Synthesis Technique', in order to recover emission at multiple Faraday depths along a particular LOS.

Following eq. 2.28, the observed polarised intensity, $P(\lambda^2)$, coming from all possible values of ϕ, is related to the Faraday dispersion function, $F(\phi)$, according to

$$P(\lambda^2) = \int_{-\infty}^{+\infty} F(\phi) e^{i2\phi\lambda^2} {\rm d}\phi. \tag{2.35}$$

Eq. 2.35 is very similar to a Fourier transform, but since $P(\lambda^2)$ cannot assume negative values (i.e. we do not observe at $\lambda^2 < 0$) and is not defined for all $\lambda^2 > 0$, the integral

cannot be directly inverted to get the FDF. The authors generalised the equation by introducing a *weight function*, $W(\lambda^2)$, that represents how the λ^2 space is sampled and assumes non-zero values at all λ^2 points and zero elsewhere (i.e. a top-hat function). Then, the observed polarised intensity is re-written as

$$\tilde{P}(\lambda^2) = W(\lambda^2)P(\lambda^2) = W(\lambda^2)\int_{-\infty}^{+\infty} F(\phi)e^{i2\phi\lambda^2}\mathrm{d}\phi, \tag{2.36}$$

and after some maths, the *reconstructed* FDF, $\tilde{F}(\phi)$, is expressed as the convolution between the intrinsic polarised flux and the RM *transfer function* (RMTF), $R(\phi)$,

$$\begin{aligned} \tilde{F}(\phi) = F(\phi) \circledast R(\phi) = K\int_{-\infty}^{+\infty} \tilde{P}(\lambda^2)e^{-i2\phi\lambda^2}\mathrm{d}\lambda^2, \\ R(\phi) = K\int_{-\infty}^{+\infty} W(\lambda^2)e^{-i2\phi\lambda^2}\mathrm{d}\lambda^2, \end{aligned} \tag{2.37}$$

where K is the inverse of the integral over $W(\lambda^2)$. The RMTF describes the instrumental response in the Faraday space based on the λ^2-coverage and is represented by a complex valued *sinc* function, where the real part corresponds to the response of the transform parallel to the QU vector at $\lambda = \lambda_0$ and the imaginary part to the one orthogonal to it. The quality of the reconstruction depends mainly on the weight function, since a more large and complete coverage of the λ^2 space with few holes improves the Full-Width-Half-Maximum (FWHM; i.e. the resolution in the Faraday space) and reduces the sidelobes of the RMTF, respectively.

Moreover, a shift, λ_0^2, may be added in the exponential term in order to get a better behavior of the RMTF and eq. 2.37 becomes

$$\begin{aligned} \tilde{F}(\phi) = K\int_{-\infty}^{+\infty} \tilde{P}(\lambda^2)e^{-i2\phi(\lambda^2-\lambda_0^2)}\mathrm{d}\lambda^2, \\ \lambda_0^2 = \frac{\int_{-\infty}^{\infty} W(\lambda^2)\lambda^2 d\lambda^2}{\int_{-\infty}^{\infty} W(\lambda^2)\mathrm{d}\lambda^2}, \end{aligned} \tag{2.38}$$

where λ_0^2 is the weighted average of the observed λ^2. It corresponds to de-rotate all polarisation vectors back to their positions at $\lambda = 0$ and affects the argument and not the amplitude of the RMTF. If $\phi\delta\lambda^2 << 1$[6] and since the channels have a finite bandwidth, eq. 2.38 can be approximated as a sum:

$$\tilde{F}(\phi) \approx K\sum_{i=1}^{N} \tilde{P}_i e^{-2i\phi(\lambda_i^2-\lambda_0^2)}, \quad K = \left(\sum_{i=1}^{N} w_i\right)^{-1}, \tag{2.39}$$

where λ_i^2 is λ^2 of the i-th channel, $\tilde{P}_i^2 = \tilde{P}(\lambda_i^2) = w_i P(\lambda_i^2)$ and $w_i = W(\lambda_i^2)$.

[6] for Faraday-simple sources, $\phi\delta\lambda^2 >> 1$ for Faraday-complex ones.

The benefit of this technique resides mainly in two reasons: at first, it minimises the $n\pi$-ambiguity by performing multiple measures in adjacent narrow frequency channels, in which the observation bandwidth is split; second, it resolves the possible instrumental depolarisation by using a series of RM values and finding the one that maximises the signal level resulting from the addition of the polarised flux from all channels. Finally, $\tilde{F}(\phi)$ will peak at the ϕ corresponding to the RM of the source, in case of Faraday-simple objects. At other values of ϕ, the polarisation vector rotates at the wrong rate through the λ^2 space, thus will not constructively interfere throughout the band, and the total flux will be lower. If more than one source is seen through the same LOS, each peak corresponds to a source. On the other hand, for Faraday complex media, the value of $|\tilde{F}(\phi_{peak})|$ and of ϕ_{peak} are not sufficient to describe the polarisation and rotation effect experienced by the radiation since the polarised emission would be spread at different values of ϕ and affected by internal Faraday depolarisation. Thus, ϕ_{peak} represents only the main component of the reconstructed FDF and $|\tilde{F}(\phi_{peak})|$ is then a fraction of the total emission of the source.

In order to apply the RM synthesis technique, three parameters have to be checked in advance: the maximum observable Faraday depth, $|\phi_{max}|$, the resolution in ϕ space, $\delta\phi$, and the largest scale in ϕ space to which we are sensitive, $\Delta\phi_{max}$. Estimates for the FWHM of the main peak of the RMTF, the maximum Faraday depth to which one has more than 50% sensitivity and the scale in ϕ space to which the sensitivity drops to 50% are approximately

$$\begin{aligned} \delta\phi &\approx \frac{2\sqrt{3}}{\Delta\lambda^2}, \\ |\phi_{max}| &\approx \frac{\sqrt{3}}{\delta\lambda^2}, \\ \Delta\phi_{max} &\approx \frac{\pi}{\lambda^2_{min}}, \end{aligned} \tag{2.40}$$

where $\Delta\lambda$ is the width of the λ distribution, $\delta\lambda$ is the channel width and λ_{min} is the shortest wavelength. If the extent of a source in ϕ is less than the FWHM of the RMTF, it is unresolved, whereas in order to resolve Faraday complex structures, the main peak of the RMTF should be narrower than the maximum scale to which one is sensitive, i.e. $\lambda_{min} < \Delta\lambda$.

The RM synthesis technique can be applied with the `rmsynth3d` task implemented in CIRADA RM-Tools, which takes as input Stokes Q and U cubes with the associated frequency list.

2.2.1 RM Deconvolution

Since the resulting reconstructed FDF, $\tilde{F}(\phi)$, is the convolution of the intrinsic FDF, $F(\phi)$, with the RMTF, multiple features may appear in the FDF spectrum caused by the RMTF sidelobes and can make their interpretation tricky. The situation can be improved by performing a deconvolution operation, similar to the aperture synthesis imaging developed by Högbom, 1974. The main two differences consist in the adopted dimension, one (ϕ) rather than two (spatial), and the fact that the functions involved are complex quantities. This algorithm has been implemented within the CIRADA RM-Tools software package as a task called `rmclean3d`, and follows this procedure (Heald, 2009): it starts with finding the location of ϕ_{peak} and then scales the values of the real and imaginary parts of $|\tilde{F}(\phi_{peak})|$ by a loop gain parameter, g, typically 0.1. This is stored as a 'clean component'. Next, a version of the RMTF, shifted and scaled to be equal to $g|\tilde{F}(\phi_{peak})|$ at $\phi = \phi_{peak}$, is subtracted from the FDF. At this point, the residuals are searched for a new peak and the loop is repeated until the residuals are all below a specified threshold, or a maximum number of iterations is reached. Finally, the clean components are convolved with a restoring function and added to the residuals. The result is the *deconvolved Faraday dispersion function*.

Although this procedure helps in reducing secondary lobes, it is not well suited to detect Faraday-complex sources since it assumes a Dirac δ-function model for every detected component. Some techniques have been proposed to optimise the reconstruction of Faraday-complex spectra (e.g. Bell et al., 2013). All of them assume a model for the synchrotron-emitting and Faraday-rotating medium and nowadays their performances are still tested and debated.

2.3 Magnetic Field Estimate

2.3.1 Equipartition

The first method used to estimate the magnetic field intensity is the *equiparititon*. The total energy of a synchrotron source can be assumed to be stored in the particles, such as protons (U_{pr}) and electrons (U_{el}), and in the magnetic field (U_B):

$$U_{tot} = U_{el} + U_{pr} + U_B = (1 + k)U_{el} + U_B, \tag{2.41}$$

where k represents the assumption about the protons energy contribution with respect to the electrons one (usually, $k = 0$ or 1); U_{el} is the total electron energy (obtained by integrating eq. 2.4 in a given energy range) and can be written as a function of the total synchrotron luminosity, L_{syn}, whereas U_B is the magnetic field energy density integrated over the source volume, V. The name of this method arises from the concept

that the energy stored in the particles and in the magnetic field is assumed nearly the same

$$U_B = \frac{3}{4}(1+k)U_{el}, \tag{2.42}$$

and by considering the source at the minimum energy state. Following this approach, the *equipartition magnetic field* is derived as

$$B_{eq} = \left[\frac{24\pi}{7}\xi(\alpha,\nu_1,\nu_2)\right]^{1/2}(1+k)^{2/7}\nu_0^{2\alpha/7}(1+z)^{(6+2\alpha)/7}I_0^{2/7}d^{-2/7}, \tag{2.43}$$

where $\xi(\alpha,\nu_1,\nu_2)$ is a constant tabulated in Govoni & Ferretti, 2004, z is the redshift, α is the spectral index, d is the source depth in kpc and I_0 is the source brightness in mJy arcsec^{-2}, computed as the the ratio between the flux density and the source area at the frequency ν_0 in MHz.

This approach provides a very first estimate of the strength of the magnetic field, ranging in general between $0.1-10$ μG, and can be applied to the clusters synchrotron diffuse emission, such as radio halos and radio relics (e.g. van Weeren et al., 2009, 2011b). Notably, the equipartition method should be used with care since it is based on several assumptions. For instance, Beck & Krause, 2005 proposed a revised formula using the number density ratio in a given energy interval and pointed out that protons are dominant with respect to the electrons as predicted by CR origin models, i.e. $k >> 1$. In this way, the 'classical' practice underestimates the magnetic field intensity, instead the new one leads to higher values consistent with Faraday rotation observations.

2.3.2 X-ray IC Emission

In general, relativistic electrons can scatter and transfer energy to photons coming from a radiation field through the IC scattering. In the case in which the relativistic electrons population produces both the radio synchrotron and the X-ray IC photons, the respective total powers are related:

$$\frac{L_{syn}}{L_{IC}} \propto \frac{u_B}{u_{ph}}, \tag{2.44}$$

where $u_B = B^2/8\pi$ is the magnetic field energy density and u_{ph} is the photon field energy density (for the CMB, $\sim 5\times10^{-13}(1+z)^4$ erg cm^{-3}). Extending this to a power-law energy distribution of electrons (eq. 2.4), the expression for the magnetic field strength, required to account for both, is

$$B = C(p)(1+z)^{(p+5)/(p+1)}\left(\frac{F_{syn}}{F_X}\right)^{2/p+1}\left(\frac{\nu_{syn}}{\nu_X}\right)^{(p-1)/(p+1)}, \tag{2.45}$$

where $C(p)$ is a proportionality constant, p is the index of the electrons distribution and F_{syn} and F_X are respectively the fluxes at the frequencies ν_{syn} and ν_X (Rybicki & Lightman, 1986). In this way, it is possible to give a first estimate to the magnetic field intensity, averaged over the emitting volume, once knowing the total luminosities.

The major difficulty in this method lies in discriminating between the dominant thermal X-ray component of the ICM and the non-thermal one, and bright cluster radio galaxies can contaminate the X-ray emission too. To date, there is not yet a statistical evidence for IC radiation and its non-detection allows to derive upper limits on it. Combining that with radio flux density measurements of radio halos, lower limits on the ICM magnetic field strength can be computed. The range obtained is around $0.1 - 0.5$ μG (e.g. Rossetti & Molendi, 2004; Wik et al., 2014; Bolivar et al., 2023).

2.3.3 Faraday Rotation Measure

The most promising technique to derive information about the ICM magnetic field strength and geometry is the analysis of the Faraday rotation on radio galaxies located both inside and in the background of galaxy clusters. This kind of sources produces linearly polarised synchrotron radiation from the jets and the lobes and, as explained in Sec. 2.1.3, the polarisation angle of these waves is rotated by a quantity proportional to the RM once passing through the ICM (i.e. an ionised and magnetised plasma). By taking the RM from the radio observations and given a model for the electron number density distribution (e.g. the β-model from X-ray observations; eq. 1.7), it is possible to extrapolate the parallel component of the cluster MF along the LOS according to eq. 2.23.

The best way to study how and on which scales the magnetic field changes across the ICM is to obtain high resolution RM maps of radio sources located at different projected distances from the cluster center, derive the average value of the RM, $\langle \mathrm{RM} \rangle$, and its dispersion, σ_{RM}, and then compare the radial profiles with the ones obtained from simulations. In general, the distribution of the RM detected across the radio galaxies shows a patchy structure, indicating that the MF is not regularly ordered on the cluster dimensions, but have components tangled on scales as low as 10 kpc or less, and is nearly a Gaussian. However, many RM distributions present clear evidence for a non-zero mean, if averaged over areas comparable to the radio source size, that are likely due to fluctuations of the cluster magnetic fields on scales greater than the typical source size. For this reason, it is necessary to consider MF models where both small and large scale structures are taken into account (see Sec. 5.1). In addition, some radio galaxies are subjected to the so-called *Laing-Garrington effect*, where the farthest lobe suffers a higher Faraday rotation due to the LOS passing through a larger amount of intervening material (Laing, 1988; Garrington et al., 1988).

Such studies have been carried out both statistically and on individual objects. Samples of RM measurements associated to polarised radio galaxies embedded in galaxy clusters and outside the clusters regions display an excess of $\langle \mathrm{RM} \rangle$ and σ_{RM} in the projected cluster areas (e.g. Clarke et al., 2001; Böhringer et al., 2016), as shown in Fig. 2.3a. In general, $\langle \mathrm{RM} \rangle$ and σ_{RM} radial profiles decrease with increasing projected distance from the cluster center, with values going from $100s$ in the core to $10s$ of rad m^{-2} in the peripheral regions (see Fig. 2.3b), suggesting that the MF becomes less intense towards larger distances (e.g. Eilek & Owen, 2002; Govoni et al., 2010). Information about the magnetic field in individual clusters through RM studies has been obtained so far in few objects, including both relaxed and merging clusters (e.g. Guidetti et al., 2008; Bonafede et al., 2010, 2013; Vacca et al., 2012; Govoni et al., 2017): CC clusters can even exceed MF intensities of 10 μG, while NCC clusters are characterised by a few μG strenghts. The values obtained by RM studies are systematically higher than the ones derived from radio halo data and from IC X-ray emission, but, as mentioned before, the last ones rely on several assumptions and the estimates are volume-averaged.

Future high resolution Faraday rotation analysis with the next generation radio telescopes (e.g. SKA) should help in detecting a larger number of polarised synchrotron sources, in minimising the depolarisation effects and in distinguishing the possible local effects to the radio sources (e.g. Rudnick & Owen, 2014; Bonafede et al., 2015).

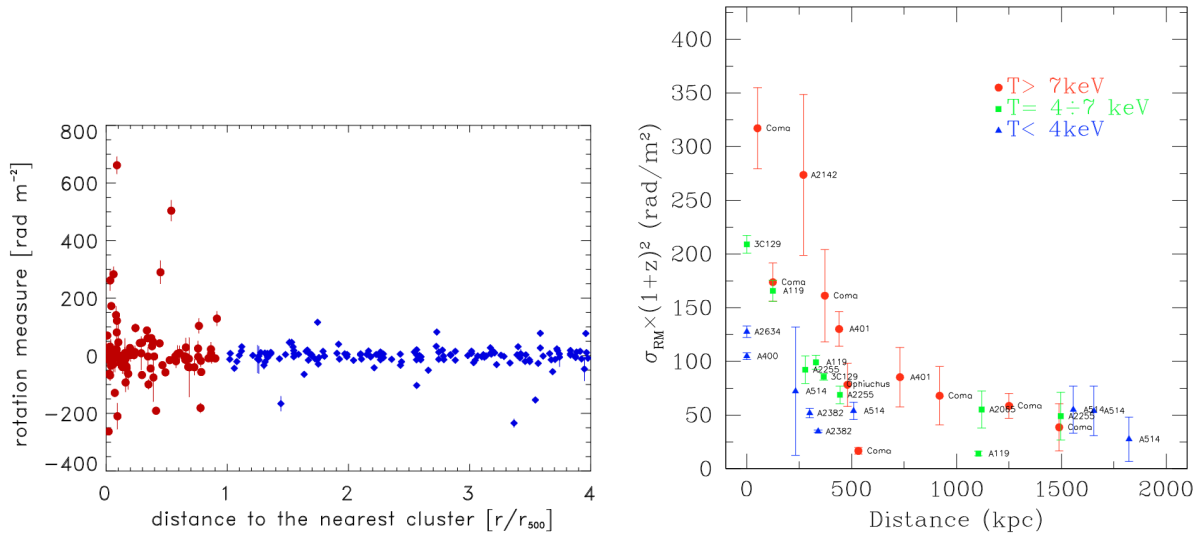

(a) **(b)**

Figure 2.3: RM and σ_{RM} radial profiles. *Panel (a):* Statistical sample of RM of polarised synchrotron extragalactic sources as a function of the distance from the nearest cluster (in Mpc and normalised for r_{500}). The RM inside r_{500} are marked with the *red* circles and those outside with the *blue* diamonds (from Böhringer et al., 2016). *Panel (b):* σ_{RM} distribution as a function of the projected distance in kpc from the cluster X-ray center for several labelled objects. The different symbols represent the cluster temperature (from Govoni et al., 2010).

2.3.4 Felten Formula

In the simplest approximation, the magnetic field components are assumed to be randomly distributed and tangled on a single cell with uniform size, Λ_c, electron number density, n_e, and parallel magnetic field strength to the LOS, $B_\parallel$. By integrating over larger scales and including a larger number of cells, the linearly polarised radiation experiences a random walk process. Therefore, the observed RM along any given LOS is a Gaussian distributed with mean, $\langle \mathrm{RM} \rangle$, and variance, σ^2_{RM}, given by

$$\langle \mathrm{RM} \rangle = 812 n_e B_\parallel L \ \frac{\mathrm{rad}}{\mathrm{m}^2} \tag{2.46}$$

$$\sigma^2_{\mathrm{RM}} = \langle \mathrm{RM}^2 \rangle = 812^2 \Lambda_c \int_0^L (n_e B_\parallel)^2 \mathrm{d}l \ \frac{\mathrm{rad}^2}{\mathrm{m}^4}. \tag{2.47}$$

By considering a gas density profile for the ICM which follows the β-model (eq. 1.7) and by integrating eq. 2.47, the relation between the RM dispersion, σ_{RM}, as a function of the projected distance from the cluster center, $r_\perp$, and the magnetic field intensity, $B = \sqrt{3} B_\parallel$, is known as *Felten formula*, firstly introduced by Felten, 1996, and writes

$$\sigma_{\mathrm{RM}} = \frac{K B n_0 r_c^{1/2} \Lambda_c^{1/2}}{(1 + r_\perp^2 / r_c^2)^{(6\beta - 1)/4}} \sqrt{\frac{\Gamma(3\beta - 0.5)}{\Gamma(3\beta)}}, \tag{2.48}$$

where Γ is the *Gamma function* and the constant K depends on the integration path over the gas density distribution (624, if the source lies completely beyond the cluster and 441 if the source is halfway through the cluster; see Govoni & Ferretti, 2004); n_0, r_c and β are respectively the central gas number density, the core radius and the parameter 1.6, derived from X-ray observations. In general, Λ_c corresponds to the magnetic field *auto-correlation length*, Λ_B, (Murgia et al., 2004), but for a preliminary estimate of the magnetic field strength is assumed to range between $10 - 100$ kpc, as the observed RM fluctuations indicate that the ICM magnetic field is not regularly ordered, but turbulent on such scales (Feretti et al., 2012).

Chapter 3

Abell 2142 Galaxy Cluster

The target of this thesis is Abell 2142 (A2142; Right Ascension (RA_{J2000}) = 15h 58m 21s; Declination (DEC_{J2000}) = 27° 13′ 37″, in the Corona Borealis constellation), a massive cluster with $M_{500} = (8.8 \pm 0.2) \times 10^{14}$ $M_\odot$ (Ettori et al., 2017) and $R_{500} = 1408.5 \pm 70.4$ kpc[1] (Planck Collaboration et al., 2016), located in the Local Universe at redshift $z = 0.0894$ (Böhringer et al., 2000). It is the dominant central member of the Abell 2142 galaxy supercluster, which extends up to 50 h^{-1} Mpc[2] and comprises 950 galaxies within $\sim$ 3 Mpc, that are hierarchically organised in many structures and substructures. Owers et al., 2011 found that most of them comprise $\sim$ 10 members, indicating that there is no sign of recent or ongoing major mergers. The galaxy population has been studied statistically by Poopakun & Kriwattanawong, 2019 in a redshift range between 0.07 and 0.12, including both blue sequence, $(u - z) < 3.2$, and red sequence sources, $(u - z) > 3.2$, where u (ultraviolet) and z (infrared) are SDSS photometric filters.

Studies carried out in the **X-ray band** using *Chandra* and *XMM-Newton* have demonstrated the non-relaxed nature of this object, that presents an asymmetrically distributed ICM, extending along the north-west/south-east axis, aligned with the filamentary structure of the supercluster (Einasto et al., 2015). The gas is cooler ($\lesssim 7$ keV) at the center with respect to the global temperature, $\sim 8-9$ keV, and the average X-ray luminosity is $L_X = 7.20 \times 10^{44}$ erg s^{-1} (Henry & Briel, 1996; Santos et al., 2010). The metallicity is $Z = 0.35$ $Z_\odot$ in the core, declining down to ~ 0.15 $Z_\odot$ at R_{500} (Tchernin et al., 2016), where $Z_\odot = 0.013$. Four spiral-like cold fronts have been observed as a direct consequence of a core sloshing episode, three of them of small-scale and the fourth one of large scale, $\sim$ 1 Mpc, to the south-east side, for which the origin is still unclear (Fig. 3.1; Markevitch et al., 2000; Rossetti et al., 2013). In this case, the sloshing does not involve only the densest and coolest gas at the center, but it is spread out to R_{500}

[1] where M_{500} is the mass contained within R_{500} and R_{500} is the radius at which the density is 500 times the critical density of matter in the Universe at the cluster redshift.

[2] h = H/100 Mpc s km^{-1}, where H is the *Hubble parameter* in km s^{-1} Mpc^{-1}.

and may have strong effects on the global properties of the cluster and induce cluster-scale radio emission. A suggested past *intermediate-mass-ratio merger*[3], viewed at a time at least $1-2$ Gyr after the initial core crossing, was not able to disrupt entirely the cool-core, and subsequent minor mergers bring A2142 to share properties from both the canonical classified kind of clusters and to be catalogued as a *warm-cool-core* (Markevitch et al., 2000; Wang & Markevitch, 2018). In this case, a well-defined X-ray peak is present as in relaxed structures, but the density ($n_0 = 3.5\times10^{-3}$ cm^{-3}; Henry & Briel, 1996), temperature and entropy ($K_0 = 49$ keV cm^2; Wang & Markevitch, 2018) are not consistent with typical values found for CC clusters (see Sec. 1.4.1). Eckert et al., 2014 report the discovery of an irregular X-ray substructure with gas temperature of 1.4 keV in the outskirts of A2142, where the tip of the X-ray emission coincides with a concentration of galaxies. This structure is interpreted as a galaxy group in the process of being accreted onto the main DM halo and supports the scenario where the cold fronts originate from core sloshing induced by minor mergers (Owers et al., 2011; Liu et al., 2018).

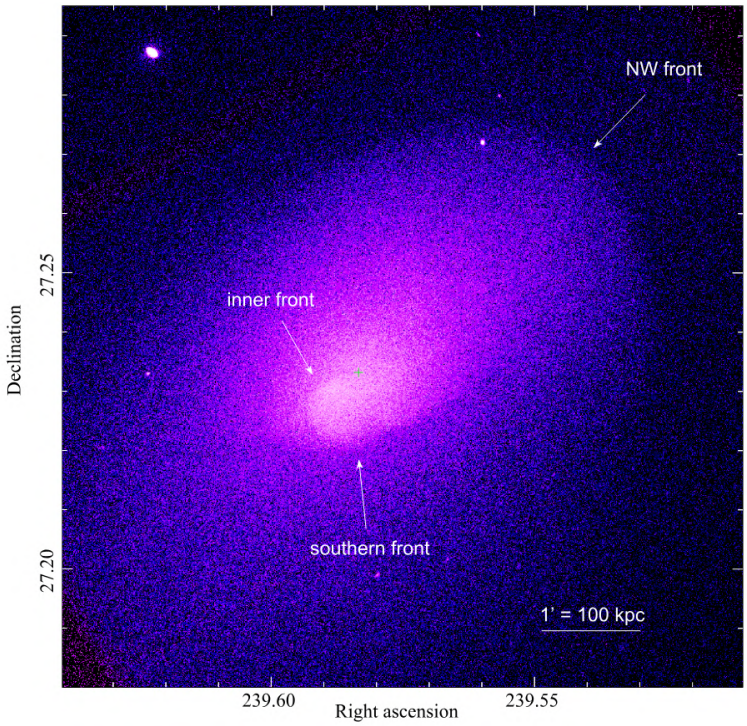

Figure 3.1: *Chandra* X-ray image of A2142 in the $[0.8-4]$ keV range. Three cold fronts (inner, southern and north-east) are labelled in *white* (from Wang & Markevitch, 2018).

Another evidence comes from the **optical** side of the electromagnetic spectrum revealing the presence of two faint r-band BCGs (BCG1 and BCG2): BCG1 (r-band magnitude = 14.52) has spectroscopic redshift $z_{\rm spec} = 0.0908$ and lies at the center of

[3]in general, it is considered as a *major merger* if the two objects are comparable in size and mass and as a *minor merger* if the two objects have a large discrepancy in size and mass, e.g. satellite galaxies and groups.

the gravitational potential (with an offset of ≈ 30 kpc from the gas density peak; Wang & Markevitch, 2018), close to the innermost cold front; BCG2 (r-band magnitude = 14.93), instead, is located to the north-west of the cluster center with spectroscopic redshift $z_{\rm spec} = 0.0965$. It possibly belongs to another merging group and the measured relative velocity is of ~ 1800 km s^{-1} (Oegerle et al., 1995). No significant radio emission is associated to BCG2, whereas BCG1 shows a weak radio AGN without X-ray cavities, suggesting that the displaced peak has starved its nucleus of accreting gas for a significant period of time and that may contribute in releasing seed electrons for subsequent re-acceleration and formation of the radio diffuse emission (Wang & Markevitch, 2018). Okabe & Umetsu, 2008 performed **weak-lensing** studies and found clumps and substructures associated to infalling small galaxies and groups: a north-west mass substructure located ahead of the north-west cold front, a mass concentration associated with a luminous galaxy in front of the south cold front and the main mass peak around BCG1. No significant clumpy mass structure has been observed around BCG2, possibly because of the induced displacement between the latter one and the DM halo after the merger.

Moving to the **radio band**, both radio dishes and *VLA*, *LOFAR* and *MeerKAT* high resolution data have helped over the years in confirming the complexity of this environment (e.g. Giovannini et al., 1999; Farnsworth et al., 2013), that shows an interesting multi-component radio halo (Venturi et al., 2017; Bruno et al., 2023; Riseley et al., 2024): the central component ('Halo 1', H1, or 'core') is more roundish, is co-located with the brightest part of the ICM and is confined within the inner cold front, possibly formed by core sloshing or hadronic collisions between protons (like mini-halos); the second component ('Halo 2', H2, or 'ridge') is more ridge-like and uniform in surface brightness, and extends to the south-east following the direction of the large scale cold fronts, possibly formed by turbulence due to large scale sloshing or by off-axis minor mergers (both of them are show in Fig. 3.2). The region in between the 'core' and the 'ridge', shows a depletion of radio emission, which forms a 'bay'-like structure with a significant flattening in the spectral index ($\alpha = 0.9$). H1 and H2 may probe the evolution of the core sloshing on different scales and/or times and may trace different levels of perturbation and magnetic field strength that are present in the ICM. Riseley et al., 2024 confirmed the presence of a third halo component ('Halo 3', H3), with elliptical morphology elongated in the north-west/south-east direction, encompassing the other structures and filling a volume out to ~ 1.2 Mpc from the cluster center. Bruno et al., 2023 proposed two potential scenarios for its generation: either the natural evolution of the original merger $\sim$ 4 Gyr ago, or the continuous accretion of small galaxy groups onto the main structure, that provides sufficient turbulence injected over the cluster volume. In addition, H2 might have been the inner part of H3 in the past,

hence implying the same origin of the two components. All the components of the halo have steep radio spectra, $\alpha_{\rm H1} = 1.09 \pm 0.03$, $\alpha_{\rm H2} = 1.15 \pm 0.04$ and H3 showing an ultra-steep radio spectrum with $\alpha_{\rm H3} = 1.68 \pm 0.10$. Riseley et al., 2024 performed a point-to-point correlation investigation for the thermal/non-thermal connection between the radio surface brightness and the X-ray surface brightness, $I_R \propto I_X^k$[4], and between the radio spectral index and the X-ray surface brightness, α/I_X. They found a sub-linear correlation for I_R/I_X, where H1 and H3 present very similar slopes, while H2 shows a flatter relation; for α/I_X they obtained an unexplained anti-correlation for H1 and a positive correlation for H2.

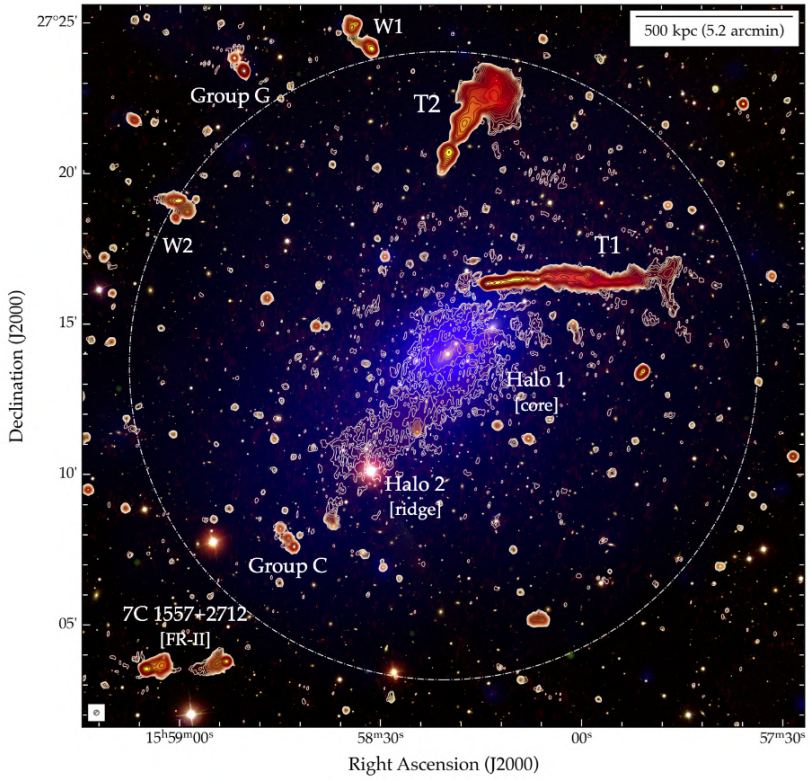

Figure 3.2: Color-composite image of A2142, with optical RGB (SDSS) overlaid radio contours at 143 MHz. Yellow-through-red colors trace the radio surface brightness at 143 MHz (LOFAR) and at 1283 MHz (MeerKAT), both shown at 10″ resolution. Blue colors trace the ICM emission measured by *XMM-Newton*. Known sources, like the two radio halo components and the radio galaxies, are labelled in *white* (from Riseley et al., 2024).

Finally, Bruno et al., 2023 discussed the scenario in which secondary CRe contribute to the emission of H1: in this case, the sub-linear value of k on scales of $\sim 100 - 200$ kpc would indicate a flat CR proton distribution in the core and a strong magnetic field ($B > B_{\rm CMB}$, where $B_{\rm CMB} \sim 4$ μG is the equivalent magnetic field of the CMB at the cluster redshift). Analysis and results on the magnetic field intensity and profile performed later in this work would allow us to support or not this hypothesis.

[4] $k < 1$ refers to a sub-linear correlation, i.e. the distribution of the non-thermal components is broader than that of the thermal components, and vice versa for a super-linear slope ($k > 1$).

Finally, the galaxy population of A2142 includes two head-tail **radio galaxies**: T1 ($z_{\rm spec} = 0.09540$) and T2 ($z_{\rm spec} = 0.08953$), that present interaction with the ICM due to their distorted morphology (see Fig. 3.2). T1 is an elongated radio galaxy of 527 kpc in extension at 1283 MHz, with the head coincident to the north-west cold front, small-scale undulations along its length and a gradient in the spectral index (from $\alpha = 0.61 \pm 0.05$ near to the core, to a steeper value of $\alpha = 2.49 \pm 0.09$ in the external regions; Riseley et al., 2024). T2 is located to the north of the cluster center, with a bulb-like structure extending north-west away from the host galaxy, that narrows and then widens into a diffuse and larger tail, with a gradient in the spectral index ($\alpha = 0.71 \pm 0.06$ associated with the host galaxy, becoming $= 0.99 \pm 0.05$ in correspondence to the bulb; where the tail widens again, the spectrum is steeper with a typical value of $\alpha = 1.41 \pm 0.06$, and, finally, where the tail fans out, the spectrum is again steeper with a typical value of $\alpha = 2.08 \pm 0.06$; Riseley et al., 2024). Detailed analysis on these two radio sources has been performed recently by Bruno et al., 2024. Moreover, there is a defined FRII galaxy, 7C 1557+2712, located in the south-east side of the cluster, with double-sided radio jets, bright hotspots and fainter diffuse lobes, two WATs that are not cluster members, W1 and W2, and the galaxy groups G (a blend of discrete radio sources at $z \sim 0.094$), located in the north-east to the cluster center, and C, located in the south-east (see Fig. 3.2; Venturi et al., 2017).

3.1 Aim of this Thesis

The aim of this study is to perform a radio analysis in polarisation of A2142, in order to investigate the RM distribution on background and cluster polarised synchrotron sources, e.g. radio galaxies, and derive, for the first time, the magnetic field intensity and profile in the ICM of A2142.

In this thesis work, we used high-sensitivity MeerKAT L-band (1283 MHz) data, which were previously processed and published in continuum by Riseley et al., 2024, but **imaged here for the first time in polarisation**. We have applied the RM synthesis technique to derive the RM for the polarised sources and created the RM map in order to study the average RM and the RM dispersion radial profiles (Ch. 4). By doing the comparison of the outcomes with simulated mock RM maps obtained with modeled 3D magnetic fields, we found the best-fit radial profile and put constraints on the intensity of the magnetic field in the ICM of A2142 (Ch. 5).

Throughout the thesis a ΛCDM cosmology is assumed, with $H_0 = 70$ km s^{-1} Mpc^{-1}, $\Omega_{\rm M} = 0.3$ and $\Omega_\Lambda = 0.7$. This translates to a luminosity distance of $D_{\rm L} = 408.6$ Mpc and a scale of 1.669 kpc/$''$ at the cluster redshift $z = 0.0894$.

Chapter 4

Imaging and RM Synthesis Technique

In this Chapter, we will present the measurement sets used in this thesis work (Sec. 4.1) and the data analysis we performed. The first part is dedicated to the imaging procedure on pre-calibrated data through the `WSClean` software, described both theoretically and practically (Sec. 4.2). In the second section (Sec. 4.3), we will present the application of the RM synthesis technique (discussed in Sec. 2.2) on the obtained images, whereas the last paragraph presents the final maps used for the RM analysis and the first results and considerations on the magnetic field properties (Sec. 4.4).

4.1 Measurment Sets

A2142 was observed with the MeerKAT interferometer in the L-band frequency range under the Project ID (PID) SCI-20210212-CR-01 (P.I. Riseley). Due to the high DEC of A2142, the team performed two observations to achieve the target sensitivity, resulting in a total on-source time of 5.5 hours. Tab. 4.1 reports the observations specifics.

Capture b. ID	Bandwidth [MHz]	Central freq. [MHz]	Obs. date
(1)	(2)	(3)	(4)
1633862771	872 - 1712	1283	2021 Oct. 10
1636710370	872 - 1712	1283	2021 Nov. 12

Table 4.1: List of the measurement sets used in this work. 1: capture block ID of the observation. 2: bandwidth range (L-band) of the observation. 3: central frequency of the observation. 4: year, month and day of the observation.

For the calibration, they adopted the Containerized Automated Radio Astronomy Calibration (`CARACal`) pipeline, which employs calibration tasks from the Common Astronomy Software Application (`CASA`) package. We refer to Riseley et al., 2024 for further details and references on the reduction and self-calibration of the data.

4.2 Imaging with `WSClean`

This thesis work begins after the calibration procedure with the production of the images in polarisation necessary for the application of the RM synthesis technique (Sec. 2.2). The images have been obtained with the `WSClean v3.4.0` ('w-Stacking Clean') software[1] (Offringa et al., 2014, 2017), a wide-field interferometric imager that uses the w-stacking as an alternative for the w-projection algorithm[2]. Hereinafter, the main `WSClean` tasks employed in this part of the thesis will be presented and then discussed in Sec. 4.2.5.

4.2.1 Briggs Weighting

Before computing the Fourier transform and producing an image, the (u, v) data must be interpolated onto a regular (u, v) grid, whose cells are centered on the grid points. Each data point is associated with the nearest grid point through the so-called *cell-averaging* and the number of points averaged in a cell decreases with increasing (u, v) distance, as the antennas make up more short baselines than long ones. Therefore, a weight is usually applied to each gridded visibility cell to compensate for the local density of ungridded visibilities (Thompson et al., 2017).

The widely-used weighting schemes are different and are chosen depending on the scientific goal. With the *natural weighting*, each visibility, k, is given a weight, W_k, inversely proportional to the noise variance of the visibility itself, σ_k^2, (i.e. all weights are equal to 1, as the noise is usually uniformly distributed in the image)

$$W_k = \frac{1}{\sigma_k^2}, \tag{4.1}$$

and then summed over the (u_k, v_k) cell. Since the shortest baselines are sampled the most, this weighting gives optimum surface brightness sensitivity, while the PSF is poor and the sidelobes are high, resulting in degraded spatial resolution. This kind of approach is generally used to recover the extended emission, instead the *uniform weighting* is generally adopted to resolve the small-scale structures. In this case, each visibility is given a weight inversely proportional to the sample density of the cell at which it belongs (i.e. the number of visibility data points in each grid cell)

$$W_k = \frac{1}{\sigma_k^2 \ \rho(u_k, v_k)}. \tag{4.2}$$

Therefore, each cell is corrected such that its weight is independent of the number

[1] available at https://gitlab.com/aroffringa/wsclean.

[2] we refer the reader to the App. A to have a general view on the radio interferometry and observation.

of visibilities inside. In this case, the longer baselines are weighted more than in the natural weighting scheme, the PSF has lower sidelobes and its FWHM is smaller, providing better spatial resolution, whereas the surface brightness sensitivity is reduced.

To find a compromise between spatial resolution and surface brightness sensitivity, Briggs, 1995 proposed an alternative kind of weighting, called 'Briggs' or 'robust weighting', that provides a smoothly varying combination between *uniform* and *natural*, that can be controlled with the *robustness* parameter, R. In this case, the cell weight, w_k, is given by

$$w_k = \frac{1}{S^2 + \sigma_k^2}, \quad S = \frac{(5 \times 10^{-R})^2}{\bar{w}}, \tag{4.3}$$

where $\bar{w}$ is the average variance weighting factor and, in modern softwares, R can assume values between -2 and +2, respectively close to uniform and natural weighting.

In `WSClean`, the Briggs weighting scheme can be selected by specifying the parameter `-weight briggs` followed by the value of R.

4.2.2 *w*-stacking

The w-stacking takes into account the w-term that describes the deviation of the sky curvature from a perfect plane, using a different approach than the w-projection. Instead of applying a convolution in the (u, v) space (i.e. the (u, v) samples are not convolved with a w-term correcting kernel before the Fourier transform), the w-stacking method grids the visibilities on different w-layers and performs the w-corrections (i.e. multiplication) after each inverse Fourier transform.

An interferometer samples the *complex visibility function*, V, as

$$V(u, v, w) = \int\int \frac{A(l, m) I(l, m)}{\sqrt{1 - l^2 - m^2}} e^{-2\pi i (ul + vm + w(\sqrt{1-l^2-m^2}-1)} \mathrm{d}l\mathrm{d}m, \tag{4.4}$$

where $(u,\ v,\ w)$ is a baseline coordinate in the coordinates system of the antennas, A is the primary-beam function, I is the sky brightness distribution and $(l,\ m)$ are the cosine sky coordinates. For small Field of Views (FOVs), the term $\sqrt{1 - l^2 - m^2}$ is close to 1 and eq. 4.4 is an ordinary two-dimensional (2D) Fourier transform. However, if this term exceeds unity, it is not possible to estimate the sky brightness by simple Fourier inversion of the measured visibility.

Eq. 4.4 can be re-written by defining the sky surface brightness before *primary-beam correction* (Sec. 4.2.4), $I'(l, m) = A(l, m) I(l, m)$, as

$$V(u, v, w) = \int\int \frac{I'(l, m) e^{-2\pi i w(\sqrt{1-l^2-m^2}-1)}}{\sqrt{1 - l^2 - m^2}} e^{-2\pi i (ul + vm)} \mathrm{d}l\mathrm{d}m. \tag{4.5}$$

This is an ordinary 2D Fourier transform going from the (u, v) space to the (l, m) space,

and can be inverted to get the dirty image, $I'(l,m)$, for a specific w-term

$$\frac{I'(l,m)}{\sqrt{1-l^2-m^2}} = e^{2\pi i w(\sqrt{1-l^2-m^2}-1)} \int\int V(u,v,w) e^{2\pi i(ul+vm)} \mathrm{d}u\mathrm{d}v. \tag{4.6}$$

Integrating both sides of eq. 4.6 over w_{min} to w_{max}, the minimum and maximum value of w respectively, it is possible to recover the signal for all the possible w-terms as

$$\frac{I'(l,m)(w_{max}-w_{min})}{\sqrt{1-l^2-m^2}} = \int_{w_{min}}^{w_{max}} e^{2\pi i w(\sqrt{1-l^2-m^2}-1)} \mathrm{d}w \int\int V(u,v,w) e^{2\pi i(ul+vm)} \mathrm{d}u\mathrm{d}v. \tag{4.7}$$

The final step consists in making the (u, v, w) parameters discrete, so that the integration over u and v becomes an inverse Fourier transform and the integration over w becomes a sum. In this way, it is possible to correct for large FOVs on the plane of the sky and avoid the planar-sky approximation.

4.2.3 Polarimetric Deconvolution and Deconvolution Algorithms

In order to apply the RM synthesis technique, we need to produce images of the Stokes Q and Stokes U polarisations of a measurement set at different frequencies. After that, the constructed Q- and U-frequency cubes will be Fourier transformed with an external tool as explained in Sec. 4.3.

`WSClean` allows the cleaning of Stokes I, Q, U and V polarisations individually or can jointly deconvolve them, improving the quality of the polarised images. In the latter case, the peaks and the components shape are searched in the integrated values over the selected Stokes parameters (e.g. in QU or IQUV space), but the clean components are subtracted from each polarisation once their location is selected.

The joint polarisation deconvolution can be implemented by specifying `-pol iquv` and `-join-polarizations` parameters in the code line and can be combined with other deconvolution algorithms, such as the *wideband multi-frequency deconvolution* and the *multi-scale deconvolution*.

Wideband Multi-frequency Deconvolution

Since MeerKAT and other radio telescopes have large bandwidths, variations of the sources spectrum and of the PSF within the band must be considered. Solutions consist in dividing the full-bands into evenly-spaced channels (i.e. sub-bands) and performing the cleaning jointly by searching for the peak in the joint residual map, and deconvolving every channel and polarisation taking into account the different PSFs. This multi-frequency deconvolution method is called 'joined-channel deconvolution' in `WSClean` and is applied by specifying the `-join-channels` and `-channels-out` parameters. Essentially, the approach uses the full-bandwidth (i.e. it combines the images by

summing over the channels) to determine the location of the clean components, which decreases the chance of selecting noise peaks or sidelobes, and constructs the model, the dirty and the PSF images for each output channel. The stopping thresholds of the iterations are relative to the frequency-integrated (MFS) image (i.e. the weighted sum of all the channels), that, thanks to this method, is improved by adjusting the weight of the individual frequencies.

Multi-scale Deconvolution

The second algorithm adopted is a scale-dependent deconvolution, that accounts for both small and large scale structures, i.e. different angular scales, that are present in a single image. The *multi-scale* clean was initially presented by Cornwell, 2008 and is considered as an improvement with respect to the standard cleaning algorithms (e.g. Högbom, 1974; Clark, 1980; see App. A), as the model is better reconstructed using components with different scales. So, the residuals are lower and the negative bowls are minimised and/or completely removed. The major iterations are performed by following the *Cotton-Schwab* method (Schwab, 1984), where the clean components are subtracted from the ungridded data in the visibility domain. The residual visibilities are then imaged to produce a new residuals image and the next iteration of deconvolution can proceed.

The algorithm starts with the creation of dirty images at different scales by convolving the dirty image with the corresponding scale kernels and selects the scale to be cleaned by finding the convolved dirty image with the highest maximum (or peak). After that, the PSF is convolved with the best-fitting scale and a subminor loop (like the Högbom clean) starts and performs a number of iterations with the current scale, until the maximum peak has been reduced by a specific threshold. When the subminor loop ends, the algorithm selects a new scale to clean, until the major iteration threshold is reached.

The multi-scale deconvolution algorithm can be implemented by specifying the `-multiscale` parameter in the code line and can be combined with the multi-frequency deconvolution and with the application of a mask.

4.2.4 Primary-beam Correction

In radio observations, the image obtained through the imaging and the deconvolution steps is a representation of the sky surface brightness modified by the primary-beam response of the antennas. The primary-beam is typically similar to a Gaussian function with sidelobes and is well known for every instrument. It can be considered as the antennas sensitivity that is not uniformly distributed, but depends on the direction of the incoming radiation and is assumed to be identical for every receptor in the array.

It can be corrected from an observation by dividing the final deconvolved image by the primary-beam pattern.

`WSClean` can calculate and correct for the primary-beam of MeerKAT antennas in case of L-band observations[3], by specifying the `-apply-primary-beam` parameter in the code line.

4.2.5 Polarisation Images and Discussion

As mentioned above, the images in total intensity and in polarisation (Stokes I, Q, U and V) have been created by performing the joint polarimetric deconvolution on the two measurement sets simultaneously. In order to create the polarisation cubes for the following steps, we have applied the multi-frequency deconvolution by cleaning joinedly 256 channels, which also yields a better reconstruction of the spectrum, as every sub-band has its own PSF and is cleaned individually.

The list of parameters adopted for the imaging step and specifics of the final images, e.g. the image size (in pixels), the angular scale of the pixels (in arcseconds) and the number of iterations (that sets the maximum number of minor cleaning loops), are reported in Tab. 4.2. We have checked from the clean and the residuals images that all the sources have been cleaned down to a threshold of 3 times the RMS noise standard deviation[4] (in Jy), $\sigma_{\rm RMS}$, to make sure that no additional components were left to be cleaned, especially in correspondence of the boundaries of the maps. We have exploited the Briggs weighting by specifying the `-weight briggs -0.5` parameter in order to recover both small scale and extended emission in the observations and then corrected for the primary-beam. We have also tried the multi-scale deconvolution, but the first attempts were unsuccessful, as the cleaning produced extremely high flux model values ('diverging clean'). This may happen if `WSClean` automatically uses very large scales in multi-scale deconvolution. To solve this problem we have specified the adopted scales with `-multi-scale-scales 0, 5, 7, 10`[5]. At the nominal frequency of 1283 MHz, these scales correspond to 0, $\sim$ 0.8, $\sim$ 1 and $\sim$ 1.5 times the PSF. Then, we have applied a mask in order to perform a deeper cleaning. The mask has been created from the MFS Stokes I image of 20 channels with a threshold of $3\sigma_{\rm RMS}$ and then used in combination with `-auto-mask 1.5`. In this way, `WSClean` is forced to find the components only in the areas determined by the constructed mask and to reach the automask threshold.

The output of `WSClean` is a restored or clean image, a model image, a dirty image,

[3]other instruments are present in the *EveryBeam Library*, available at https://everybeam.readthedocs.io/en/latest/.

[4]of the residuals image and is calculated automatically by the algorithm before the start of every major deconvolution iteration, if the parameter `-auto-threshold 3` is specified.

[5]each value, α, is given in units of pixels and the correspondent scale kernel is a Gaussian with FWHM equal to $\approx 0.45\alpha$.

Nr. of channels	256	Threshold	$3\sigma_{\mathrm{RMS}}$
Sub-bandwidth	3.28 MHz	Pixel scale	$2''$
Nr. of iterations	50 000	Briggs weighting	-0.5
Image size	1300 x 1300 pxl^2	`mgain`[6]	0.8

Table 4.2: List of parameters and specifics adopted for the imaging step.

and a residuals image for every channel and for every polarisation. The PSF image, instead, is common for all Stokes. We list below some relevant observations about the images:

- by inspecting Stokes I images of all channels sequentially, some of the known sources presented in Ch. 3 are visible, as well as other powerful radio galaxies in the background of the cluster. Moreover, it is appreciable a decrease in their emission intensity according to the power-law decline of synchrotron radiation at higher frequencies (along the bandwidth we are considering);
- by inspecting the Stokes Q and U images of all channels sequentially, we have noticed some features in correspondence of the radio galaxies and their lobes that change across the bandwidth. This is consistent with the fact that Stokes Q and U intensities may assume both positive and negative values due to the presence of the Faraday rotation. Instead, for Stokes V there are only barely visible fluctuations, but this is reasonable as we do not expect any circular polarisation from synchrotron radiation[7];
- by inspecting the PSF images of all channels sequentially, it is possible to observe that the shape and the FWHM become smaller with increasing frequency. This is consistent with the fact that smaller wavelengths produce smaller PSFs.

4.2.6 Image Preparation for the RM Synthesis

Before starting with the RM synthesis technique, the sub-band Stokes Q and U images must be convolved to the same resolution in order to create the cubes in frequency. With this purpose, we have extracted the restoring beam of every channel and plotted the distribution of the major (BMAJ) and minor (BMIN) axes across the bandwidth (Fig. 4.1): some of the sub-bands have been totally flagged during the calibration procedure and, in fact, show $0''$ both in BMAJ and BMIN, as they do not have any restoring beam; other channels have been heavily flagged or are particularly noisy and present values up to 100s$''$ in BMAJ. In order to include the majority of them, not to degrade the resolution and to avoid the consequent beam depolarisation as much as

[6] at every iteration of the cleaning, the peak flux is reduced by 80% until a new major iteration is started.

[7] measured degrees of Stokes V usually range between 0.1% and 0.5% of the Stokes I intensity (Ruszkowski & Begelman, 2002 and references therein).

possible, we have finally chosen a circular beam of 20″x 20″ and smoothed the images with the `imsmooth` `CASA` task, resulting in 206 channels.

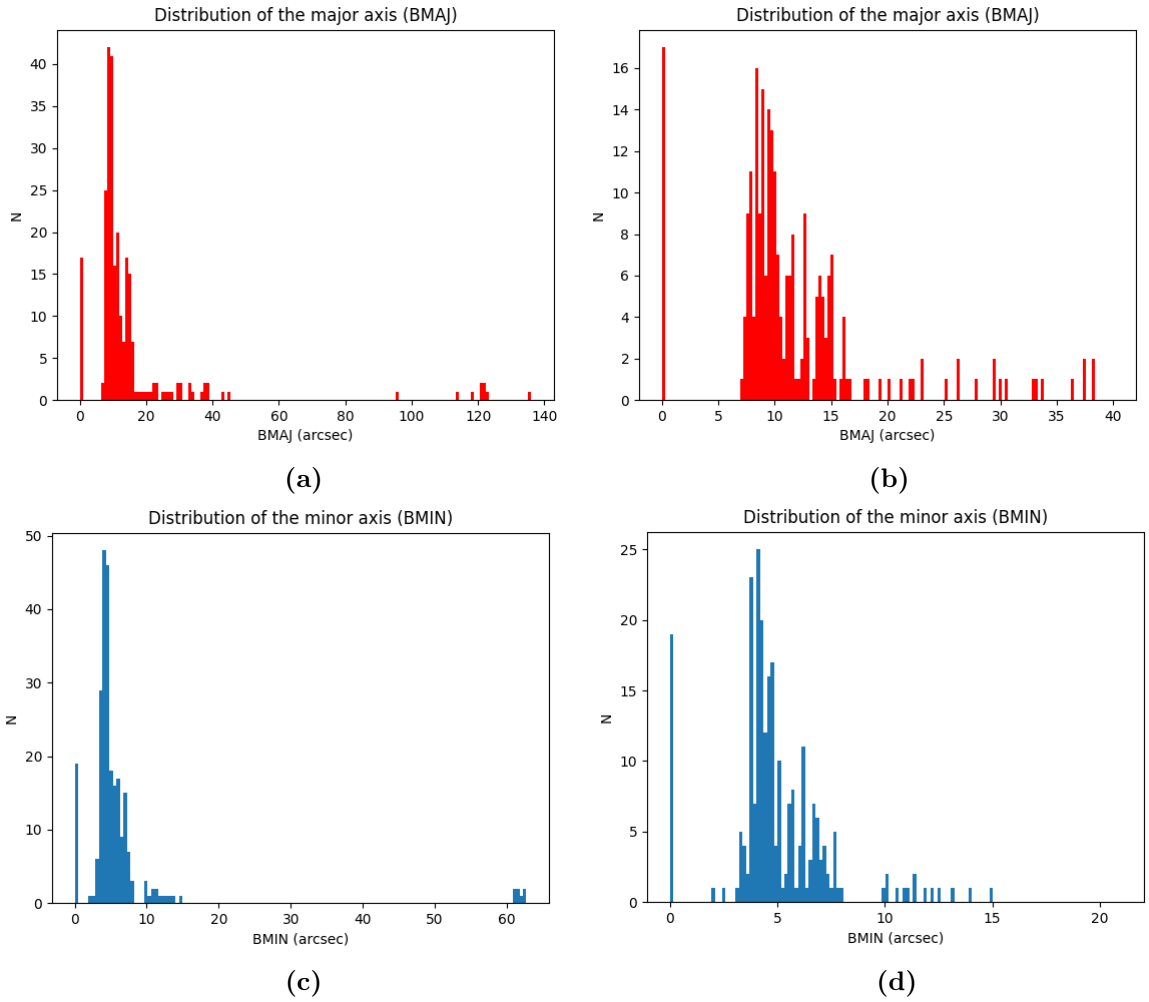

Figure 4.1: Distribution of the restoring beam axes, BMAJ and BMIN, of the 256 channels. *Panel (a):* Total distribution of the major axis (BMAJ). The majority of the channels have BMAJ within 60″. *Panel (b):* Zoom of the total distribution of BMAJ within 40″. *Panel (c):* Total distribution of the minor axis (BMIN). The majority of the channels have BMIN within 20″. *Panel (d):* Zoom of the total distribution of BMIN within 20″.

Then, we have created the Stokes Q and U cubes (with the correspondent list of frequencies) and removed the bad channels depending on the statistics of each image (i.e. the ones with noise above 5 times the RMS noise over the median noise), resulting in 191 channels (15 blanked and 65 totally removed). Finally, the cubes have been rebinned for computational load to the desired pixel scale using the `imrebin` `CASA` task with *factor=[2,2,1,1]*. In this way, we have halved the size of the image from 1300 to 650 pixels per side and obtained 5 pixel per beam rather than 10, since the pixel scale goes from 2″ to 4″. We show in Fig. 4.2 the final Stokes I, Q and U images after the convolution and the rebinning for three channels, respectively at 1283 MHz, 965 MHz and 918 MHz. The zoom of the Stokes Q and U maps on some sources is provided in Fig. 4.3.

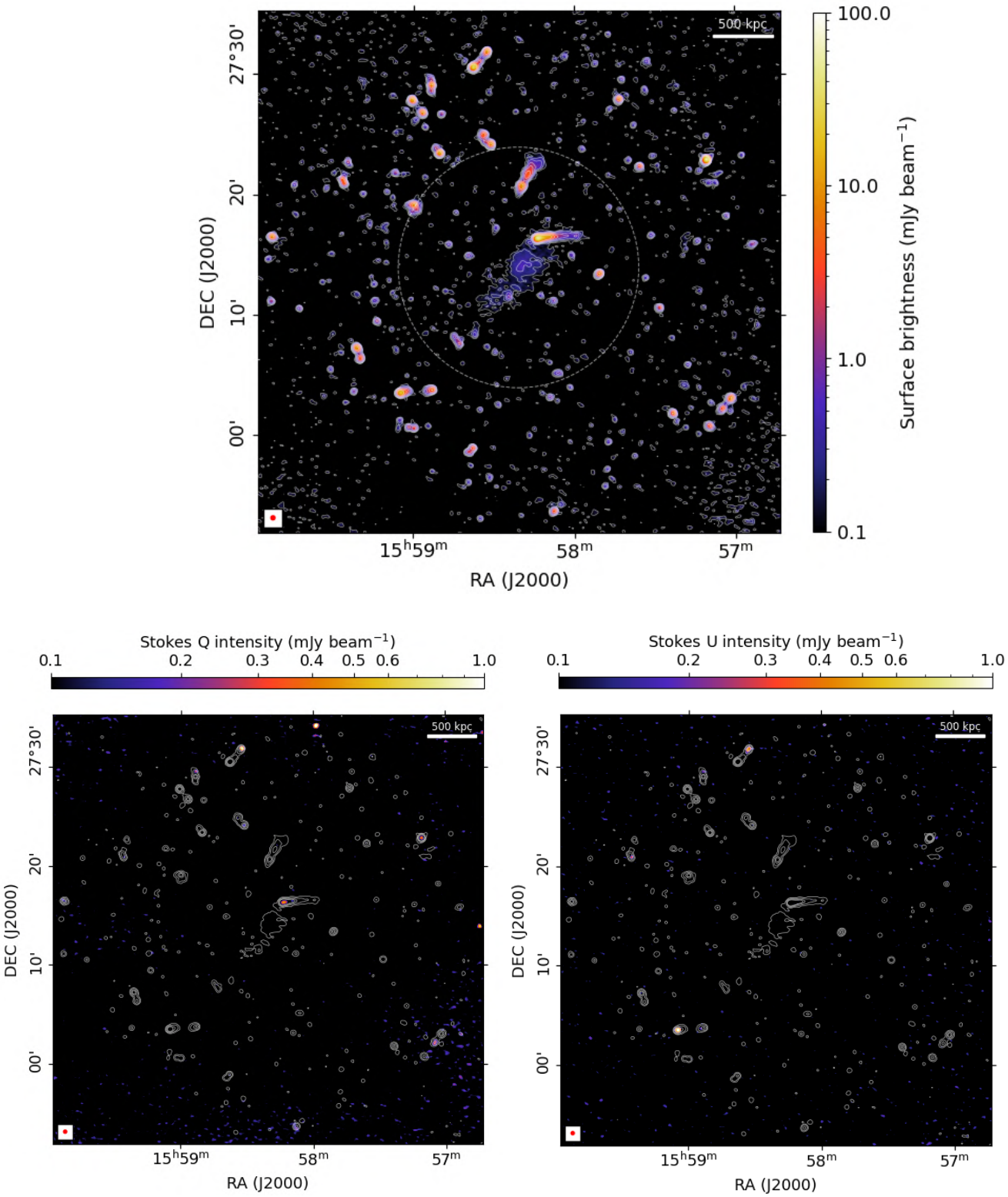

Figure 4.2: Total intensity and polarisation radio images of A2142. *Top:* Stokes I image at 1283 MHz, with overlaid radio contours (1283 MHz), from $3\sigma_{\rm I}$ and scaling by a factor of 2. It is appreciable the emission from both radio galaxies and the two radio halos, H1 and H2. Dashed circle corresponds to the reference distance of 1 Mpc from the cluster center. *Bottom left:* Stokes Q image at 965 MHz, with overlaid radio contours (1283 MHz), from $6\sigma_{\rm I}$ and scaling by a factor of 4. *Bottom right*: Stokes U image at 918 MHz, with overlaid radio contours (1283 MHz), from $6\sigma_{\rm I}$ and scaling by a factor of 4. The images have common angular resolution of 20″ x 20″ (33.4 kpc), image size of 650 pixel per side and pixel scale of 4″ after rebinning. Spatial scales and resolution beam are reported on the edges of the images.

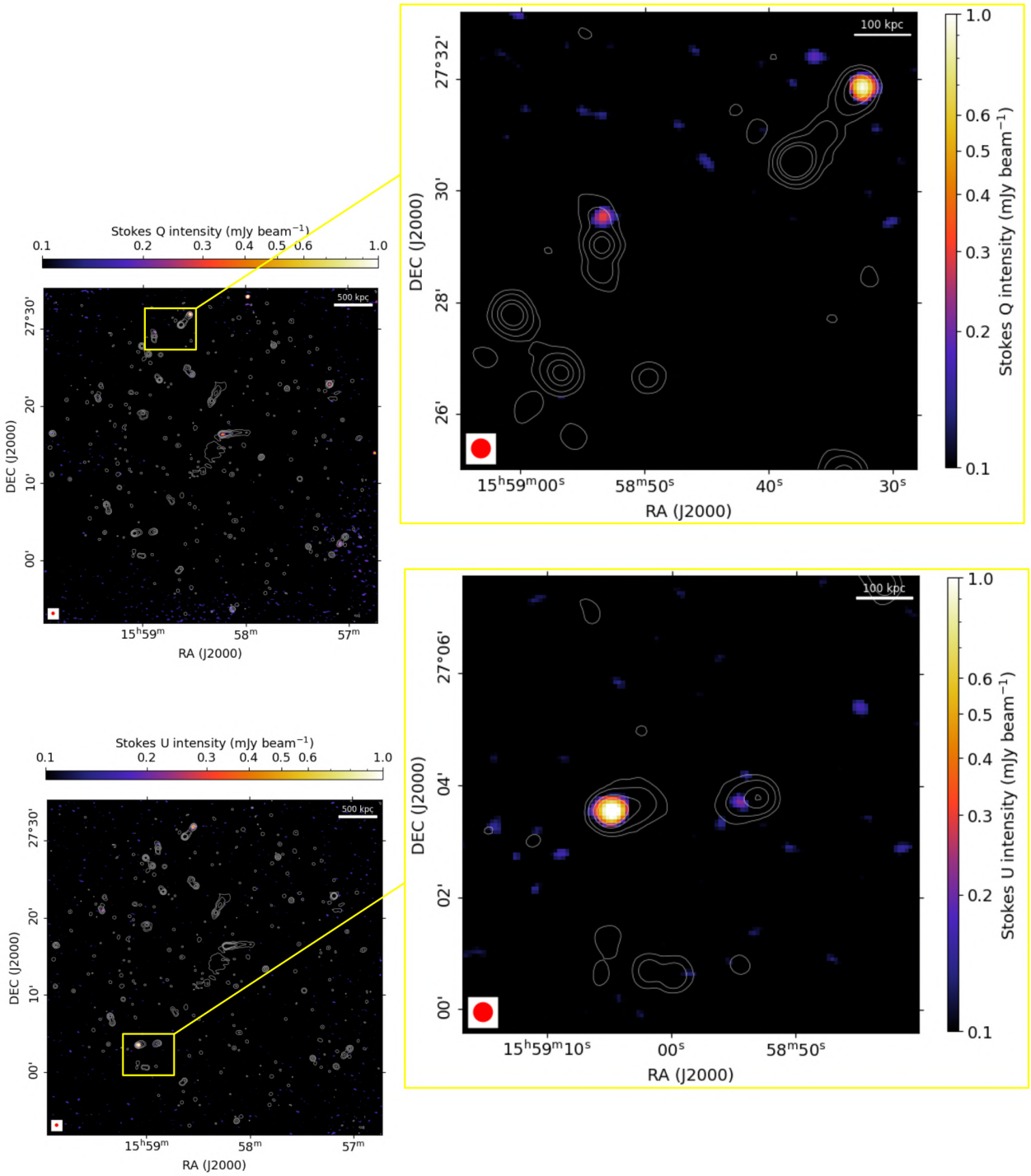

Figure 4.3: Zoom of the polarisation maps (Fig. 4.2) in correspondence of some sources. *Top panel:* Stokes Q intensity. *Bottom panel:* Stokes U intensity. Spatial scales and resolution beam of $20'' \times 20''$ are reported on the edges of the images.

4.3 RM Synthesis Results

In order to apply the RM synthesis technique and create the FDF cubes, we must compute some parameters *a priori*, that have been presented in Sec. 2.2 and will be inserted in the `rmsynth3d` algorithm. They are summarised in the following table.

$\delta\phi$	$\lvert\phi_{max}\rvert$	$\Delta\phi_{max}$	$\sigma_{\rm P}$	$\mathrm{err}_{\rm RM}$
[rad m^{-2}]	[rad m^{-2}]	[rad m^{-2}]	[μJy beam^{-1}]	[rad m^{-2}]
(1)	(2)	(3)	(4)	(5)
41.82	2004.18	97.84	4.93	3.48

Table 4.3: List of theoretical parameters for the RM synthesis technique. 1: theoretical FWHM of the RMTF. 2: maximum observable ϕ. 3: maximum observable scale in ϕ. 4: theoretical noise in polarisation. 5: theoretical noise in RM at 6 S/N ratio.

The theoretical noise in polarisation, $\sigma_{\rm P}$, is derived from the sum in quadrature of the noise in the single channels (i.e. the mean of the Stokes Q and U noises in every channel i), $\sigma_{list,i}$, whereas the theoretical noise in RM, $\mathrm{err}_{\rm RM}$, is computed as the Half-Width-Half-Maximum (HWHM; i.e. half the FWHM) of the RMTF main lobe divided by the desired signal-to-noise (S/N) ratio (here 6[8]),

$$\sigma_{\rm P} = \frac{1}{\sqrt{\sum_{i=1}^{191} \frac{1}{\sigma^2_{list,i}}}}, \quad \mathrm{err}_{\rm RM} = \frac{1}{2}\frac{\delta\phi}{6} = \frac{\delta\phi}{12}. \tag{4.8}$$

As presented above, the algorithm takes in input the Stokes Q and U cubes and the associated frequency list. We have specified some additional arguments based on the obtained theoretical values, such as the range of Faraday depths over which the FDF is computed, 1000 rad m^{-2}, and the sample spacing in ϕ, 3 rad m^{-2}. Here, we have halved the maximum observable ϕ to reduce the computational load.

The outputs of the RM synthesis are:

- the total (amplitude), real (Stokes Q) and imaginary (Stokes U) cubes of the dirty FDF in Faraday space ranging from -999 to $+999$ rad m^{-2}, in steps of 3 rad m^{-2} (667 channels). In case the maximum observable ϕ is not a multiple of the sample spacing, the algorithm decreases it to the nearest multiple;
- the RMTF resolution (FWHM), 45.87 rad m^{-2}, equal in each pixel and similar to the theoretical value, since each channel is weighted by a different $W(\lambda^2)$;

[8] which corresponds to a Gaussian significance level of about 5σ according to Hales et al., 2012.

- the total, real and imaginary cubes of the RMTF in the Faraday space ranging from -2001 to $+2001$ rad m^{-2}, with the same structure as the FDF, but with twice the channels in Faraday depth (Fig. 4.5);
- a map of the maximum polarised intensity ($|\tilde{F}(\phi_{peak}|$) in each pixel. By inspecting it, we have noticed a bubble-like structure in the top-left side of the image, which has not a diffuse Stokes I counterpart. It could be associated to a Galactic component, hereafter called 'Galactic bubble' (see Fig. 4.4);
- a map of the Faraday depth corresponding to the maximum polarised intensity in each pixel ($\phi_{\rm peak}$), which represents the equivalent of the RM map in the case of Faraday-simple screen.

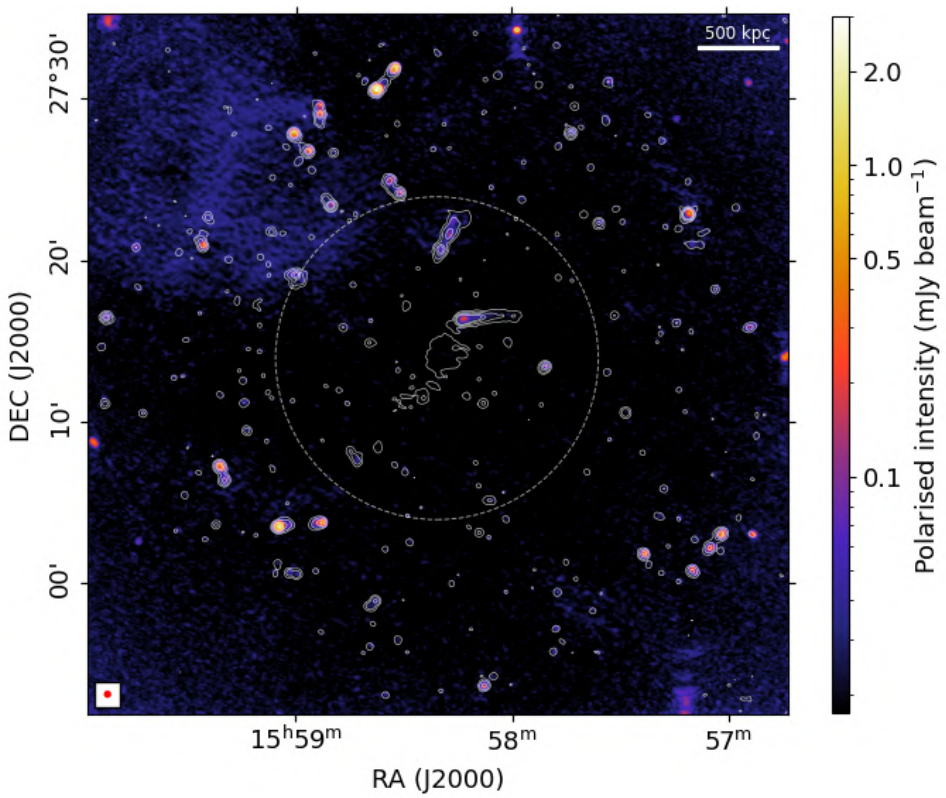

Figure 4.4: Map of the maximum polarised intensity in each pixel obtained with RM synthesis technique, with overlaid radio contours (1283 MHz), from $6\sigma_{\rm I}$ and scaling by a factor of 4. In the image are distinguishable the two head-tail radio galaxies, T1 and T2, bright hot-spots of background sources and the 'Galactic bubble' in the top-left side. Dashed circle corresponds to the reference distance of 1 Mpc from the cluster center. Spatial scales and resolution beam of $20'' \times 20''$ are reported on the edges of the image.

At this point, we have computed the RMS noise level of the real and imaginary part of the dirty FDF from the edges of the cubes, $|\phi| > 750$ rad m^{-2}, where there was not contamination from the sidelobes of the sources. We have obtained:

- $\sigma_{\rm Q} = 4.74$ μJy beam^{-1} as RMS noise for the Stokes Q cube

- $\sigma_{\mathrm{U}} = 4.70\ \mu\mathrm{Jy\ beam}^{-1}$ as RMS noise for the Stokes U cube
- $\sigma_{\mathrm{QU}} = \dfrac{\sigma_{\mathrm{Q}} + \sigma_{\mathrm{U}}}{2} = 4.72\ \mu\mathrm{Jy\ beam}^{-1}$ as average RMS noise,

which is slightly lower with respect to the theoretical noise, σ_{P}, found above, and then used 8 times σ_{QU} ($37.74\ \mu\mathrm{Jy\ beam}^{-1}$) as the threshold for `rmclean3d`.

The produced outputs are:

- the total (amplitude), real (Stokes Q) and imaginary (Stokes U) cubes of the cleaned FDF in Faraday space, with the same format as the dirty FDF ones;
- the total (amplitude), real (Stokes Q) and imaginary (Stokes U) cubes of the complex components found by the algorithm in Faraday space, with the same format as the clean FDF ones;
- a map (with same dimensions as the cubes, but without the Faraday depth axis) showing the number of iterations used for each pixel.

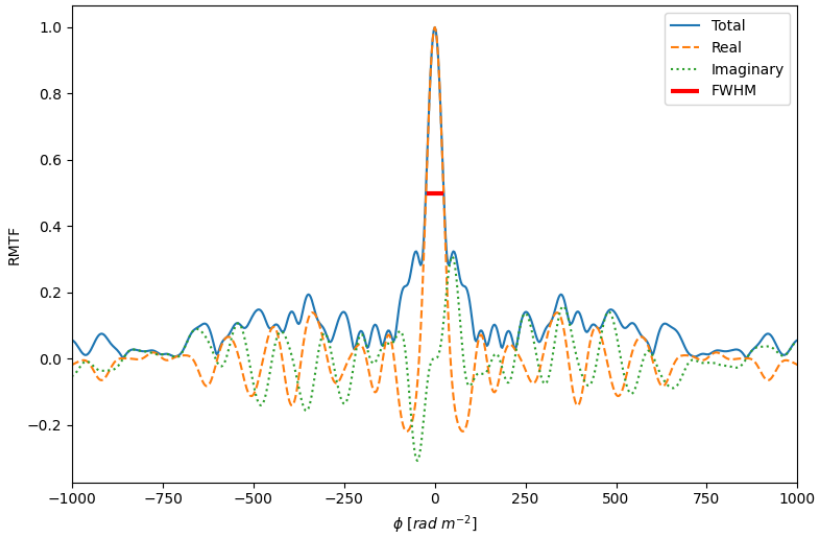

Figure 4.5: The RMTF in Faraday space. The total, real and imaginary part are reported in *blue*, *orange* and *green*, respectively. The FWHM is also shown in *red* as a reference.

We report in Fig. 4.6 the FDF dirty spectrum, the FDF clean spectrum and the clean components taken from one pixel of 3 different sources and from a region of the 'Galactic bubble'. Fig. 4.6a is associated to the central radio galaxy, T1, and shows a clear double peak in polarisation above the $8\sigma_{\mathrm{QU}}$ threshold. We note that the algorithm has identified multiple components, whose superposition gives rise to the dirty FDF primary lobe. In this case, the FWHM is larger with respect to separation of the two peaks in the clean spectrum, i.e. we are not able to resolve the Faraday-complex spectrum. A possible scenario explaining what we got is the orientation of the tail of the radio galaxy seen in projection: the bended jets and lobes could be superimposed

on a single LOS and consist in a combination of Faraday-rotating and synchrotron-emitting media. Similar cases are reported in Fig. 4.6b for the second central radio galaxy, T2, and in Fig. 4.6c, associated to a bright hot-spot of a radio galaxy found on the top of the image. Finally, we have explored the 'Galactic bubble' region and found a very faint signal (Fig. 4.6d), not coming from any visible source in the background and is an evident example of Faraday-simple spectrum.

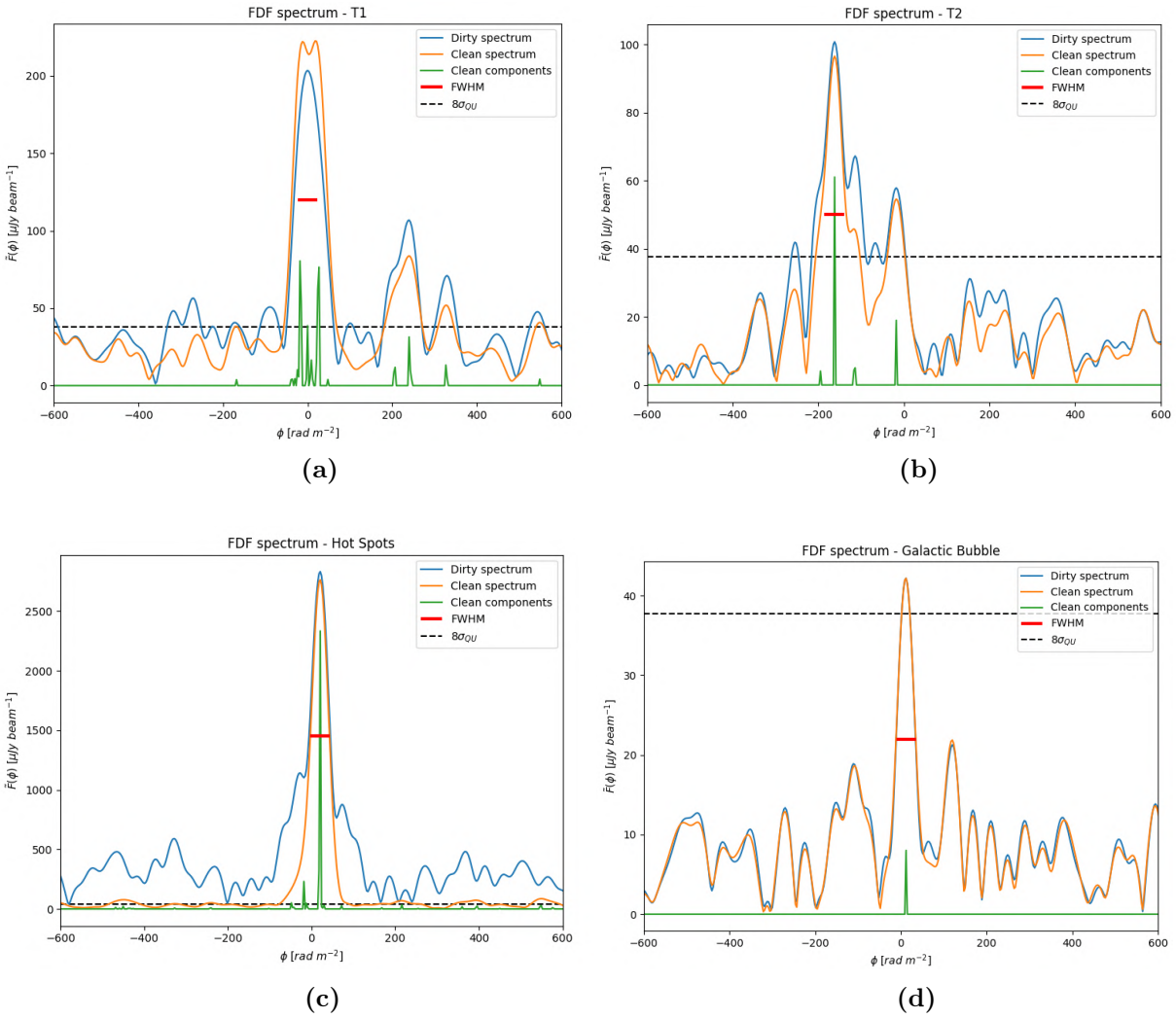

Figure 4.6: Reconstructed FDF spectrum taken from one pixel of 3 different sources and from a region of the 'Galactic bubble'. The dirty spectrum is shown in *blue*, the clean spectrum in *orange* and the clean components in *green*. The FWHM of the RMTF is reported in *red* and the $8\sigma_{QU}$ with the *black* dashed line as a reference. *Panel (a):* T1. *Panel (b):* T2. *Panel (c):* Hot-spot of a radio galaxy. *Panel (d):* region of the 'Galactic bubble'.

4.4 Final Maps and Discussion

At this point, we are ready to create the final maps for the further analysis on the RM and the fractional polarisation radial profiles.

All the images have been obtained by masking for $6\sigma_{\rm QU}$ and 3 times the noise in Stokes I intensity ($\sigma_{\rm I} = 3.26 \times 10^{-5}$ Jy beam^{-1}), in order to avoid noisy pixels. The RM map has been created by taking the Faraday depth corresponding to the peaks of the cleaned FDF cube and corrected for the Galactic Faraday rotation in the region of the cluster ($\rm RM_{Gal} = 4.10 \pm 1.13$ rad m^{-2}; Hutschenreuter et al., 2022). We have then produced the polarisation map with the maximum polarised intensity in each pixel from the cleaned FDF cube and corrected it for the *Ricean bias* (Wardle & Kronberg, 1974)

$$P = \sqrt{|\tilde{F}(\phi_{peak})|^2 - \sigma^2_{\rm QU}}, \tag{4.9}$$

since the linearly polarised intensity is always positive-defined as $P = \sqrt{Q^2 + U^2}$ and the noises in Stokes Q and U result in a positive value of P even if no signal is present. This leads to an over-estimation of the polarised intensity which we need to correct for and the noise statistic of P follows the Rice distribution (George et al., 2012). For the fractional polarisation map, instead, we have divided the obtained polarisation map by the total intensity MFS image of 20 channels, convolved to reach the same resolution and then rebinned to the same number of pixels.

Some first considerations are presented below:

- **RM map** (Fig. 4.7): we observe values ranging from -950 to $+960$ rad m^{-2} according to the different intensity and orientation of the magnetic field along the LOS and a patchy appearance, especially in correspondence to the resolved radio galaxies, due to the magnetic field components fluctuating on scales smaller than the source size; the RM distribution of the unresolved sources, instead, looks more uniform, which indicates that the magnetic field substantially changes on scales larger than the source size. Zooms of the RM map are provided in Fig. 4.9, 4.10 and 4.11 in correspondence to the sources considered in the further analysis (see discussion in Sec. 4.4.1);
- **fractional polarisation map** (Fig. 4.8)): by eye, there is a clear distribution of fractional polarisation, with values ranging from 0.25% to 50% and increasing towards the edges of the cluster; the radio galaxies seen in projection in the central regions (e.g. T1 and T2) show the lowest values and this is in agreement with larger RM dispersion in the cluster center; in case of T1, a further reduction may be caused by the internal Faraday depolarisation for the reasons discussed in the previous section; the highest percentage values are concentrated in the region of the 'Galactic bubble'. Zooms of the fractional polarisation map are provided in Fig. 4.12, 4.13 and 4.14 in correspondence to the sources considered in the further analysis (see discussion in Sec. 4.4.1);

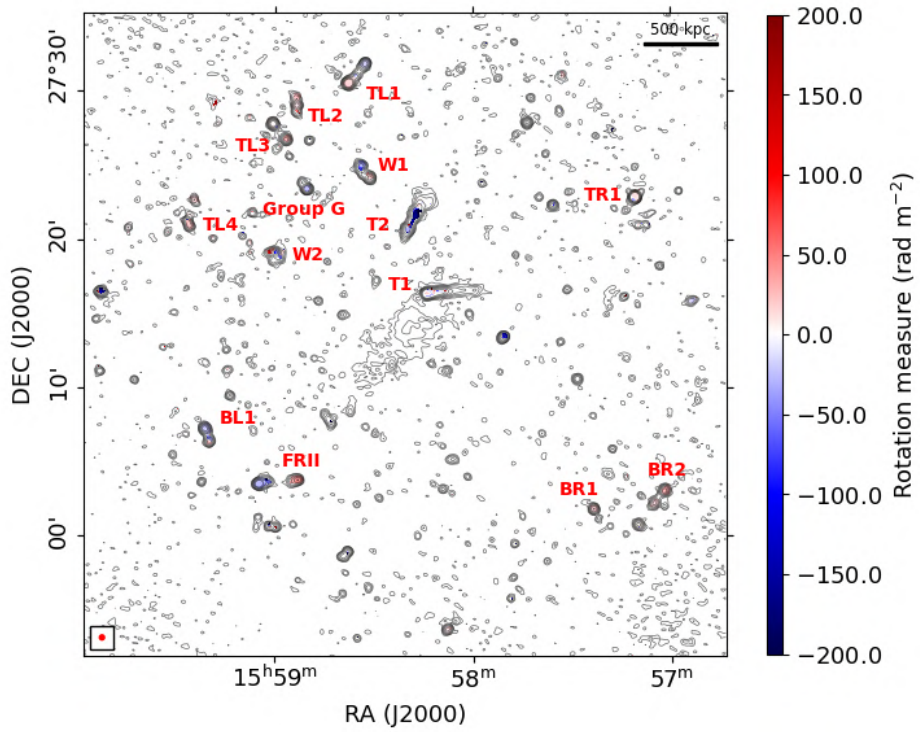

Figure 4.7: RM map of A2142, with overlaid radio contours (1283 MHz), from $3\sigma_{\rm I}$ and scaling by a factor of 2. The $6\sigma_{\rm QU}$ and $3\sigma_{\rm I}$ detection thresholds were imposed in polarisation and only pixels above them are shown. Values were corrected for the Galactic foreground rotation. Spatial scales and resolution beam of $20'' \times 20''$ are reported on the edges of the image.

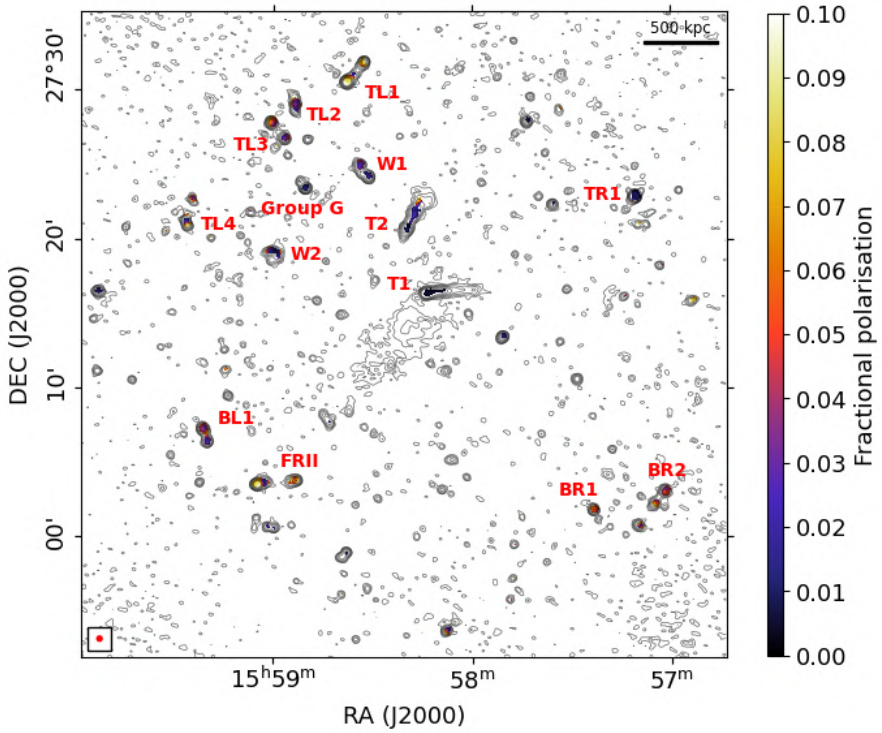

Figure 4.8: Fractional polarisation map of A2142, with overlaid radio contours (1283 MHz), from $3\sigma_{\rm I}$ and scaling by a factor of 2. The $6\sigma_{\rm QU}$ and $3\sigma_{\rm I}$ detection thresholds were imposed in polarisation and only pixels above them are shown. Values were corrected for the Ricean bias. Spatial scales and resolution beam of $20'' \times 20''$ are reported on the edges of the images.

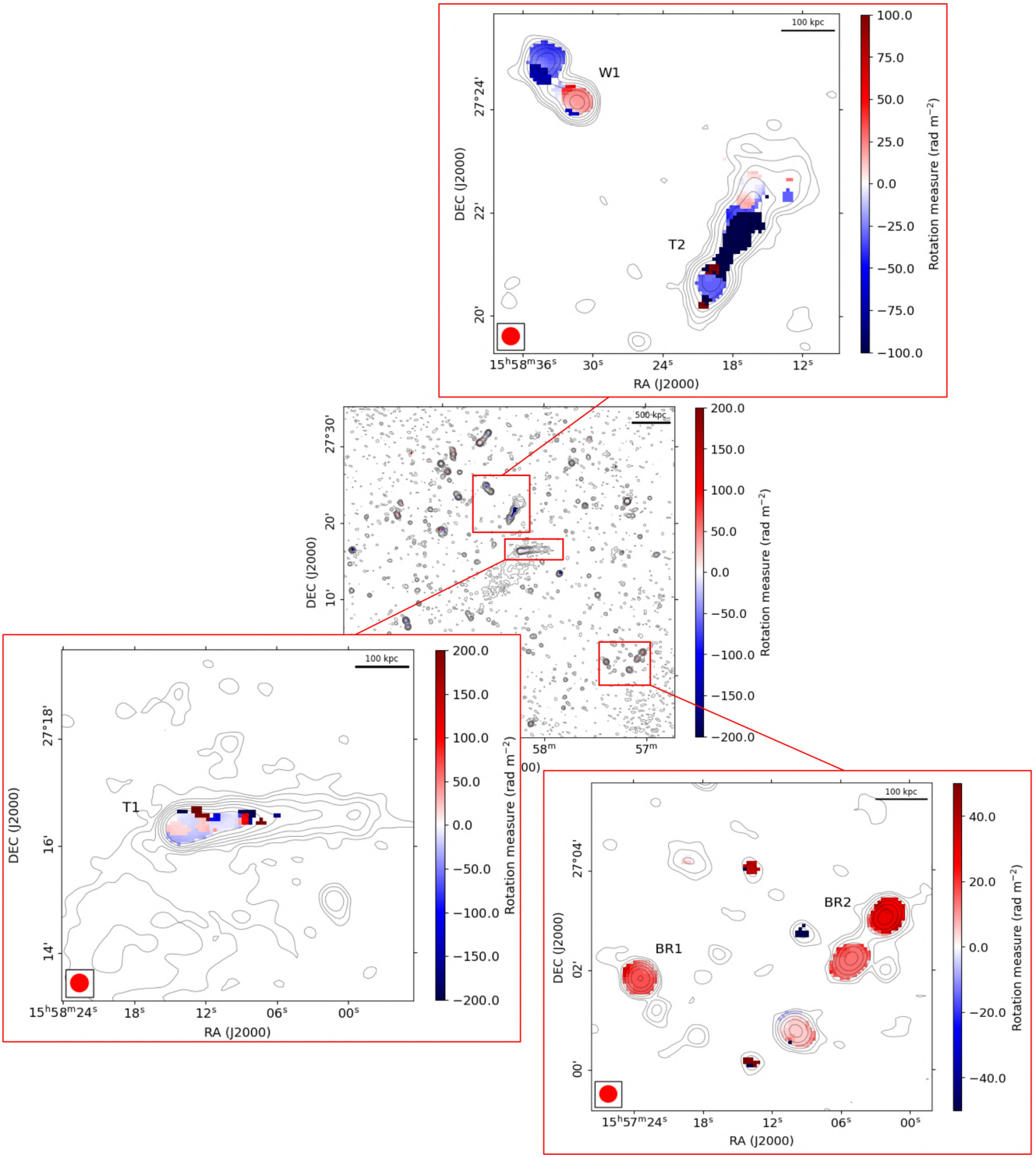

Figure 4.9: Zoom of the RM map (Fig. 4.7) in correspondence of some sources analysed in this work. *Top-right panel:* T2 and W1. *Bottom-left panel:* T1. *Bottom-right panel:* BR1 and BR2. Positive values refer to the magnetic field orientation along the LOS towards the observer, whereas negative values refer to an orientation away from the observer. The range of values shown in the panels may change from the principal map for a better visualisation of their distribution. Spatial scales and resolution beam of $20'' \times 20''$ are reported on the edges of the images.

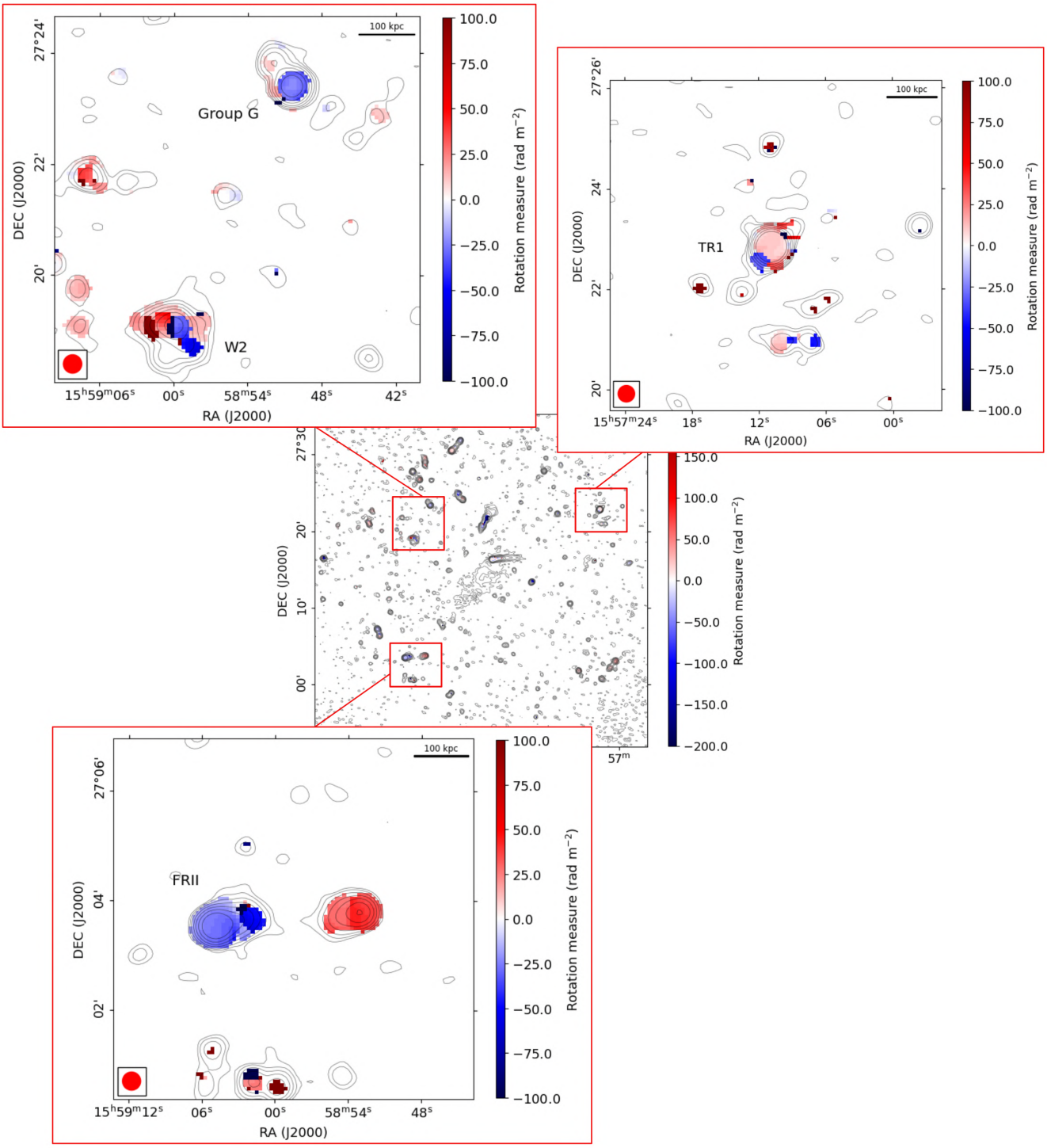

Figure 4.10: Zoom of the RM map (Fig. 4.7) in correspondence of some sources analysed in this work. *Top-left panel:* W2 and Group G. *Top-right panel:* TR1. *Bottom-left panel:* FRII. Positive values refer to the magnetic field orientation along the LOS towards the observer, whereas negative values refer to an orientation away from the observer. The range of values shown in the panels may change from the principal map for a better visualisation of their distribution. Spatial scales and resolution beam of $20'' \times 20''$ are reported on the edges of the images.

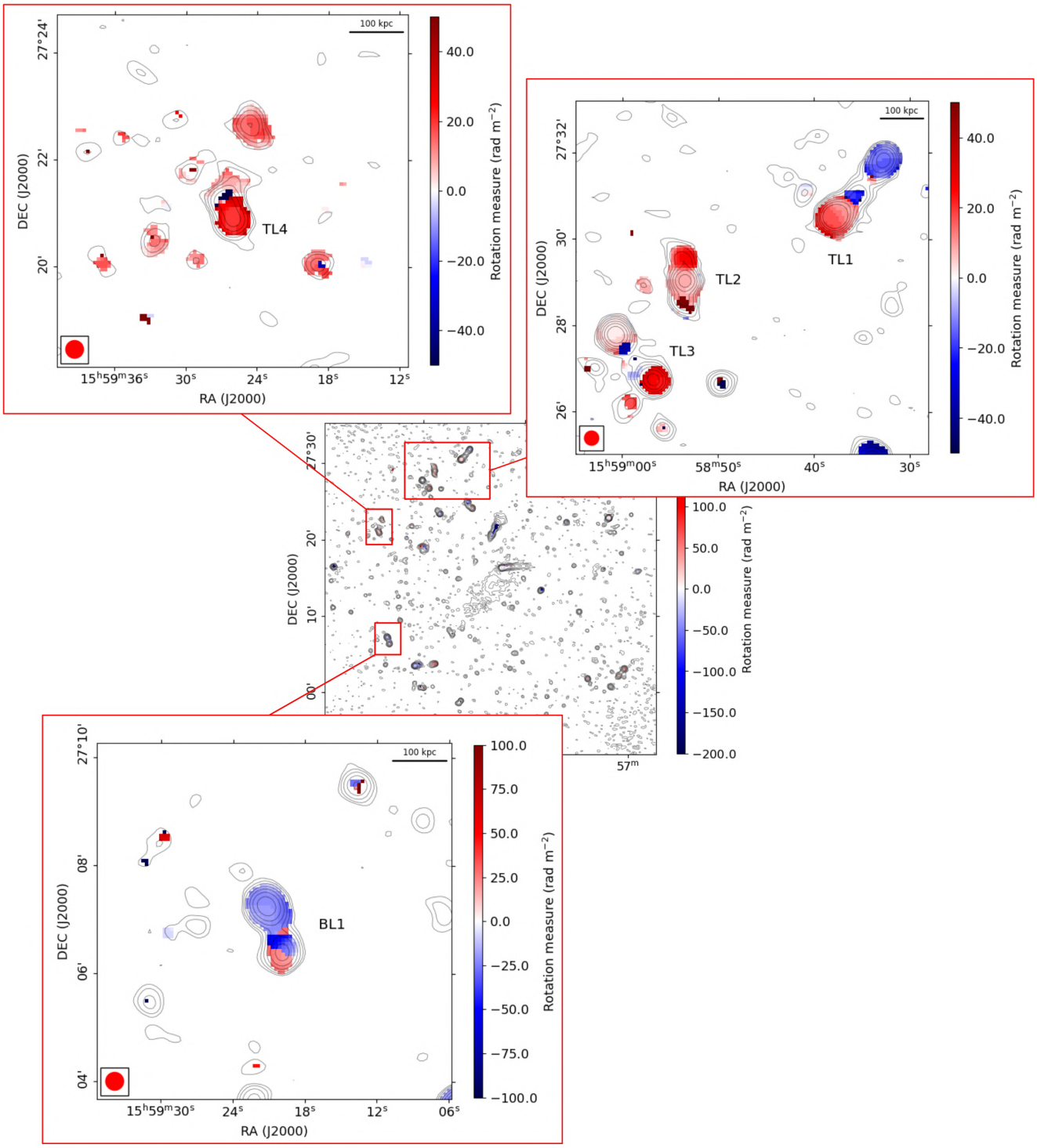

Figure 4.11: Zoom of the RM map (Fig. 4.7) in correspondence of some sources analysed in this work. *Top-left panel:* TL4. *Top-right panel:* TL1, TL2 and TL3. *Bottom-left panel:* BL1. Positive values refer to the magnetic field orientation along the LOS towards the observer, whereas negative values refer to an orientation away from the observer. The range of values shown in the panels may change from the principal map for a better visualisation of their distribution. Spatial scales and resolution beam of $20'' \times 20''$ are reported on the edges of the images.

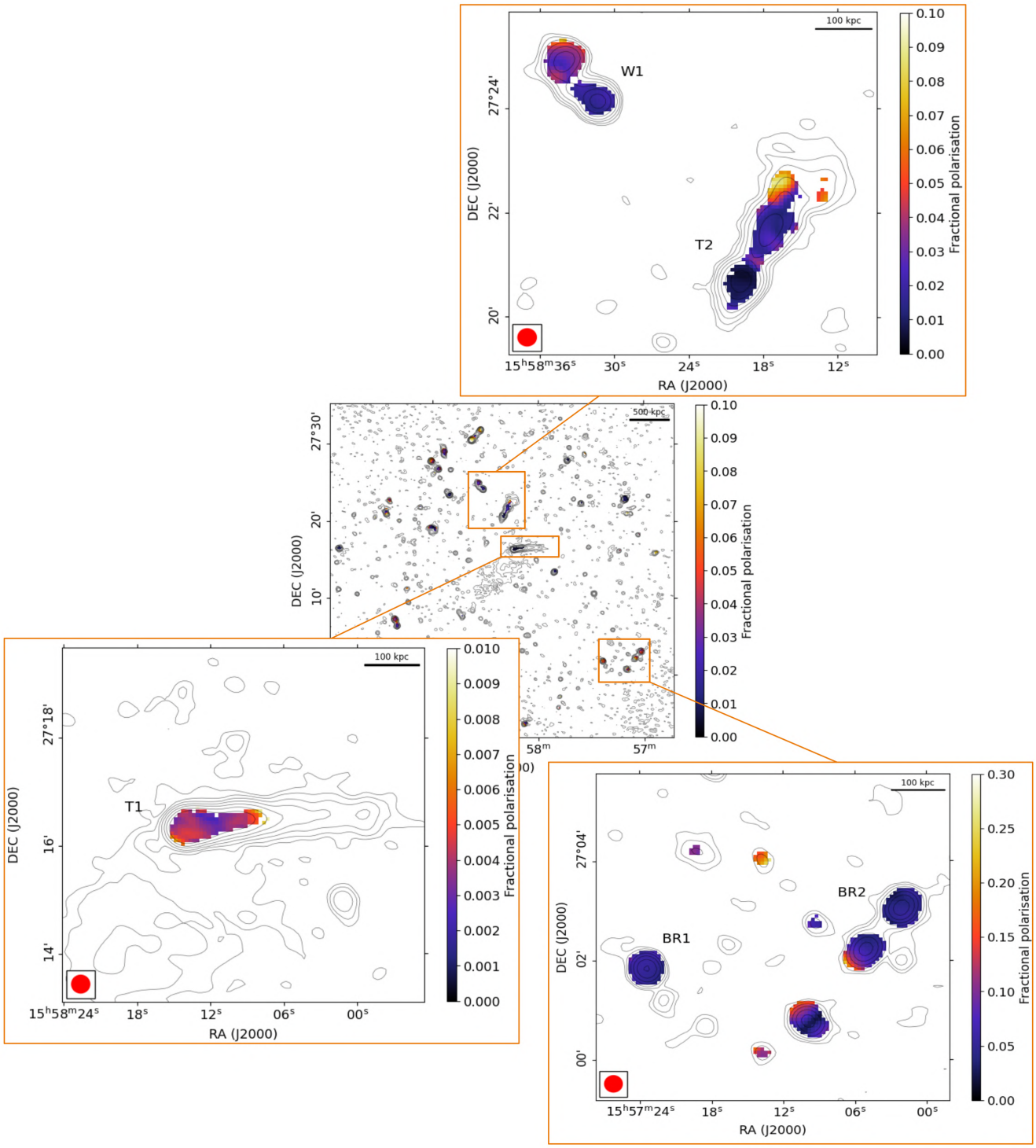

Figure 4.12: Zoom of the fractional polarisation map (Fig. 4.8) in correspondence of some sources analysed in this work. *Top-right panel:* T2 and W1. *Bottom-left panel:* T1. *Bottom-right panel:* BR1 and BR2. The range of values shown in the panels may change from the principal map for a better visualisation of their distribution. Spatial scales and resolution beam of $20'' \times 20''$ are reported on the edges of the images.

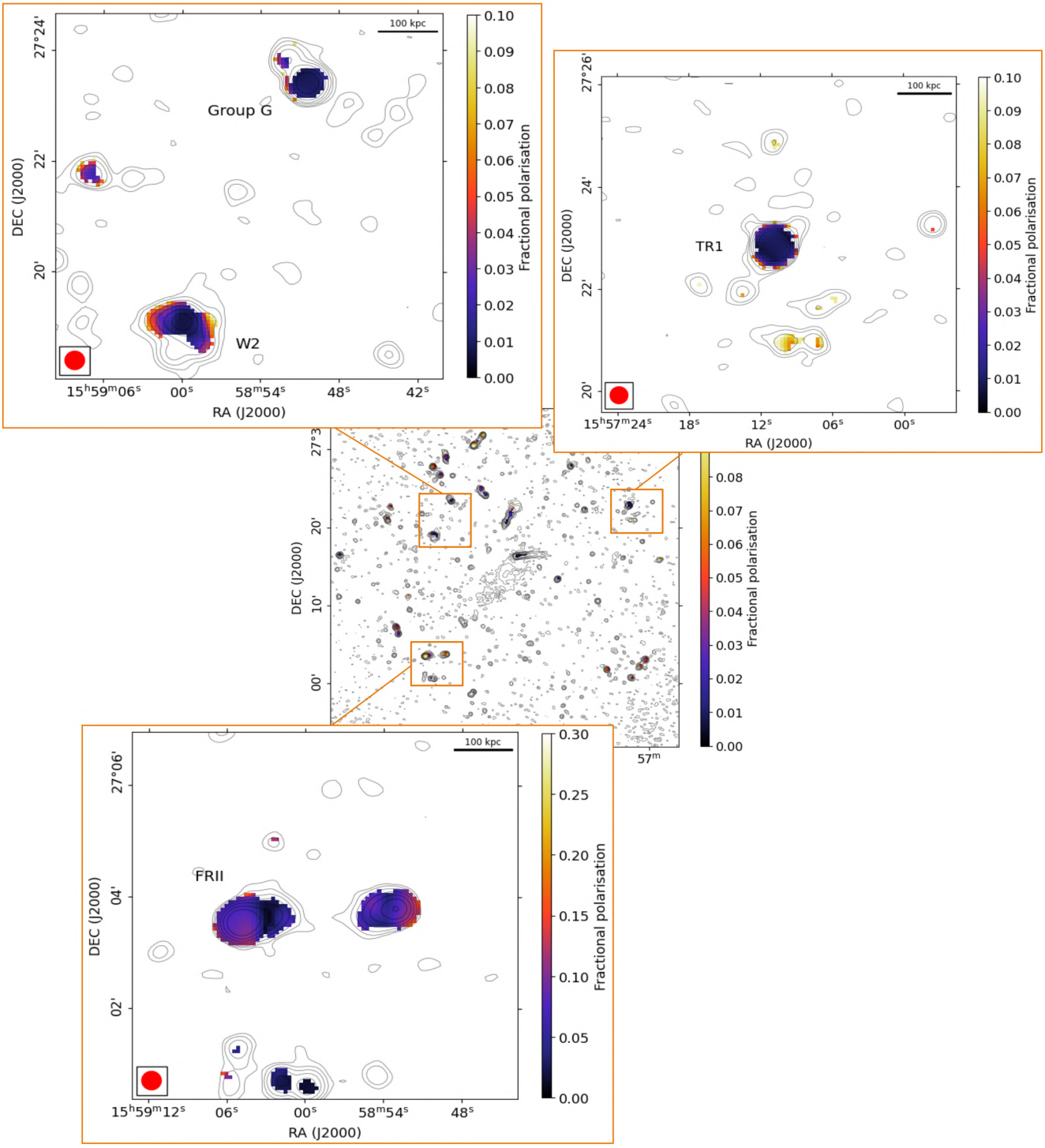

Figure 4.13: Zoom of the fractional polarisation map (Fig. 4.8) in correspondence of some sources analysed in this work. *Top-left panel:* W2 and Group G. *Top-right panel:* TR1. *Bottom-left panel:* FRII. The range of values shown in the panels may change from the principal map for a better visualisation of their distribution. Spatial scales and resolution beam of $20'' \times 20''$ are reported on the edges of the images.

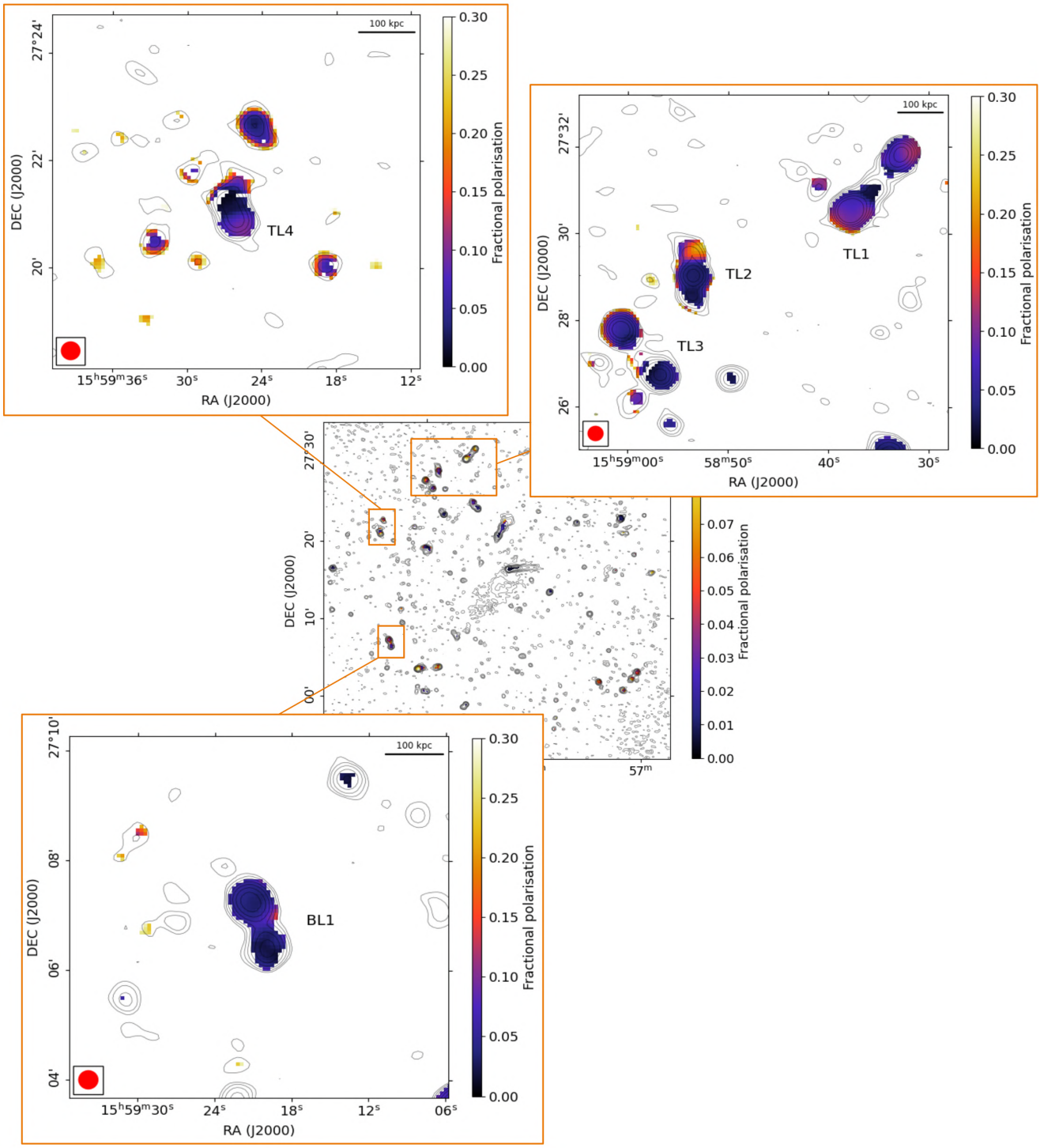

Figure 4.14: Zoom of the fractional polarisation map (Fig. 4.8) in correspondence of some sources analysed in this work. *Top-left panel:* TL4. *Top-right panel:* TL1, TL2 and TL3. *Bottom-left panel:* BL1. The range of values shown in the panels may change from the principal map for a better visualisation of their distribution. Spatial scales and resolution beam of $20'' \times 20''$ are reported on the edges of the images.

Finally, we show in Fig. 4.15 a color-composite image of A2142, combining the optical emission from the SDSS with the Stokes I intensity at 1283 MHz and the linearly polarised emission coming from the radio galaxies.

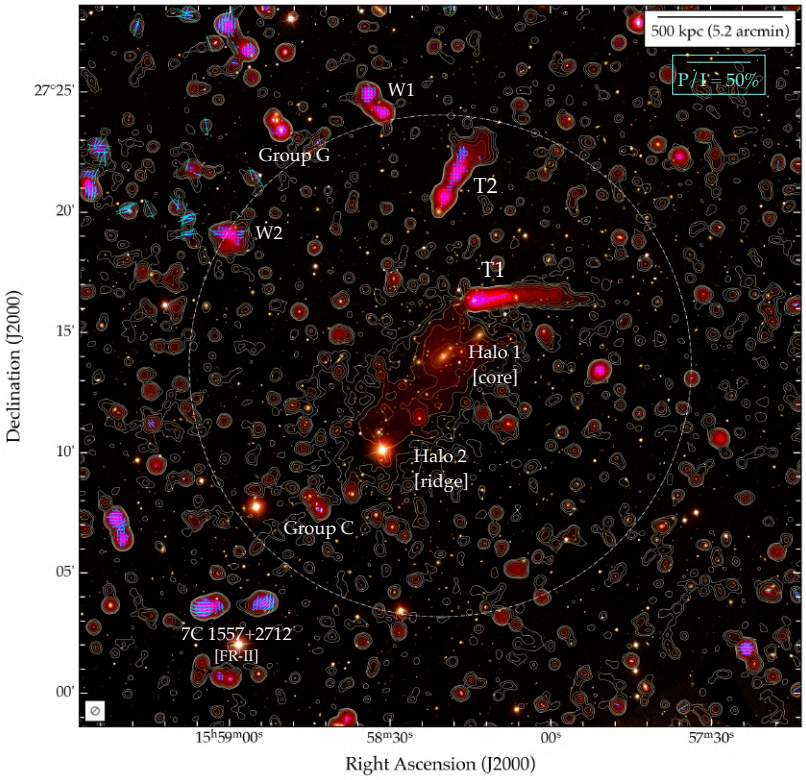

Figure 4.15: Color-composite image of A2142. Optical RGB (SDSS) with overlaid radio contours (1283 MHz), from $3\sigma_{\rm I}$ and scaling by a factor of 2. Red shade traces the Stokes I total intensity, with blue shade tracing the linearly polarised intensity, and the cyan blue vectors (with polarisation angle computed as in eq. 2.19). They represent the magnetic field projected orientation, with extent scaling depending on the fractional polarisation percentage. The known sources and the two halo components are labelled with names given by Venturi et al., 2017 and Bruno et al., 2023. Dashed circle corresponds to the reference distance of 1 Mpc from the cluster center. Spatial scales and resolution beam of $20'' \times 20''$ are reported on the edges of the image.

4.4.1 Radial Profiles

To give the very first considerations on the magnetic field distribution in A2142, we have studied the the average RM, $\langle \mathrm{RM} \rangle$, RM dispersion, $\sigma_{\rm RM}$, and fractional polarisation, $\mathrm{F_p}$, variation as a function of the projected distance from the cluster center.

In Tab. 4.4 we summarise the properties of the sources for this analysis. The known sources are labelled as in Fig. 4.15, while for the unknown ones we have chosen an identification name according to the quadrant of the image in which they are located, e.g. *bottom-left* (BL), *top-right* (TR), *bottom-right* (BR) and *top-left* (TL). The radial distance of each source is computed as the projected distance between the X-ray peak and the brightest polarised pixel detected at the source position, following Stuardi

et al., 2021. The errors in $\langle \mathrm{RM} \rangle$ and in σ_{RM} are calculated as

$$\mathrm{err}_{\langle \mathrm{RM} \rangle} = \frac{\sigma_{\mathrm{RM}}}{\sqrt{n_{\mathrm{beam}}}}, \quad \mathrm{err}_{\sigma_{\mathrm{RM}}} = \frac{\sigma_{\mathrm{RM}}}{\sqrt{2n_{\mathrm{beam}}}}, \tag{4.10}$$

where n_{beam} is the number of beams on which the RM is computed. Only sources with $n_{\mathrm{beam}} \geq 3$ have been considered statistically significant for the analysis. The errors in $\mathrm{F_p}$ are defined based on the propagation of the errors as

$$\mathrm{err}_{\mathrm{F_p}} = \mathrm{F_p} \sqrt{\left(\frac{\sigma_{\mathrm{P}}}{\mathrm{P}}\right)^2 + \left(\frac{\sigma_{\mathrm{I}}}{\mathrm{I}}\right)^2}, \tag{4.11}$$

where $\sigma_{\mathrm{P}} = \sigma_{\mathrm{QU}}$.

Source	Distance [kpc]	$\mathrm{n_{beam}}$	$\langle \mathrm{RM} \rangle \pm \mathrm{err}_{\langle \mathrm{RM} \rangle}$ [rad m^{-2}]	$\sigma_{\mathrm{RM}} \pm \mathrm{err}_{\sigma_{\mathrm{RM}}}$ [rad m^{-2}]	$\mathrm{F_p} \pm \mathrm{err}_{\mathrm{F_p}}$ [$\times 10^{-2}$]
(1)	(2)	(3)	(4)	(5)	(6)
T1	279.31	5	-16.6 ± 80.4	189.9 ± 56.8	0.45 ± 0.08
T2	600.77	10	-84.3 ± 39.4	127.8 ± 28.4	2.62 ± 0.21
W1	1046.68	6	-19.7 ± 13.9	34.7 ± 9.8	2.76 ± 0.36
W2	989.65	6	9.8 ± 43.3	110.1 ± 30.6	5.13 ± 0.87
Group G	1150.19	3	-16.6 ± 12.8	23.6 ± 9.1	5.15 ± 1.75
FR II	1437.59	11	-12.1 ± 25.7	88.9 ± 18.2	7.14 ± 1.14
BL 1	1503.94	7	-15.1 ± 7.8	21.3 ± 5.5	4.53 ± 0.73
TR 1	1789.07	5	6.6 ± 20.1	45.2 ± 14.2	3.68 ± 1.18
BR 1	1760.69	3	16.3 ± 2.4	4.1 ± 1.7	5.41 ± 1.95
BR 2	2067.57	7	20.8 ± 3.1	8.2 ± 2.2	6.00 ± 1.02
TL 1	1699.23	11	-2.0 ± 16.5	56.3 ± 11.7	8.22 ± 1.40
TL 2	1665.54	7	18.6 ± 9.7	26.9 ± 6.9	8.60 ± 1.55
TL 3	1643.40	9	6.8 ± 6.5	19.6 ± 4.6	7.66 ± 1.30
TL 4	1600.49	5	8.0 ± 17.7	40.4 ± 12.5	8.37 ± 2.09

Table 4.4: RM and polarisation properties of the sources detected in polarisation. 1: identification name of the source as show in Fig. 4.15; for the unknown sources, the name is associated to one of the four quadrants of the image in which they are located (BL: *bottom-left*; TR: *top-right*; BR: *bottom-right*; TL: *top-left*). 2: projected distance of the source from the cluster center. 3: number of beams of the source. 4: average RM of the source with associated error. 5: RM dispersion of the source with associated error. 6: fractional polarisation of the source with associated error.

Fig. 4.16 shows the radial profile of $\langle RM \rangle$ for both the cluster radio sources and the radio galaxies in the background of the cluster. By eye, it is possible to notice that the modulus of the average RM, $|\langle RM \rangle|$, decreases as a function of the projected distance from the center, suggesting that the magnetic field becomes less intense toward larger distances. Only T1 presents lower values than expected and this could suggest that the source is located in the peripheral regions of the cluster, but seen in projection in the core. Moreover, there could be local contribution by the source itself. As discussed in Sec. 4.3, T1 shows two peaks around $\phi = 0$ rad m^{-2} in the clean Faraday spectrum (see Fig. 4.6a), suggesting that both the ICM and the radio galaxy are acting as Faraday-rotating media. However, we are not able to resolve them due to our instrumental sensitivity and only one of the two peaks is considered once creating the RM map.

Since the RM can assume positive and negative values, according to the orientation of the magnetic field along the LOS, the $\langle RM \rangle$ can be zero even in presence of a non-zero magnetic field. Consequently, the dispersion of the RM is a better proxy of the magnetic field strength. We show in Fig. 4.17 the radial trend of σ_{RM}, going from $100s$ rad m^{-2} in the central regions to $10s$ rad m^{-2} in the periphery, where the lower values of W1 and Group G could be possibly due to fluctuations in the magnetic field spectrum (Sec. 5.1).

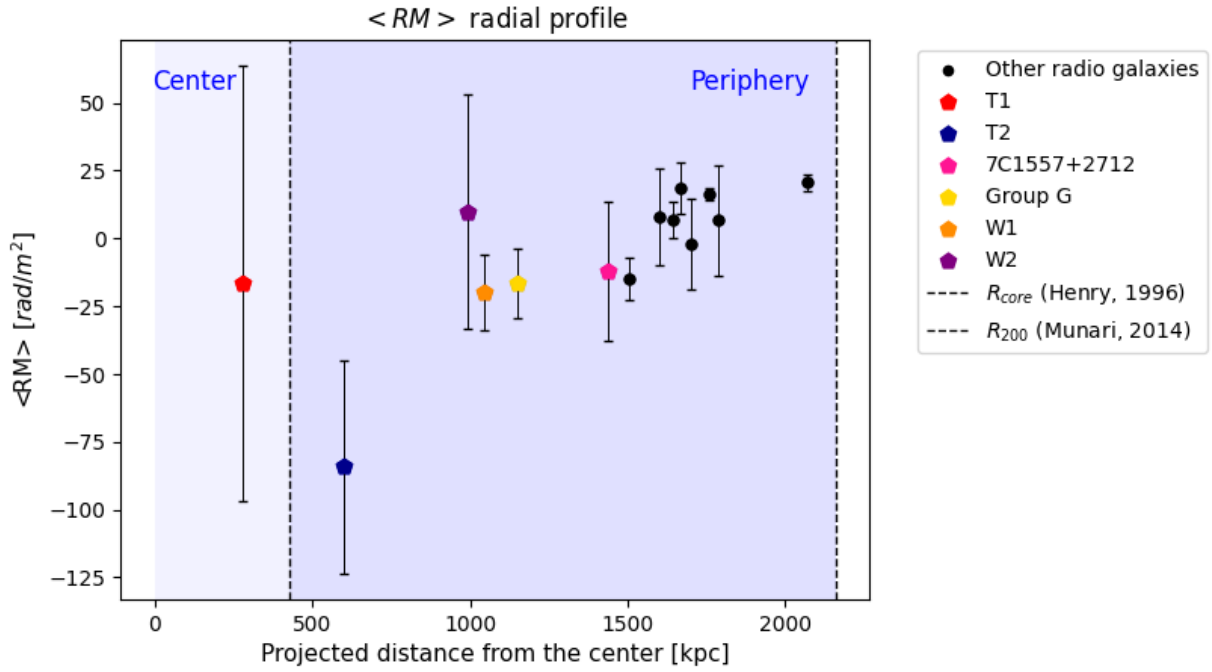

Figure 4.16: $\langle RM \rangle$ as a function of the projected distance from the cluster center. The known sources are represented with the colored pentagons, whereas the other radio galaxies with the *black* dots. The errors are computed following eq. 4.10. Reference distances, such as $R_{core} = 425.60 \pm 20.03$ kpc (Henry & Briel, 1996) and $R_{200} = 2.16 \pm 0.08$ Mpc (Munari et al., 2014), are reported with the dashed lines to discriminate the central from the peripheral regions of the cluster.

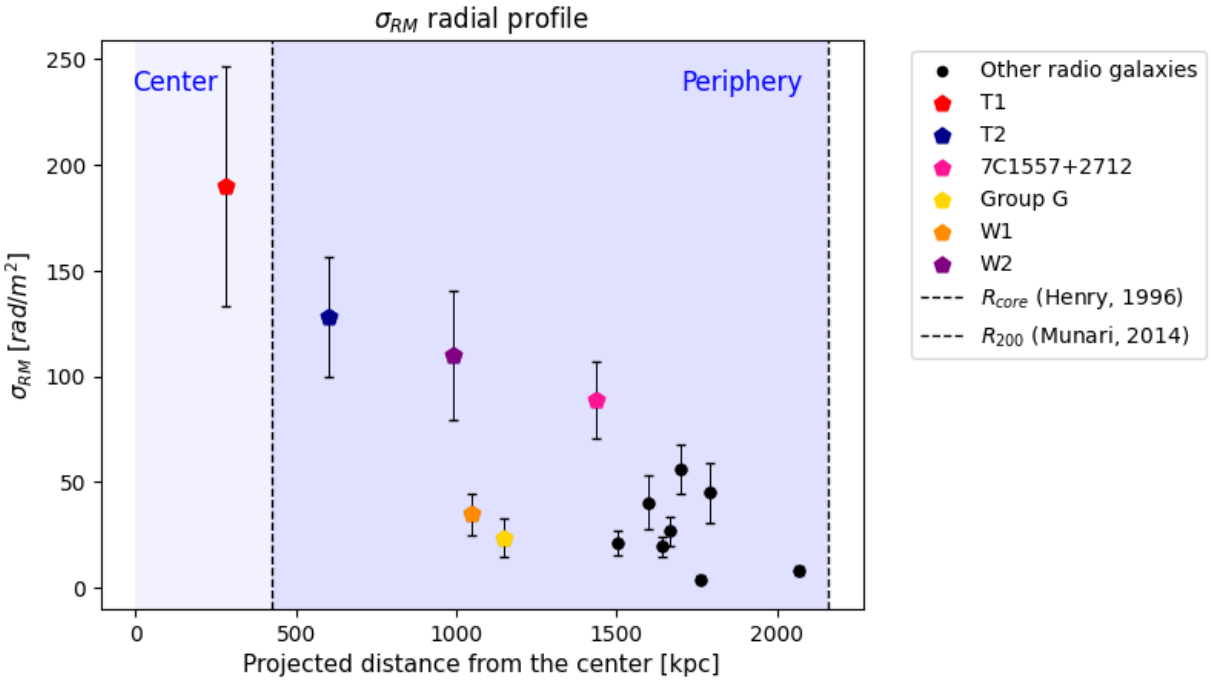

Figure 4.17: $\sigma_{\rm RM}$ as a function of the projected distance from the cluster center. The known sources are represented with the colored pentagons, whereas the other radio galaxies with the *black* dots. The errors are computed following eq. 4.10. Reference distances, such as $\rm R_{core} = 425.60 \pm 20.03$ kpc (Henry & Briel, 1996) and $\rm R_{200} = 2.16 \pm 0.08$ Mpc (Munari et al., 2014), are reported with the dashed lines to discriminate the central from the peripheral regions of the cluster.

Finally, the fractional polarisation radial profile (Fig. 4.18) confirms that radio galaxies seen in projection near the cluster center suffer higher depolarisation than peripheral ones, where the magnetic field is expected to become less intense and producing lower values of the RM dispersion (e.g. Osinga et al., 2022). Also in this case T1 is showing very low values of $\rm F_p$ that can be explained by the additional internal Faraday depolarisation.

According to eq. 2.46 and eq. 2.47, the observed enhancement of $\langle \rm RM \rangle$ and $\sigma_{\rm RM}$ in the inner parts of the cluster is explained not only by the higher expected values of the LOS magnetic field intensity, but also by the gas number density, that is observed to be greater in the core. Thus, an additional check has been performed by using the X-ray surface brightness map[9] as a proxy of the gas number density distribution. It has been regridded using the `imregrid CASA` task, in order to match the pixel scale of the observations, and then masked according to the RM map. The values are reported in Tab. 4.5. Fig. 4.19 shows that the profile is not radially symmetric and confirms that $\sigma_{\rm RM}$ becomes shallower in the external regions, where the medium is expected to be more diluted.

[9] the XMM Cluster Outskirts Project (X-COP) X-ray surface brightness map in the $[0.7 - 1.2]$ keV range previously used by Riseley et al., 2024.

In conclusion, the results obtained so far are in line with similar studies on other clusters (e.g. Bonafede et al., 2010, 2013; Vacca et al., 2012; Stuardi et al., 2021).

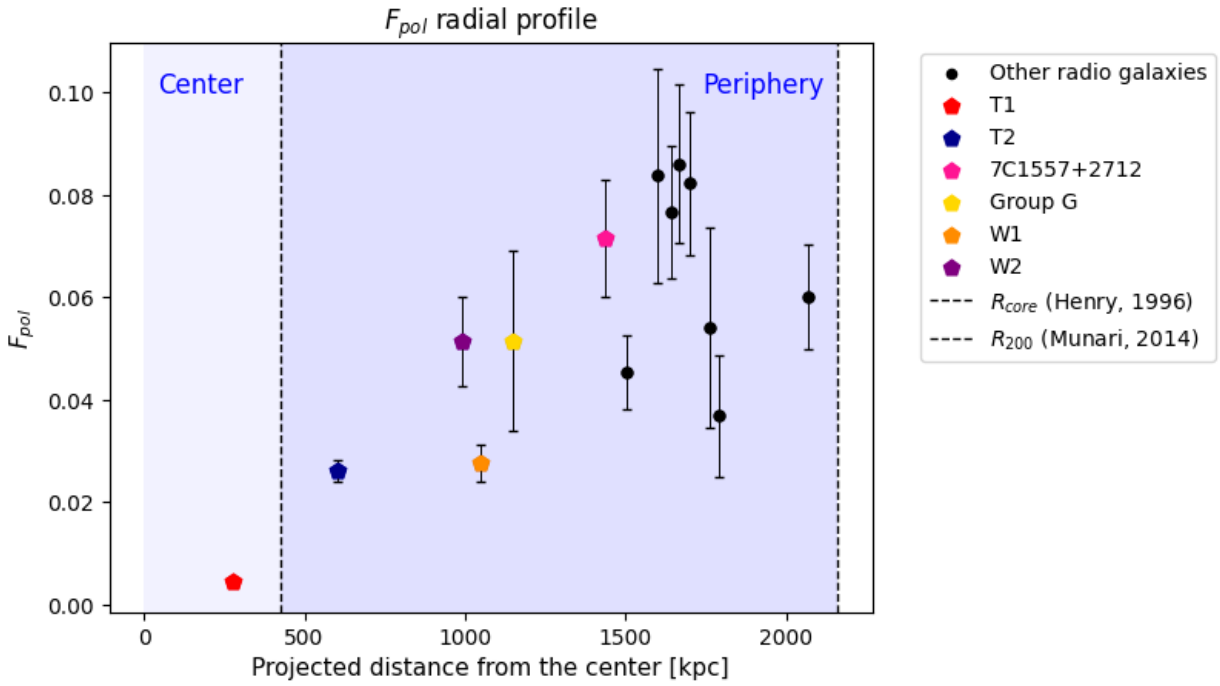

Figure 4.18: F_p as a function of the projected distance from the cluster center. The known sources are represented with the colored pentagons, whereas the other radio galaxies with the *black* dots. The errors are computed following eq. 4.11. Reference distances, such as $R_{core} = 425.60 \pm 20.03$ kpc (Henry & Briel, 1996) and $R_{200} = 2.16 \pm 0.08$ Mpc (Munari et al., 2014), are reported with the dashed lines to discriminate the central from the peripheral regions of the cluster.

Source	S_X	Source	S_X
	[$\times 10^{-5}$ counts s^{-1} arcmin^{-2}]		[$\times 10^{-5}$ counts s^{-1} arcmin^{-2}]
(1)	(2)	(1)	(2)
T1	3.44	TR 1	0.06
T2	0.27	BR 1	0.07
W1	0.15	BR 2	0.06
W2	0.33	TL 1	0.17
Group G	0.56	TL 2	0.38
FR II	0.10	TL 3	0.15
BL 1	0.09	TL 4	0.06

Table 4.5: X-ray surface brightness in correspondence to the source location (2). 1: same as Tab. 4.4.

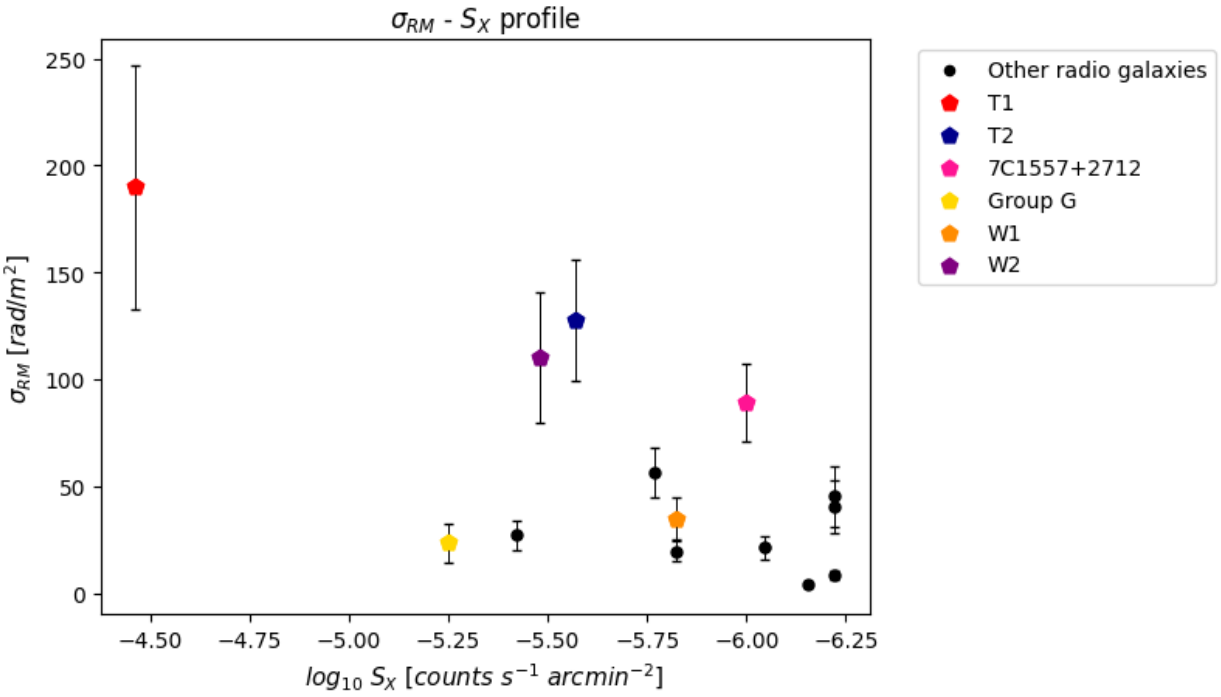

Figure 4.19: σ_{RM} as a function of the X-ray surface brightness in logarithmic scale for a better visualisation (from the highest to the lowest values). The known sources are represented with the colored pentagons, whereas the other radio galaxies with the *black* dots. The errors are computed following eq. 4.10.

Chapter 5

Simulations and Magnetic Field Profile

In this Chapter, we will describe the simulations used in order to constrain the magnetic field properties of A2142. The combinations of parameters to be inserted in the simulations and the adopted 3D magnetic field model are explained in the first section (Sec. 5.1). These simulations are used to create the mock RM maps. In Sec. 5.2 and 5.3, we have compared the results of the simulations with the observations. Finally, we derive the best-fit parameters of the magnetic field model and constrain the cluster magnetic field profile.

5.1 Magnetic Field Modeling: MIRO' Code

Both radio observations (e.g. Murgia et al., 2004; Bonafede et al., 2010) and MHD simulations (e.g. Vazza et al., 2018; Domínguez-Fernández et al., 2019) suggest that, to recreate a realistic cluster magnetic field model, it is necessary to consider components fluctuating over a wide range of spatial scales. Moreover, the classical $\beta-$model (eq. 1.8) is not always sufficient to describe the X-ray surface brightness profile, thus the gas density distribution of galaxy clusters. To accomplish this, we used the modified version of the `MIRO'` code (Bonafede et al., 2013; Stuardi et al., 2021), on A2142. Briefly, the code is designed to start by creating 3D magnetic field and gas density models and to produce 2D RM maps according to eq. 2.23.

We proceed now with a more detailed description of the algorithm step by step:

- first, it creates a 3D gas density model based on the universal electron density profile recently determined by Ghirardini et al., 2019. The authors have exploited X-ray observations of 12 XCOP galaxy clusters (including A2142) and fitted their de-projected density profiles with the functional form from Vikhlinin et al., 2006,

in order to parameterise the radial behavior

$$n_e^2(x) = n_0^2 \frac{(x/r_c)^{-\alpha}}{(1+x^2/r_c^2)^{3\beta-\alpha/2}} \frac{1}{(1+x^\gamma/r_s^\gamma)^{\epsilon/\gamma}}, \tag{5.1}$$

where $x = R/R_{500}$ and $\gamma = 3$. In this way, the code takes in input R_{500} and the dynamical state of the cluster (for A2142: NCC) to set the best-fit parameters of the profile. The specific values are $\log(n_0) = -0.49$, $\log(r_c) = -2.7$, $\alpha = 0.70$, $\beta = 0.39$, $\log(r_s) = -0.51$ and $\epsilon = 2.60$. This model is able to reproduce the observed radial steepening from the core out to two decades in radius ($2R_{500}$);

- secondly, it generates a 3D magnetic field model from the analytical power spectrum derived by Domínguez-Fernández et al., 2019, which represents a much more realistic magnetic field energy distribution expected in galaxy clusters with respect to the Kolmogorov power-law spectrum, $\propto k^{-n}$ (e.g. Murgia et al., 2004; Bonafede et al., 2010). Using cosmological MHD simulations, the authors found that the 1D magnetic spectra of all the analysed galaxy clusters can be well fitted to

$$E_B(k) \propto k^{3/2} \left[1 - \mathrm{erf}\left(B \, \ln \frac{k}{C} \right) \right], \tag{5.2}$$

where $k = \sqrt{\sum_i k_i^2}$ (with $i = 1, 2, 3$) is the wavenumber corresponding to the physical scale of the magnetic field fluctuations (e.g. $\Lambda \propto 1/k$), B is a parameter related to the width of the spectrum and C is the wavenumber corresponding to the peak of the spectrum. Both B and C depend on the dynamical state of the cluster, are the best-fit values derived from the simulated clusters analysed in Domínguez-Fernández et al., 2019 and are taken in input by the code.

In order to set up a turbulent magnetic field with the power spectrum as eq. 5.2, the algorithm starts with the vector potential, $\tilde{\mathbf{A}}(\mathbf{k})$, and selects the corresponding power spectrum in the Fourier space, $E_A(k) \propto k^{-2} E_B(k)$ (Murgia et al., 2004). Random values of the amplitude, $A_{k,i}$, and the phase, ϕ, are then defined for each point in the Fourier domain in order to obtain a Gaussian distribution for the real magnetic field components: $A_{k,i}$ is randomly drawn from the Rayleigh distribution, while ϕ is uniformly distributed in the range $[0, 2\pi]$. The magnetic field components in the Fourier space are then $\tilde{\mathbf{B}}(\mathbf{k}) = i\mathbf{k} \times \tilde{\mathbf{A}}(\mathbf{k})$ and are transformed back to the real space using a 3D Fast Fourier transform. The magnetic field generated in this way is by definition divergence-free, with Gaussian components, B_i, having $\langle B_i \rangle = 0$ and $\sigma_{B_i}^2 = \langle B_i^2 \rangle$. The radial profile of the magnitude of the magnetic field is expected to scale with the thermal electron density as

$$|\mathbf{B}(r)| \propto n_e(r)^\eta, \tag{5.3}$$

where η is assumed to be equal to 0.5 (Bonafede et al., 2010). The normalisation of the magnetic field distribution is finally obtained imposing that the magnetic field averaged over the cluster volume is B_{norm} and will be determined during the comparison with the observations;

- in the end, the code produces a 2D RM map, integrating numerically the obtained thermal electron density and magnetic field profiles along the z axis of the cube, starting from the center of the cluster.

Overall, the magnetic field model depends on six parameters: the radial slope, η, the minimum and maximum spatial scales of the fluctuations, Λ_{min} and Λ_{max}, the normalisation, B_{norm}, and the B and C parameters of the magnetic field spectrum.

The simulation takes in input the size of the simulated box and the cell resolution. In order to match the observations, we have chosen a pixel scale of 3.4 kpc (i.e. 2″ at the cluster redshift) and to produce a 829^3 pixels cube to reach a cluster dimension of $\sim 2.8^3$ Mpc^3 (i.e. out to R_{500} from the cluster center). The maximum fluctuating scale of the magnetic field components in Fourier space, k_{max}, is defined as $k_{max} = (829 \cdot 0.5) - 1 \sim 413$, therefore fixing

$$\Lambda_{min} = \frac{829 \cdot 3.4}{k_{max}} \sim 7 \text{ kpc}. \tag{5.4}$$

Regarding the power spectrum, B and C are respectively assumed to be 1.118 and 5.026 Mpc^{-1} (corresponding to a power spectrum peaking at ~ 199 kpc). This is justified by the observations in the radio and X-ray band discussed in Ch. 3: A2142 is not currently undergoing a major merger, but is seen at least $1-2$ Gyr after the first event and has possibly experienced several minor mergers from weak-lensing studies. Thus, we have assumed $z_{last} = 0.1$, which corresponds to a post-merger dynamical state (see ID E1 in Tab. 1 of Domínguez-Fernández et al., 2019).

We summarise the fixed parameters of the simulations in the following table.

Size of the box	829 pxl	Dynamical state[1]	NCC
Resolution	3.4 kpc	R_{500}[2]	1409 kpc
Λ_{min}	7 kpc	B	1.118
η	0.5	C	5.026 Mpc^{-1}

Table 5.1: List of fixed parameters adopted for the simulations.

[1] for the Ghirardini et al., 2019 density profile.
[2] Planck Collaboration et al., 2016.

The final outputs of the simulations are mainly 4: three cubes with the three components of the magnetic field model (B_x, B_y and B_z) and a cube with the projected volume weighted mean density, mean magnetic field and RM for each pixel (Fig. 5.1), with size of $\sim 2.8^2$ Mpc^2 and a resolution of 3.4 kpc.

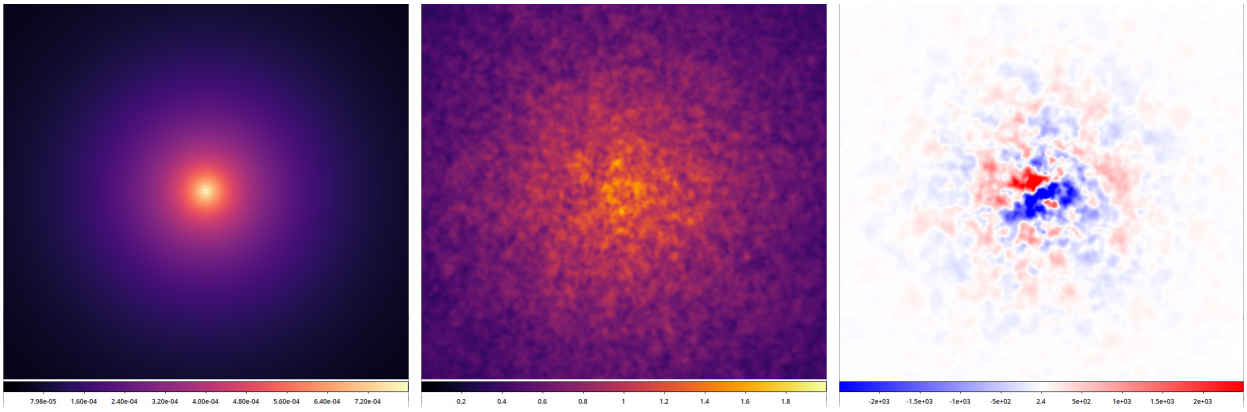

(a) **(b)** **(c)**

Figure 5.1: Example of final output of MIRO' code, with $B_{norm} = 1.5$ μG and $\Lambda_{max} = 940$ kpc. *Panel (a):* 2D map of the projected mean density in cm^{-3}; *Panel (b):* 2D map of the projected mean magnetic field in μG. *Panel (c):* 2D RM map in rad m^{-2}.

5.2 Comparison with the Observations and Profiles

Since six free parameters cannot be constrained with the number of sources we have, we have decided to fix $\eta = 0.5$, as found by Bonafede et al., 2010, and $\Lambda_{min} = 7$ kpc. We have also chosen B and C as reported in Tab. 5.1, which refer to a post-merger dynamical state of the cluster according to Domínguez-Fernández et al., 2019 results.

Our magnetic field model considers a total of two free parameters, Λ_{max} and B_{norm}, that can be investigated through the comparison with our observations. We have chosen the sets of parameters, $\Lambda_{max} = [50, 470, 940]$ kpc and $B_{norm} = [0.7, 1.0, 1.5, 3.0]$ μG, and, for every combination, we have performed 5 simulations from different random seeds, as different realisations of the same model will correspond to different values of the RM at a given position. The 2D RM maps are then convolved with a Gaussian function with the same FWHM as the restoring beam of the observations (i.e. 33.4 kpc) and rebinned following the imaging procedure (see Sec. 4.2.6).

The first approach we adopted for the comparison consists in the extraction of the RM dispersion, $\sigma_{\rm RM}$, from annuli of increasing radius from the center of the map. We have chosen to compare only $\sigma_{\rm RM}$, because the RM can assume both positive and negative values according to the orientation of the magnetic field along the LOS and consequently the average RM can be zero, even for a strong magnetic field. Thus, $\sigma_{\rm RM}$ is a more robust proxy of the magnetic field strength and, in general, this is the approach used in literature (e.g. Bonafede et al., 2013; Govoni et al., 2017; Stuardi et al., 2021).

Then, the $\sigma_{\rm RM}$ radial profiles are realised by taking the mean in each annulus over the 5 simulations and plot it together with the associated scatter (computed as the standard deviation) and the observed values of the sources. In addition, we have performed a further check by analysing $\sigma_{\rm RM}$ as a function of the X-ray surface brightness, S_X.

Examples of the mean radial profiles of $\sigma_{\rm RM}$ and the $\sigma_{\rm RM} - S_X$ mean profiles are reported together, for different magnetic field models, in Fig. 5.3 and Fig. 5.4, respectively. As it is possible to observe, the change of B_{norm} is responsible for the variation of the overall normalisation of the profiles, thus the higher B_{norm}, the higher are the values of $\sigma_{\rm RM}$ at fixed Λ_{max}. On the other hand, at fixed B_{norm}, higher values of Λ_{max} give higher $\sigma_{\rm RM}$, since we are integrating components with different fluctuating scales along the same LOS. It is clear that none of the profiles perfectly fits the observed values, suggesting that our model it is too simplistic for the scenario we are analysing, and possibly other power spectra should be considered.

As specified in Sec. 4.3, T1 presents a Faraday-complex spectrum (Fig. 4.6a), possibly related to the local emission to the radio galaxy, that we are not able to resolve. This can explain the lower values of $\sigma_{\rm RM}$ for such source with respect to the mean simulated one. The opposite case involves W2, the radio galaxy seen in projection behind the 'Galactic bubble' (see Fig. 4.4). By performing a deeper analysis in the FDF spectrum of W2 (Fig. 5.2), we found evidences of multiple components, but not a real double peak as in T1. There is a possible contribution from the 'Galactic bubble', increasing $\sigma_{\rm RM}$ for W2. In general, the values are very difficult to be fitted since we have multiple contribution from both the 'Galactic bubble' or locally from the source and future observations require a higher resolution in Faraday space to disentangle the two components. Moreover, we are missing sources located in the very central regions of the cluster ($\lesssim 250$ kpc), that could help in finding the best-fit profile.

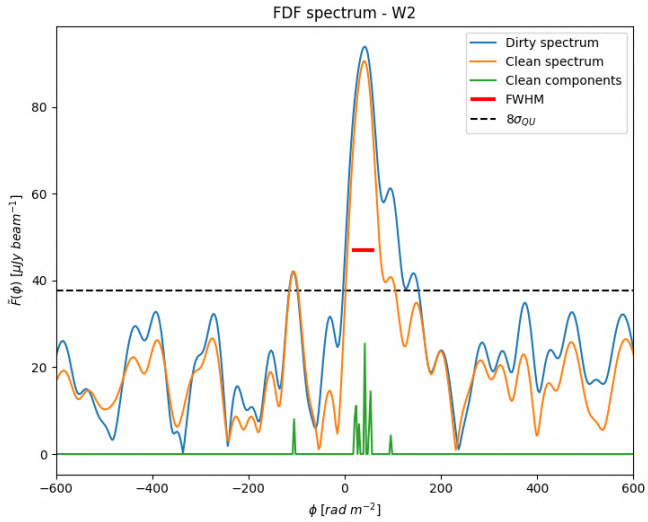

Figure 5.2: Reconstructed FDF spectrum taken from one pixel of W2. The dirty spectrum is shown in *blue*, the clean spectrum in *orange* and the clean components in *green*. The FWHM of the RMTF is reported in *red* and the $8\sigma_{\rm QU}$ with the *black* dashed line as a reference.

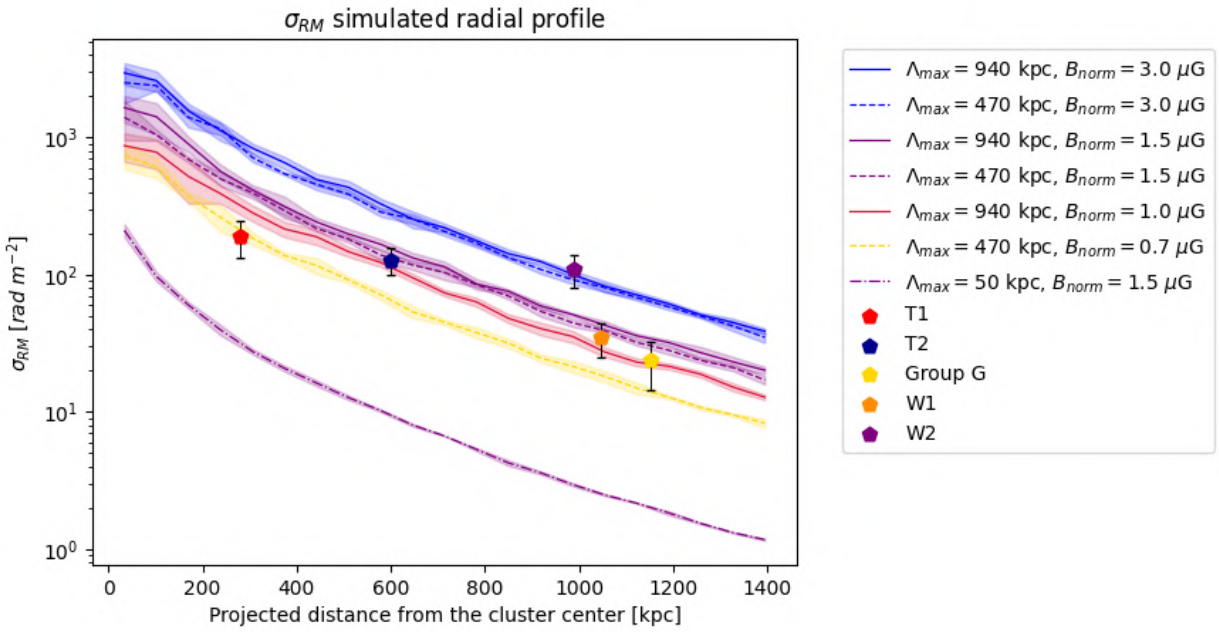

Figure 5.3: Simulated profile of $\sigma_{\rm RM}$ as a function of the projected distance from the cluster center. The profile is computed as the mean over 5 simulations and the scatter is the standard deviation. Different colors refer to different values of the magnetic field normalisation, B_{norm}. From higher to lower: *blue* (3.0 μG), *purple* (1.5 μG), *bordeaux* (1.0 μG) and *yellow* (0.7 μG). Different line-styles represent different maximum fluctuating scales, Λ_{max}, of the magnetic field. From higher to lower: *solid* (940 kpc), *dashed* (470 kpc) and *dashdot* (50 kpc). Observed values with associated errors of 5 sources within R_{500} are reported as in Fig. 4.17. The y axis is in logarithmic scale for a better visualisation of the profile.

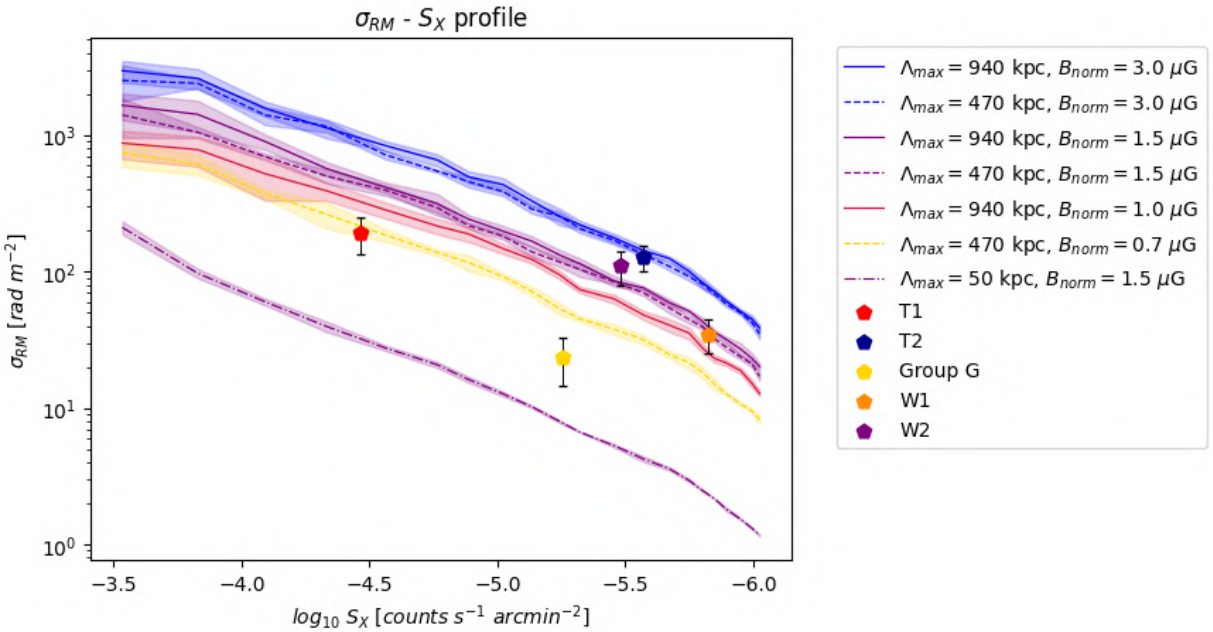

Figure 5.4: Simulated profile of $\sigma_{\rm RM}$ as a function of the X-ray surface brightness in logarithmic scale. The profile is computed as the mean over 5 simulations and the scatter is the standard deviation. Colors and line-styles follow the ones in Fig. 5.3. Observed values with associated errors of 5 sources within R_{500} are reported as in Fig. 4.17. The y axis is in logarithmic scale for a better visualisation of the profile.

5.3 Constraining the Magnetic Field Properties

To better compare the observed and simulated quantities, we have trimmed the observed RM map at 414 pixels according to the dimension of the simulated RM maps and use it as a mask. In this way, the 5 simulated RM maps for each magnetic field model are blanked following the shape of the sources and the correspondent $\sigma_{\rm RM}$ is then extracted. We have repeated this method for all the combinations of parameters considered in the previous section, and calculated the *reduced* χ^2 for $\sigma_{\rm RM}$ using the formula from Govoni et al., 2006

$$\chi^2_{\sigma_{\rm RM},red} = \frac{1}{d.o.f.} \sum_{i=1}^{5} \frac{(\sigma_{{\rm RM}obs,i} - |\sigma_{\rm RM}|_{sim,i})^2}{|{\rm Scatter}_{sim,i}|^2 + {\rm Err}^2_{\sigma_{\rm RM}obs,i}}, \tag{5.5}$$

where $d.o.f. = 3$ are the degrees of freedom of the model, i.e. the number of data points (5) subtracted by the number of free parameters (2). $\sigma_{{\rm RM}obs,i}$ is the observed RM dispersion of every source, here 5, and ${\rm Err}_{\sigma_{\rm RM}obs,i}$ is the correspondent error calculated as eq. 4.10. $|\sigma_{\rm RM}|_{sim,i}$ is the mean over 5 simulations of the RM dispersion extracted from that specific source. In the end, $|{\rm Scatter}_{sim,i}|$ is the mean of the scatter of 5 simulations in the annulus in which the source is located.

Λ_{max}	B_{norm}	$\langle B_0 \rangle \pm {\rm err}_{B_0}$	$\chi^2_{red,\sigma_{\rm RM}}$
[kpc]	[μG]	[μG]	
(1)	(2)	(3)	(4)
50	3.0	13.9 ± 0.7	16.76
470	3.0	16.4 ± 6.7	6.03
940	3.0	12.9 ± 4.3	5.34
50	1.5	7.2 ± 0.3	18.91
470	**1.5**	$\mathbf{8.9 \pm 3.2}$	**4.85**
940	1.5	7.3 ± 1.1	5.06
50	1.0	5.0 ± 0.5	19.68
470	1.0	5.0 ± 2.1	7.58
940	1.0	4.7 ± 1.9	7.41
50	0.7	3.4 ± 0.2	20.11
470	0.7	3.6 ± 1.6	11.54
940	0.7	4.9 ± 1.8	11.75

Table 5.2: List of the outcomes of the statistical analysis for the combination of parameters, Λ_{max} and B_{norm}. The row in boldface refers to the minimum. 1: maximum spatial scale of the magnetic field fluctuations. 2: normalisation of the magnetic field power spectrum. 3: mean central magnetic field with associated error. 4: reduced χ^2 for the RM dispersion.

The aim is to find what combination of parameters minimise the reduced χ^2 value.

We report the results in Tab. 5.2 and in Fig. 5.5, where it is possible to notice that the minimum of the reduced χ^2 is reached for $\Lambda_{max} = 470$ kpc and $B_{norm} = 1.5$ μG, with mean central magnetic field, $\langle B_0 \rangle$, of 8.9 $\pm$ 3.2 μG (i.e. within $\sim$ 70 kpc from the cluster center). The best-fit radial profile for $\sigma_{\rm RM}$ is shown in Fig. 5.6. The correspondent magnetic field radial profile (Fig. 5.7) has been computed as the mean over the 5 simulations and the scatter is again the standard deviation. Each profile has been obtained by creating a new cube, having the same dimension of the other magnetic field components cubes, with the magnetic field module, $|B| = \sqrt{3}B_x$, in each pixel. Then, the average magnetic field module is extracted from spherical shells with increasing radius from the center. $\langle B_0 \rangle$ of every combination of parameters refers to the mean over 5 simulations in the first spherical shell (i.e. up to $\sim$ 70 kpc) and err_{B_0} is computed as the standard deviation. By removing W2 from the statistical analysis we have noticed an improvement in the reduced χ^2 value (declining to 2.38), as expected for the reasoning mentioned above, but the minimum does not change. We show in Fig. 5.8 the best-fit radial profile of the average RM for $\Lambda_{max} = 470$ kpc and $B_{norm} = 1.5$ μG, which confirms the good agreement of the simulations outcomes with the observed values of the sources.

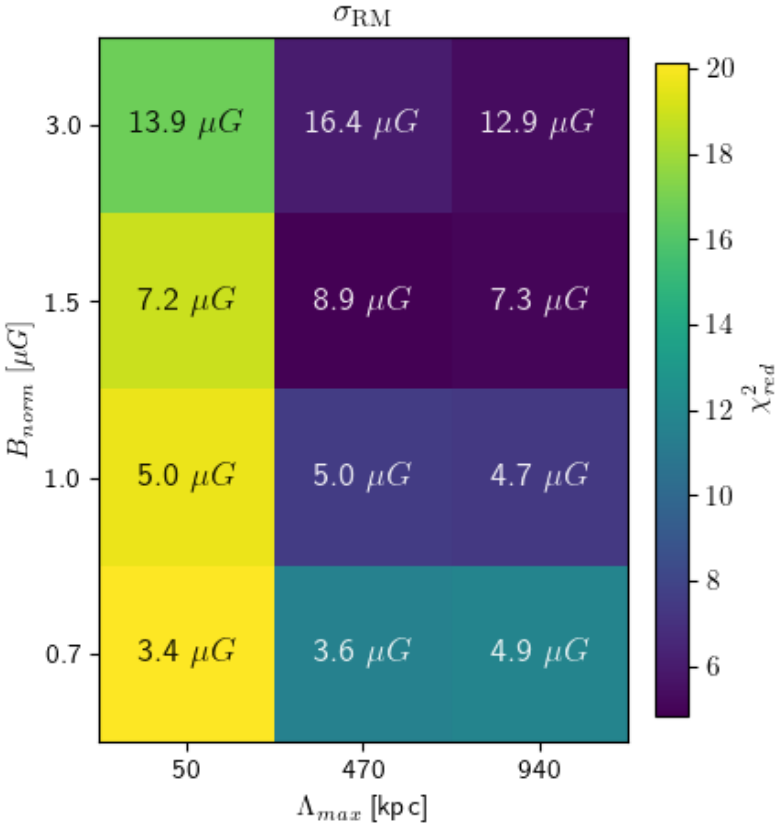

Figure 5.5: Reduced χ^2 value of $\sigma_{\rm RM}$ for each combination of B_{norm} and Λ_{max}. The correspondent average central value of the magnetic field, $\langle B_0 \rangle$, is reported at the center of each square. The minimum is 4.85 with $\langle B_0 \rangle = 8.9$ μG.

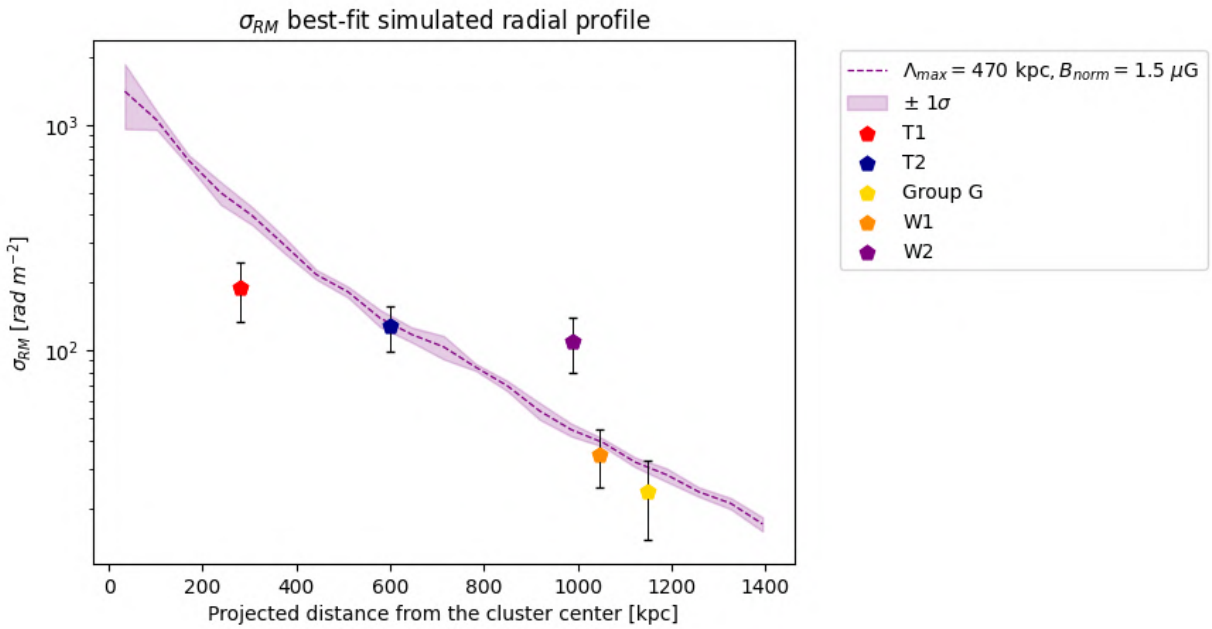

Figure 5.6: Best-fit simulated profile of $\sigma_{\rm RM}$ as a function of the projected distance from the cluster center, for Λ_{max} and $B_{norm} = 1.5$ μG. The profile is computed as the mean over 5 simulations and the scatter is the standard deviation. Observed values with associated errors of 5 sources within R_{500} are reported as in Fig. 4.17. The y axis is in logarithmic scale for a better visualisation of the profile.

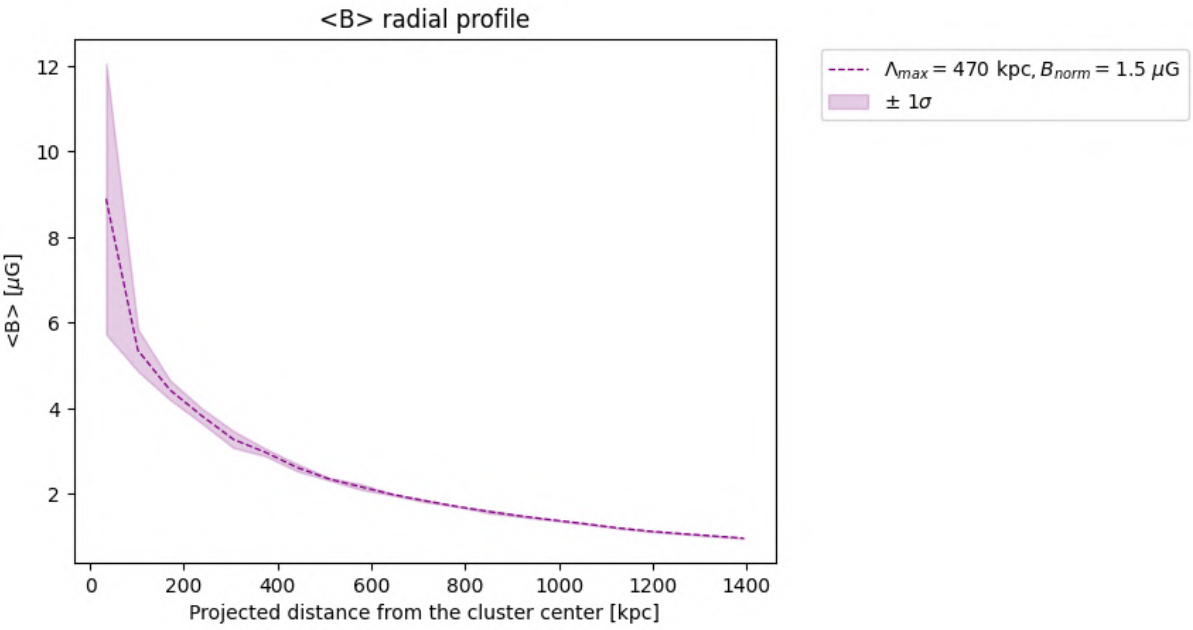

Figure 5.7: Profile of $\langle B \rangle$ as a function of the projected distance from the cluster center, for $\Lambda_{max} = 470$ kpc and $B_{norm} = 1.5$ μG. The profile is computed as the mean over 5 simulations and the scatter is the standard deviation. The central average magnetic field, $\langle B_0 \rangle$, is equal to 8.9 ± 3.2 μG.

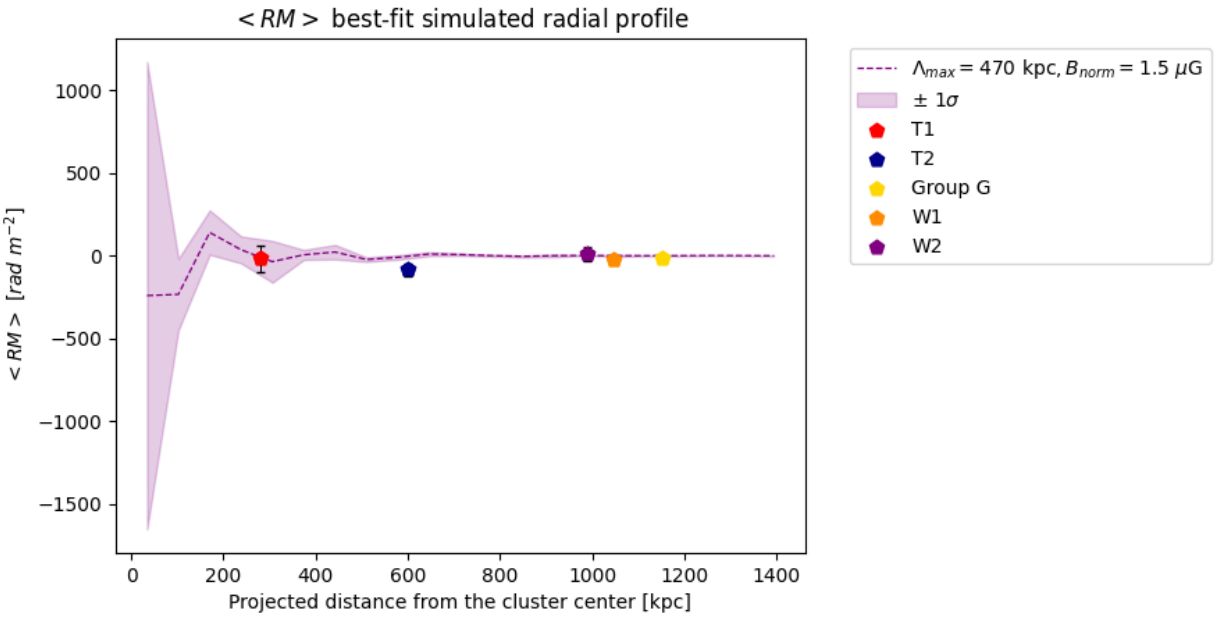

Figure 5.8: Best-fit simulated profile of ⟨RM⟩ as a function of the projected distance from the cluster center, for $\Lambda_{max} = 470$ kpc and $B_{norm} = 1.5$ μG. The profile is computed as the mean over 5 simulations and the scatter is the standard deviation. Observed values with associated errors of 5 sources within R_{500} are reported as in Fig. 4.16.

The average magnetic field in 1 Mpc^3 volume, $\langle B_{1\mathrm{Mpc}^3} \rangle$, is ~ 2.6 μG. It has been computed from the magnetic field module cube, within a sphere with radius of 620 kpc, i.e. $V = 4\pi r^3/3 \sim 1$ Mpc^3, and by taking the mean over 5 simulations. The average magnetic field within 1.2 Mpc is ~ 1.6 μG and is higher than the magnetic field equipartition estimate of ~ 0.19 μG, that has been derived with eq. 2.43 and using the parameters for the radio halo H3 from Tab. 2 of Riseley et al., 2024. In particular, $\xi(\alpha, \nu_1, \nu_2) = 1.31 \times 10^{-13}$, $z = 0.0894$, $\alpha = 1.68$, $d = 2400$ kpc and $I_0 = 0.2$ μJy arcsec^{-2}. This extremely low value of the equipartition magnetic field is incompatible with the values derived from our earlier analysis, suggesting that the assumption of equipartition cannot be made in the case of A2142.

To summarise, we found that a magnetic field tangled on scales between 7 and 470 kpc, following a power spectrum with a peak at $\sim$ 199 kpc, best describes our data with a mean central magnetic field of 8.9 $\pm$ 3.2 μG and $\eta = 0.5$.

Our work assumed a thermal electron density profile as eq. 5.1, which departs with respect to the classical β or double-β models, and is one of the few studies that uses a magnetic field power spectrum as eq. 5.2. It has been previously adopted to constrain the magnetic field profile and intensity in merging clusters (Stuardi et al., 2021; De Rubeis et al., 2024), whereas the very first works using this approach assumed a power-law spectrum with different indexes (e.g. Murgia et al., 2004; Govoni et al., 2006, 2017; Bonafede et al., 2010; Vacca et al., 2010, 2012). In general, the intensity

and profile of the magnetic field in A2142 is in agreement with the results found in the literature. This can be explained by the model considered and by the dynamical state of the cluster and its interaction with the environment. The magnetic field strength is assumed to decrease as the square root of the thermal electron density (eq. 5.3) and we allow the maximum fluctuating spatial scale, Λ_{max}, i.e. k_{min}, to change, but not the minimum one, Λ_{min}, i.e. k_{max}, for a consistent comparison with the observations. Moreover, the peak of the magnetic field spectrum (that is defined by the parameter C) is fixed, assuming a post-merger dynamical state. The uncertainty lies on the redshift of the last merging event, so by testing other post-merger systems studied by Domínguez-Fernández et al., 2019, we expect that the equipartition is reached at larger spatial scales. This can produce the same mock RM maps from a less intense magnetic field. Therefore, testing and fixing the majority of the parameters allow to break the possible degenerancies.

Finally, A2142 is considered as an intermediate category between a CC and a NCC cluster and presents evidences of minor mergers during its evolution, which may contribute to the magnetic field amplification and can explain the high magnetic field intensity found in the central regions of this cluster. We note that the value derived in this work is not extreme, as Vacca et al., 2012 have found a magnetic field strength of 11.7 μG in the center of A2199 CC cluster.

5.3.1 Magnetic Field and Origin of the Diffuse Radio Emission

The hadronic or leptonic origin of the clusters radio sources is a widely-debated field and many authors have investigated the connection between thermal and non-thermal components for radio mini-halos (e.g. Bravi et al., 2016; Giacintucci et al., 2019). Recently, Ignesti et al., 2020 have performed this study in a sample of radio mini-halos found in relaxed clusters and used their radio/X-ray correlations to constrain the physical parameters of an hadronic model. They have assumed stationary conditions, without including the effect of the re-acceleration, and found a super-linear $I_{\rm R}/I_{\rm X}$ correlation. This suggests a peaked distribution of relativistic electrons and a magnetic field intensity in the range of 10–40 μG for $\eta = 0.5$. The value found for the average central magnetic field in our work is lower with respect to this result, but could be explained again by the complex dynamical state of A2142. H1, shows, in fact, a sub-linear correlation (Bruno et al., 2023; Riseley et al., 2024), that suggests a broader distribution of the electrons, that could be re-accelerated by the merger events occurring during A142 evolution. However, this scenario should not be ruled out, as the average magnetic field intensity of 4.9 μG within 200 kpc (computed in the same way as above) satisfies the lower limit discussed by Bruno et al., 2023 and presented in Ch. 3, that is consistent to a potential hadronic origin of the radio mini-halo, H1, in A2142.

Chapter 6

Conclusions and Future Perspectives

The aim of this work was to study and constrain the magnetic field intensity and profile in A2142. This galaxy cluster is peculiar from its dynamical point of view, as it shows evidences of a past intermediate-mass-ratio merger and minor mergers, and is considered as a warm-cool-core cluster. This intermediate object represents an additional case for understanding the magnetic field amplification level in such systems and it was the first time that data in polarisation of the SKA precursor MeerKAT interferometer have been used with this specific purpose.

For this thesis, we have used high-sensitivity pre-reduced MeerKAT L-band (872-1712 MHz) data, that have been imaged in polarisation joining the two measurement sets and dividing the full-bandwidth in 256 channels (then 191) for the further analysis. After convolving the images to a common resolution of $20'' \times 20''$, we have created the Stokes Q and U cubes and applied the RM synthesis technique. This advanced method allows to reduce the instrumental bandwidth depolarisation and to recover the emission at multiple Faraday depths along a particular LOS. By inspecting the outcomes, we have noticed a bubble-like structure in polarised intensity seen in projection in the top-left region of Fig. 4.4, which has no diffuse Stokes I counterpart. It could be associated to a galactic filament, that we called 'Galactic bubble'. Moreover, the radio galaxy T1 shows a clear double peak in polarisation (Fig. 4.6a), that we are not able to resolve for instrumental reasoning, and could be originated from a Faraday-rotating and synchrotron-emitting medium local to the source.

To give the very first considerations on the magnetic field distribution in A2142, we have created the RM and the fractional polarisation maps from the RM synthesis outputs by masking for 6 times the noise in polarised intensity and 3 times the noise in Stokes I intensity and corrected them for the Galactic Faraday rotation and for the Ricean bias, respectively. We have then extracted and studied the average RM, $\langle \mathrm{RM} \rangle$, RM dispersion, σ_{RM}, and fractional polarisation, $\mathrm{F_p}$, for the sources in Tab. 4.4 as a function of the projected distance from the cluster center.

In general, the RM map (Fig. 4.7) displays gradients of values and the appearance results particularly patchy in correspondence to the resolved radio galaxies and becomes more uniform for the unresolved ones, due to magnetic field fluctuations on different scales. Regarding the fractional polarisation map (Fig. 4.8), the values increase towards the edges of the cluster, whereas the central radio galaxies show the lowest fractions for the high RM dispersion, and, in case of T1, also for the internal Faraday depolarisation. From the $\langle \mathrm{RM} \rangle$ radial profile (Fig. 4.16) we conclude that $|\langle \mathrm{RM} \rangle|$ decreases as a function of the projected distance from the cluster center, suggesting that the magnetic field becomes less intense toward larger distances. Only T1 presents lower values than expected, possibly explained by its position in the cluster or by the local contribution of the source. We show in Fig. 4.17 the radial trend of σ_{RM} from $100s$ rad m^{-2} in the central regions to $10s$ rad m^{-2} in the periphery (also confirmed by the comparison with the X-ray surface brightness as a proxy of the gas number density; Fig. 4.19), where the lower values of W1 and Group G could be possibly due to fluctuations in the magnetic field spectrum. Finally, the fractional polarisation radial profile confirms that radio galaxies seen in projection near the cluster center suffer higher depolarisation than peripheral ones (Fig. 4.18). In general, the outcomes obtained so far are in line with the results of other studies in this field (e.g. Bonafede et al., 2010, 2013; Vacca et al., 2012; Stuardi et al., 2021).

Starting from these results, we ran 3D simulations using a modified version of the `MIRO'` code (Bonafede et al., 2013; Stuardi et al., 2021) in order to produce mock RM maps. We assumed a 3D gas density model following the electron density profile for NCC clusters found by Ghirardini et al., 2019 and a 3D magnetic field model from the power spectrum for post-merger clusters (ID E1) derived by Domínguez-Fernández et al., 2019. Of the six parameters available, we have fixed four of them (η, Λ_{min}, B and C) and left the other two to vary in a defined range of values, namely $\Lambda_{max} = [50, 470, 940]$ kpc and $B_{norm} = [0.7, 1.0, 1.5, 3.0]$ μG. The resolution of the simulations is 3.4 kpc in order to match the observations and to reach a cluster dimension out to R_{500} from the cluster center. We have compared the simulated outcomes with the observational results using two different approaches and computed the reduced χ^2 of σ_{RM} according to eq. 5.5 in order to find the best-fit parameters of the magnetic field model and to define the cluster magnetic field profile generating the observed RM. We found that a magnetic field tangled on scales between 7 and 470 kpc, following a power spectrum with a peak at $\sim$ 199 kpc, best describes our data with a mean central magnetic field of 8.9 ± 3.2 μG and $\eta = 0.5$. The average magnetic field in 1 Mpc^3 volume, $\langle B_{1\mathrm{Mpc}^3} \rangle$, is ~ 2.6 μG, whereas the one within 1.2 Mpc (~ 1.6 μG) is higher with respect to the equipartition estimate (~ 0.19 μG).

None of the simulated mean radial profiles perfectly fits the observed values (Fig. 5.3), suggesting that our model is too simplistic. In particular, there are two radio galaxies, T1 and W2, showing evidences of additional contribution, respectively locally to the source and from the 'Galactic bubble'. By removing W2 from the statistical analysis, the reduced χ^2 is improved as expected as mentioned in Sec. 5.3. Future observations with a greater instrumental resolution would allow to minimise the beam depolarisation and to detect higher polarised signal, especially from the sources in the very central regions of the cluster, whereas larger observational bandwidth would improve the FWHM of the RMTF, thus resolving the narrow multiple peaks from components on the same LOS. Regarding the magnetic field model, we have left free to vary only two parameters, B_{norm} and Λ_{max}. Future work could be focused on the exploration of intermediate spatial scales between 470 and 50 kpc and between 470 and 940 kpc, with the same normalisations tested above or higher/lower values, as different combinations may produce the same RM. Further tests could be carry out on the dynamical state of the cluster, e.g. considering the PM ($z_{last} = 0.2$) power spectrum by Domínguez-Fernández et al., 2019, peaking at ~ 224 kpc, or on exploring other peaks of the magnetic field power spectrum, or on the index η. In the latter case, higher values of the parameter lead to a higher central magnetic field and to a stronger radial decrease of the magnetic field energy density. In the end, the average central magnetic field intensity does not allow us to discard an hadronic origin of the radio mini-halo, H1, in A2142.

Appendix A

Radio Interferometry

Radio astronomy covers six decades in frequency across the electromagnetic spectrum from MHz to THz frequencies, thus requires a wide range of radio telescopes and observing techniques to accomplish different scientific aims.

There are two kind of radio telescopes, the *single-dish* and the *interferometer*. The *single-dish* is composed by a parabolic mirror and a sub-reflector, that collect and focus the radio waves in phase onto a feed antenna, and by receivers, which detect, filter and amplify the signal. Moreover, a device called *orthomode transducer* (OMT) is provided to combine and/or to separate orthogonal polarisations. The leading property of a receiving antenna is the *effective collecting area*, A_e, that approaches the geometric area, $A_g = \pi D^2/4$, where D is the diameter of the *aperture*, an imaginary circular hole covering the mirror. The variation of the effective area with the orientation, i.e. the angular distribution of the instrumental response, represents the receiving *power pattern* and is called Point Source Response, or PSF, or beam. The beam of most radio telescopes (Fig. A.1) is nearly a Gaussian and the beamwidth is usually specified by the angle between the half-power points,

$$\theta_{\mathrm{HPBW}} \approx 0.89 \, \frac{\lambda}{D}, \tag{A.1}$$

where λ is the observing wavelength. It represents the resolving power of the telescope and is diffraction limited.

Interferometry is a technique that increases the angular resolution by combining N dishes into an array, the *interferometer*, that can assume different configurations. The simplest one is composed by two antennas (Fig. A.2), separated by a baseline vector, $\vec{\mathbf{b}}$, with length b, whose voltage outputs, V_1 and V_2, are correlated, i.e. the *correlator* multiplies the outputs and takes the time average, obtaining the final response

$$R = \langle V_1 V_2 \rangle = \Big(\frac{V^2}{2} \Big) \cos(\omega \tau_g). \tag{A.2}$$

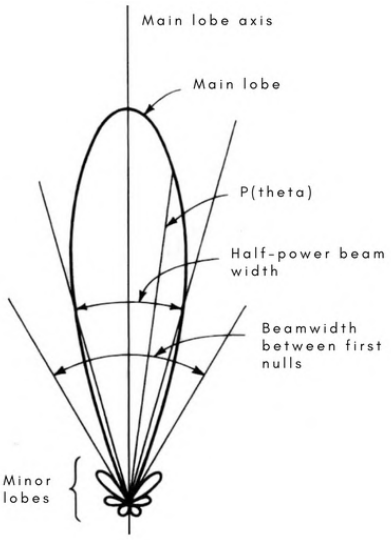

Figure A.1: Power pattern of a receiving antenna, $P(\theta)$. The main lobe represents the central peak between the first nulls, i.e. at $\theta = \pm\lambda/D$, and is the region containing the principal response. The minor lobes are called sidelobes and are separated by nulls in the power pattern, i.e. at $\theta = \pm n\lambda/D$. The Half-Power-BeamWidth ($\theta_{\rm HPBW}$) and the BeamWidth between the First Nulls ($\theta_{\rm BWFN} = 2\lambda/D$) are reported.

It changes sinusoidally with time and is usually called 'interferometer fringes'. The amplitude is proportional to the flux density, S, of the source and to the two effective areas, A_1 and A_2, of the antennas

$$\frac{V^2}{2} \propto S(A_1 A_2)^{1/2}, \tag{A.3}$$

while the phase between the signals, ϕ, is a relative phase and depends on the angular frequency, ω, and on the *geometric delay*[1], τ_g, thus on the observing λ

$$\phi = \omega\tau_g = 2\pi\Big(\frac{b}{\lambda}\Big)\cos(\theta), \tag{A.4}$$

where θ is the angle between the baseline vector, $\vec{\mathbf{b}}$, and the source direction, $\hat{\mathbf{s}}$.

For identical antennas the product between the two voltages is the power pattern of an individual antenna, which goes like $sinc^2$. This means that the PSF of an interferometer, the *dirty beam*, is a cosine modulated by a $sinc^2$

$$P(\theta) \propto sinc^2\Big(\frac{D}{\lambda}\cos(\theta)\Big)\cos\Big(2\pi\frac{b}{\lambda}\cos(\theta)\Big), \tag{A.5}$$

where the main beam of the power pattern defines the FOV of the interferometer, which goes like $\sim \lambda/D$.

To improve the PSF of an interferometer, a larger number of components, i.e.

[1] plane waves from a distant point source must travel an extra distance, $b\cos(\theta)$, in order to reach the antenna 1 with respect to antenna 2 and this causes a lag in time.

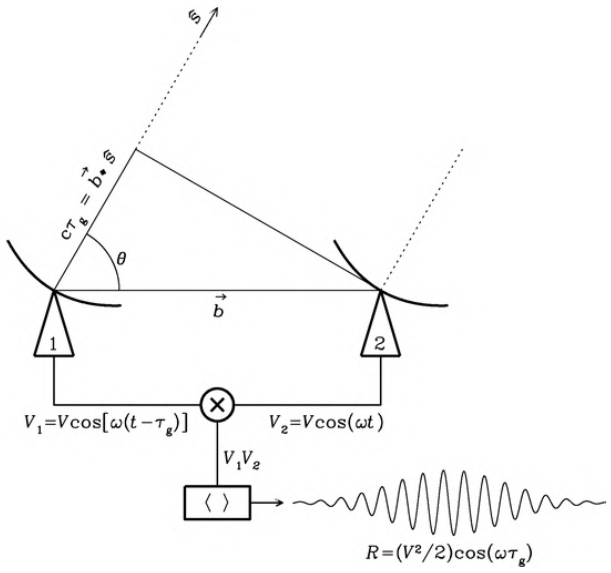

Figure A.2: Simple sketch of a two-element multiplying interferometer. The two antennas, 1 and 2, are separated by the baseline vector, $\vec{\mathbf{b}}$, and θ is the angle between the latter element and the common direction versor, $\hat{\mathbf{s}}$. $c\tau_g$ is the additional path that the radio waves have to travel with respect to antenna 2 in order to reach antenna 1 and is defined as the projection of $\vec{\mathbf{b}}$ on $\hat{\mathbf{s}}$. V_1 and V_2 are the two output voltages that are correlated giving the interferometer response, R (from Condon & Ransom, 2016).

number of baselines, is required. The instantaneous synthetised beam projected onto the plane of the sky of an interferometer with N antennas is the arithmetic mean of the $N(N-1)/2$ individual responses, that rapidly approaches a Gaussian as N increases. Whereas for a single-dish the angular resolution is limited by the projected diameter (eq. A.1), the resolution of a multi-element interferometer depends on the maximum baseline, b_{max}, separating the dishes

$$\theta_{min} \sim \frac{1}{u_{max}}, \; u_{max} = \frac{b_{max}\,\sin(\theta)}{\lambda}, \tag{A.6}$$

that is also called *minimum recoverable angular scale*. The longer baselines have a narrower projected angular fringe spacing, which means that the corresponding responses are sensitive to very compact objects; on the other hand, shorter baselines are sensitive to extended objects because of their larger angular fringe spacing. The largest fringe spacing corresponds to the *maximum recoverable scale*, which is limited by the 'short spacing problem', namely b_{min} has to be larger than the diameter D of the dishes.

There is a natural Cartesian coordinates system for expressing the correlator response of an interferometer and is shown in Fig. A.3: $\hat{\mathbf{s_0}}$ is the direction to the source center (the 'phase center'); the plane perpendicular to $\hat{\mathbf{s_0}}$ is called (u, v) *plane* and its 'coverage' is the distribution of the projected baselines in unit of λ, as seen from the source at infinity; each baseline vector position is specified by the coordinates (u, v, w), where

$w = 0$ on the source direction; finally, the *source plane* is the projection of the celestial sphere onto a plane with a tangent point defined by the phase center and the positions on the sky are defined by the direction cosines, (l, m, n), and are measured with respect to the (u, v) plane.

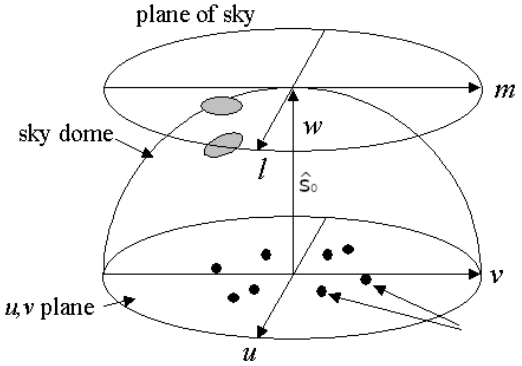

Figure A.3: Simple sketch of the coordinates system. The (u, v) plane is the plane perpendicular to the phase center, $\hat{\mathbf{s_0}}$, where the black dots represent the projected baselines in unit of λ and their position is defined by (u, v, w). The plane of the sky, or source plane, is the plane tangent to the sky dome in the intersection with $\hat{\mathbf{s_0}}$ and the positions of the sources are defined by (l, m, n).

To recover the full power of a source, the 'cosine' correlator output must be combined with the 'sine' correlator output, thus resulting in the *complex correlator*. The response of a complex correlator to any extended source with brightness distribution $I(\hat{\mathbf{s}})$ is called *complex visibility*

$$V = \int\int I(\hat{\mathbf{s}}) \exp(-2\pi i \vec{\mathbf{b}} \cdot \hat{\mathbf{s}}/\lambda) \mathrm{d}\Omega, \tag{A.7}$$

and represents the 2D Fourier transform of the source brightness distribution. It can be re-written as a function of the coordinates mentioned above

$$V(u, v) = \int\int I(l, m) \exp[-2\pi i(ul + vm)] \mathrm{d}l \mathrm{d}m \tag{A.8}$$

and also as a function of amplitude and phase as

$$\begin{aligned} V &= R_C - iR_S = Ae^{-i\phi}, \\ A &= (R_C^2 + R_S^2)^{1/2}, \quad \phi = \tan^{-1}\Big(\frac{R_S}{R_C}\Big), \end{aligned} \tag{A.9}$$

where R_C and R_S are respectively the cosine and the sine correlator responses.

Theoretically, the complex visibility is a continuous function and the sky brightness distribution can be obtained directly by computing the 2D inverse Fourier transform

as

$$I(l,m) = \int\int V(u,v)\exp[2\pi i(ul+vm)]\mathrm{d}u\mathrm{d}v. \tag{A.10}$$

However, the (u,v) coverage depends by definition on the number of antennas in the array and a single baseline samples a discrete point in the (u,v) plane by measuring both the amplitude and the phase of a complex visibility. Therefore, $V(u,v)$ cannot be sampled 'continuously' through all the (u,v) plane and deconvolution is required. The 'sampled' visibility, $V_s(u,v)$, is technically the product between the 'true' visibility, $V_t(u,v)$ (eq. A.7), and the *sampling function*, $S(u,v)$, i.e. the (u,v) coverage,

$$V_t(u,v)\cdot S(u,v) = V_s(u,v), \tag{A.11}$$

and represents the starting point for the image reconstruction (Fig. A.4).

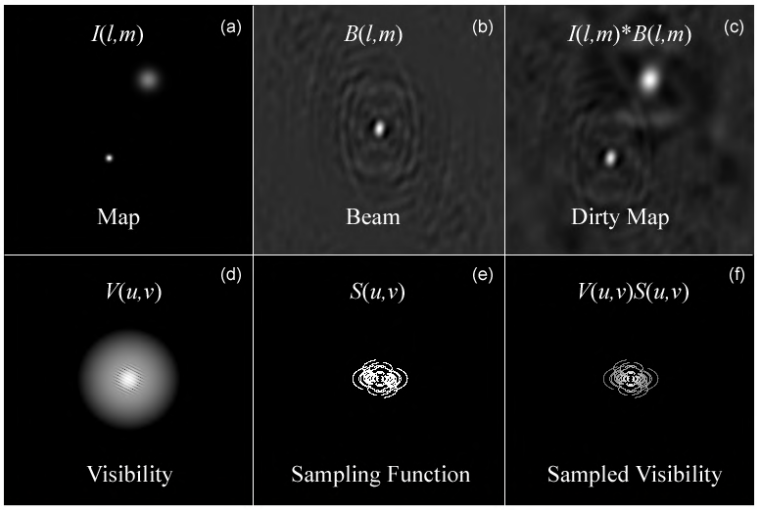

Figure A.4: An example of the sky brightness distribution map (a) and the correspondent visibility (d). The sampling function (e) is represented by the (u,v) coverage and the product between (d) and (e) gives the sampled visibility (f). The inverse Fourier transform of (e) and (f) are respectively the dirty beam (b) and the dirty map (c). The latter one is also expressed as the convolution between (a) and (b).

The inverse Fourier transform of both the sampled visibility and the sampling function are respectively the *dirty map*, $I^D(l,m)$, and the *dirty beam*, $B(l,m)$. According to the convolution theorem,

$$I^D = FT^{-1}(V_s) = FT^{-1}(V_t\cdot S) = FT^{-1}(V_t) * FT^{-1}(S) \tag{A.12}$$

and given that the true visibility is the Fourier transform of the brightness distribution, $I(l,m)$,

$$I^D = I * B.$$

Hence, to obtain the sky brightness distribution map, we have to deconvolve the dirty map for the dirty beam, which means to reduce the sidelobes created by the gaps in the (u, v) coverage.

This cleaning method has been developed firstly by Högbom, 1974 and then implemented in different algorithms (e.g. Clark, 1980; Schwab, 1984), assuming that an extended source is a collection of point-like sources. Here the steps:

- first, it initialises the residuals map, I^R, to the dirty map, I^D, and the clean components, I^C, list to empty values;

- secondly, it identifies the pixels with the peak intensity, I_{max}, in the residuals map and adds them to the clean component list as a fraction of the peak intensity, γI_{max}, where γ is the 'loop gain', usually 0.1-0.3;

- then, it subtracts over the whole dirty map a dirty beam pattern, B, (including the full sidelobes, centered on the position of the peaks saved in the clean component list) convolved with the normalised clean components, I^C,

$$I^R = I^D - \gamma B * I^C. \tag{A.13}$$

  At every cycle, the residuals image becomes the dirty image, until a stopping threshold is reached;

- finally, the algorithm multiplies the clean components by the clean beam, B^I, (an elliptical Gaussian that fits the main lobe of the dirty beam), and adds it back to the residuals map

$$I = I^R + I^C * B^I. \tag{A.14}$$

In this way, the 'cleaned' final image is obtained.

Bibliography

[1] Ackermann M., et al., 2014, The Astrophysical Journal, 787, 18

[2] Ade P. A. R., et al., 2016, Astronomy & Astrophysics, 594, A17

[3] Alexander E. L., 2022, Synchrotron, https://emmaalexander.github.io/resources.html

[4] Allen S. W., Evrard A. E., Mantz A. B., 2011, Annual Review of Astronomy and Astrophysics, 49, 409–470

[5] Arnaud M., 2009, Astronomy & Astrophysics, 500, 103

[6] Arshakian T. G., Beck R., 2011, Monthly Notices of the Royal Astronomical Society, 418, 2336

[7] Bahcall N. A., 1999, in Dekel A., Ostriker J. P., eds, Formation of Structure in the Universe. Cambridge University Press, p. 135

[8] Bartelmann M., 2010, Classical and Quantum Gravity, 27, 233001

[9] Beck R., Krause M., 2005, Astronomische Nachrichten, 326, 414–427

[10] Beck A. M., Hanasz M., Lesch H., Remus R. S., Stasyszyn F. A., 2012, Monthly Notices of the Royal Astronomical Society: Letters, 429, L60

[11] Beck A. M., Dolag K., Lesch H., Kronberg P. P., 2013, Monthly Notices of the Royal Astronomical Society, 435, 3575

[12] Bell M. R., Oppermann N., Crai A., Enßlin T. A., 2013, Astronomy & Astrophysics, 551, L7

[13] Beresnyak A., Miniati F., 2016, The Astrophysical Journal, 817, 127

[14] Bernstein J. P., Bhavsar S. P., 2001, Monthly Notices of the Royal Astronomical Society, 322, 625

[15] Best P. N., von der Linden A., Kauffmann G., Heckman T. M., Kaiser C. R., 2007, Monthly Notices of the Royal Astronomical Society, 379, 894

[16] Birkinshaw M., 1999, Physics Reports, 310, 97–195

[17] Blasi P., Burles S., Olinto A. V., 1999, The Astrophysical Journal, 514, L79

[18] Böhringer H., et al., 2000, The Astrophysical Journal Supplement Series, 129, 435

[19] Bolivar R. R., et al., 2023, NuSTAR Observations of Abell 665 and 2146: Constraints on Non-Thermal Emission (arXiv:2308.00969)

[20] Bonafede A., Giovannini G., Feretti L., Govoni F., Murgia M., 2009, Astronomy & Astrophysics, 494, 429

[21] Bonafede A., Feretti L., Murgia M., Govoni F., Giovannini G., Dallacasa D., Dolag K., Taylor G. B., 2010, Astronomy & Astrophysics, 513, A30

[22] Bonafede A., Dolag K., Stasyszyn F., Murante G., Borgani S., 2011, Monthly Notices of the Royal Astronomical Society, 418, 2234

[23] Bonafede A., et al., 2012, Monthly Notices of the Royal Astronomical Society, 426, 40

[24] Bonafede A., Vazza F., Brüggen M., Murgia M., Govoni F., Feretti L., Giovannini G., Ogrean G., 2013, Monthly Notices of the Royal Astronomical Society, 433, 3208

[25] Bonafede A., et al., 2014, Monthly Notices of the Royal Astronomical Society: Letters, 444, L44–L48

[26] Bonafede A., et al., 2015, Unravelling the origin of large-scale magnetic fields in galaxy clusters and beyond through Faraday Rotation Measures with the SKA (arXiv:1501.00321)

[27] Bonafede A., et al., 2017, Monthly Notices of the Royal Astronomical Society, 470, 3465

[28] Botteon A., et al., 2020, Monthly Notices of the Royal Astronomical Society: Letters, 499, L11

[29] Botteon A., et al., 2022, Science Advances, 8, eabq7623

[30] Bravi L., Gitti M., Brunetti G., 2016, Monthly Notices of the Royal Astronomical Society, 455, L41

[31] Brentjens M. A., de Bruyn A. G., 2005, Astronomy & Astrophysics, 441, 1217–1228

[32] Briggs D. S., 1995, PhD thesis, New Mexico Institute of Mining and Technology

[33] Brownstein J. R., Moffat J. W., 2007, Monthly Notices of the Royal Astronomical Society, 382, 29

[34] Brunetti G., Lazarian A., 2007, Monthly Notices of the Royal Astronomical Society, 378, 245

[35] Brunetti G., Setti G., Feretti L., Giovannini G., 2001, Monthly Notices of the Royal Astronomical Society, 320, 365

[36] Bruno L., et al., 2023, Astronomy & Astrophysics, 678, A133

[37] Bruno L., et al., 2024, Ageing and dynamics of the tailed radio galaxies in Abell 2142 (arXiv:2409.03453)

[38] Burn B. J., 1966, Monthly Notices of the Royal Astronomical Society, 133, 67

[39] Böhringer H., 2014, Memorie della Società Astronomica Italiana, 85, 396

[40] Böhringer H., Werner N., 2010, The Astronomy and Astrophysics Review, 18, 127

[41] Böhringer H., Chon G., Kronberg P. P., 2016, Astronomy & Astrophysics, 596, A22

[42] Calzadilla M. S., et al., 2023, The SPT-Chandra BCG Spectroscopic Survey I: Evolution of the Entropy Threshold for Cooling and Feedback in Galaxy Clusters Over the Last 10 Gyr (arXiv:2311.00396)

[43] Carlstrom J. E., Holder G. P., Reese E. D., 2002, Annual Review of Astronomy and Astrophysics, 40, 643–680

[44] Carretti E., et al., 2022, Monthly Notices of the Royal Astronomical Society, 512, 945

[45] Cavagnolo K. W., Donahue M., Voit G. M., Sun M., 2009, The Astrophysical Journal Supplement, 182, 12

[46] Cavaliere A., Fusco-Femiano R., 1976, Astronomy & Astrophysics, 49, 137

[47] Cavaliere A., Fusco-Femiano R., 1978, Astronomy & Astrophysics, 70, 677

[48] Cheng B., Olinto A. V., Schramm D. N., Truran J. W., 1996, Physical Review D, 54, 4714

[49] Clark B. G., 1980, Astronomy & Astrophysics, 89, 377

[50] Clarke T. E., 2004, Journal of The Korean Astronomical Society, 37, 337

[51] Clarke T. E., Kronberg P. P., Böhringer H., 2001, The Astrophysical Journal, 547, L111

[52] Collett E., 2005, Field Guide to Polarization. SPIE Press

[53] Collins C., et al., 2009, Nature, 458, 603

[54] Condon J., Ransom S. M., 2016, Essential radio astronomy. Vol. 2, Princeton University Press

[55] Cornwell T. J., 2008, IEEE Journal of Selected Topics in Signal Processing, 2, 793–801

[56] Cuciti V., et al., 2022, Nature, 609, 911–914

[57] De Grandi S., Molendi S., 2001, The Astrophysical Journal, 551, 153

[58] De Grandi S., Santos J. S., Nonino M., Molendi S., Tozzi P., Rossetti M., Fritz A., Rosati P., 2014, Astronomy & Astrophysics, 567, A102

[59] De Rubeis E., Stuardi C., Bonafede A., Vazza F., van Weeren R. J., de Gasperin F., Brüggen M., 2024, Magnetic fields in the outskirts of PSZ2 G096.88+24.18 from depolarization analysis of radio relics (arXiv:2408.08603)

[60] Di Gennaro G., et al., 2020, Nature Astronomy, 5, 268–275

[61] Dolag K., Ensslin T. A., 2000, Radio Halos of Galaxy Clusters from Hadronic Secondary Electron Injection in Realistic Magnetic Field Configurations (arXiv:astro-ph/0008333)

[62] Dolag K., Grasso D., Springel V., Tkachev I., 2005, Journal of Cosmology and Astroparticle Physics, 2005, 009–009

[63] Dolag K., Bykov A. M., Diaferio A., 2008, Space Science Reviews, 134, 311–335

[64] Domínguez-Fernández P., Vazza F., Brüggen M., Brunetti G., 2019, Monthly Notices of the Royal Astronomical Society, 486, 623

[65] Donnert J., Dolag K., Lesch H., Müller E., 2009, Monthly Notices of the Royal Astronomical Society, 392, 1008

[66] Donnert J., Vazza F., Brüggen M., ZuHone J., 2018, Space Science Reviews, 214

[67] Dressler A., 1980, The Astrophisical Journal, 236, 351

[68] Durrer R., Neronov A., 2013, The Astronomy and Astrophysics Review, 21

[69] Eckert D., et al., 2014, Astronomy & Astrophysics, 570, A119

[70] Edge A., 2001, Monthly Notices of the Royal Astronomical Society, 328, 762

[71] Eilek J. A., Owen F. A., 2002, The Astrophysical Journal, 567, 202

[72] Einasto M., et al., 2015, The Astrophysical Journal, 580, A69

[73] Ensslin T. A., Biermann P. L., Klein U., Kohle S., 1997, Cluster Radio Relics as a Tracer of Shock Waves of the Large-Scale Structure Formation (arXiv:astro-ph/9712293)

[74] Ettori S., Fabian A. C., 1999, Monthly Notices of the Royal Astronomical Society, 305, 834–848

[75] Ettori S., Ghirardini V., Eckert D., Dubath F., Pointecouteau E., 2017, Monthly Notices pf the Royal Astronomycal Society, 470, L29

[76] Fabian A. C., 1994, Annual Review of Astronomy and Astophysics, 32, 277

[77] Fabian A. C., et al., 2000, Monthly Notices of the Royal Astronomical Society, 318, L65

[78] Fabian A. C., Sanders J. S., Taylor G. B., Allen S. W., Crawford C. S., Johnstone R. M., Iwasawa K., 2006, Monthly Notices of the Royal Astronomical Society, 366, 417–428

[79] Fanaroff B. L., Riley J. M., 1974, Monthly Notices of the Royal Astronomical Society, 167, 31P

[80] Farnsworth D., Rudnick L., Brown S., Brunetti G., 2013, The Astrophysical Journal, 779, 189

[81] Felten J. E., 1996, in Trimble V., Reisenegger A., eds, Astronomical Society of the Pacific Conference Series Vol. 88, Clusters, Lensing, and the Future of the Universe. p. 271

[82] Felten J. E., Gould R. J., Stein W. A., Woolf N. J., 1966, The Astrophysical Journal, 146, 955

[83] Feretti L., Brunetti G., Giovannini G., Kassim N., Orru E., Setti G., 2004, Journal of Korean Astronomical Society, 37, 315

[84] Feretti L., Giovannini G., Govoni F., Murgia M., 2012, The Astronomy and Astrophysics Review, 20, 54

[85] Fine M. A., Van Eck C. L., Pratley L., 2023, Monthly Notices of the Royal Astronomical Society, 520, 4822–4835

[86] Fixsen D. J., 2009, The Astrophysical Journal, 707, 916

[87] Forman W., Bechtold J., Blair W., Giacconi R., Van Speybroeck L., Jones C., 1981, The Astrophysical Journal, 243, L133

[88] Gardner F. F., Daviest R. D., 1966, Australian Journal of Physics, 19, 441

[89] Gardner F. F., Whiteoak J. B., 1966, Annual Review of Astronomy and Astrophysics, 4, 245

[90] Garrington S. T., Leahy J. P., Conway R. G., Laingt R. A., 1988, Nature, 331, 147

[91] Gendron-Marsolais M., et al., 2017, Monthly Notices of the Royal Astronomical Society, 469, 3872

[92] George S. J., Stil J. M., Keller B. W., 2012, Publications of the Astronomical Society of Australia, 29, 214–220

[93] Ghirardini V., et al., 2019, Astronomy & Astrophysics, 621, A41

[94] Giacintucci S., Markevitch M., Venturi T., Clarke T. E., Cassano R., Mazzotta P., 2014, The Astrophysical Journal, 781, 9

[95] Giacintucci S., Markevitch M., Cassano R., Venturi T., Clarke T. E., Kale R., Cuciti V., 2019, The Astrophysical Journal, 880, 70

[96] Giovannini M., Shaposhnikov M., 2000, Physical Review D, 62, 103512

[97] Giovannini G., Tordi M., Feretti L., 1999, New Astronomy, 4, 141

[98] Giovannini G., Bonafede A., Feretti L., Govoni F., Murgia M., Ferrari F., Monti G., 2009, Astronomy & Astrophysics, 507, 1257

[99] Gitti M., 2016, Radio mini-halos and AGN heating in cool core clusters of galaxies (arXiv:1602.08312)

[100] Gitti M., Brunetti G., Setti G., Feretti L., 2002, Modeling radio mini-halos in cooling flow clusters (arXiv:astro-ph/0207145)

[101] Gitti M., Brunetti G., Feretti L., Setti G., 2004, The Astrophysical Journal, 417, 1

[102] Gnedin N. Y., Ferrara A., Zweibel E. G., 2000, The Astrophysical Journal, 539, 505

[103] Gorenstein P., Fabricant D., Topka K., Harnden F. R. J., Tucker W. H., 1978, The Astrophysical Journal, 224, 718

[104] Govoni F., Ferretti L., 2004, International Journal of Modern Physics D, 13, 1549–1594

[105] Govoni F., Ensslin T., Feretti L., Giovannini G., 2001, Astronomy & Astrophysics, 369, 441

[106] Govoni F., Murgia M., Feretti L., Giovannini G., Dolag K., Taylor G. B., 2006, Astronomy & Astrophysics, 460, 425

[107] Govoni F., et al., 2010, Astronomy & Astrophysics, 522, A105

[108] Govoni F., et al., 2017, Astronomy & Astrophysics, 603, A122

[109] Gu M., Conroy C., Brammer G., 2018, The Astrophysical Journal Letters, 862, L18

[110] Guidetti D., Murgia, M. Govoni, F. Parma, P. Gregorini, L. de Ruiter, H. R. Cameron, R. A. Fanti, R. 2008, Astronomy & Astrophysics, 483, 699

[111] Gunn J. E., Gott J. R. I., 1972, The Astrophisical Journal, 176, 1

[112] Ha J., Ryu D., Kang H., 2018, The Astrophysical Journal, 857, 26

[113] Hales C. A., Gaensler B. M., Norris R. P., Middelberg E., 2012, Monthly Notices of the Royal Astronomical Society, 424, 2160

[114] Hayashi E., White S. D. M., 2006, Monthly Notices of the Royal Astronomical Society: Letters, 370, L38

[115] Heald G., 2009, Proceedings of the International Astronomical Union, 4, 591–602

[116] Henning J. W., Gantner B., Burns J. O., Hallman E. J., 2009, The Astrophysical Journal, 697, 1597–1620

[117] Henry J. P., Briel U. G., 1996, The Astrophysical Journal, 472, 137

[118] Hoffer A. S., Donahue M., Hicks A., Barthelemy R. S., 2012, The Astrophysical Journal Supplement Series, 199, 23

[119] Högbom J. A., 1974, Aperture Synthesis with a Non-Regular Distribution of Interferometer Baselines

[120] Hubble E. P., 1936, Realm of the Nebulae

[121] Hudson D. S., Mittal R., Reiprich T. H., Nulsen P. E. J., Andernach H., Sarazin C. L., 2010, Astronomy & Astrophysics, 513, A37

[122] Hutschenreuter S., et al., 2022, Astronomy & Astrophysics, 657, A43

[123] Iapichino L., Brüggen M., 2012, Monthly Notices of the Royal Astronomical Society, 423, 2781

[124] Ignesti A., Brunetti G., Gitti M., Giacintucci S., 2020, Astronomy & Astrophysics, 640, A37

[125] Johnston-Hollitt M., et al., 2015, Using SKA Rotation Measures to Reveal the Mysteries of the Magnetised Universe (arXiv:1506.00808)

[126] Jones C., Forman W., 1978, The Astrophysical Journal, 224, 1

[127] Kaastra J. S., Ferrigno C., Tamura T., Paerels F. B. S., Peterson J. R., Mittaz J. P. D., 2001, Astronomy & Astrophysics, 365, L99

[128] Kahniashvili T., Tevzadze A. G., Brandenburg A., Neronov A., 2013, Physical Review D, 87, 083007

[129] Kennicutt R. C. J., 1992, Astrophysical Journal Supplement, 79, 255

[130] King I., 1962, The Astrophysical Journal, 67, 471

[131] Kolmogorov A. N., 1991, Proceedings of the Royal Society of London. Series A: Mathematical and Physical Sciences, 434, 9

[132] Kravtsov A. V., Borgani S., 2012, Annual Review of Astronomy and Astrophysics, 50, 353–409

[133] Krick J. E., Bernstein R. A., Pimbblet K. A., 2006, The Astronomical Journal, 131, 168–184

[134] Laing R. A., 1988, Nature, 331, 149

[135] Langer M., Aghanim N., Puget J. L., 2005, Astronomy & Astrophysics, 443, 367–372

[136] Large M. I., Mathewson D. S., Haslam C. G. T., 1959, Nature, 183, 1663

[137] Lauer T. R., Postman M., Strauss M. A., Graves G. J., Chisari N. E., 2014, The Astrophysical Journal, 797, 82

[138] Lin Y.-T., Mohr J. J., Stanford S. A., 2003, The Astrophysical Journal, 591, 749

[139] Liu A., Yu H., Diaferio A., Tozzi P., Hwang H. S., Umetsu K., Okabe N., Yang L.-L., 2018, The Astrophysical Journal, 863, 102

[140] Liu A., Zhai M., Tozzi P., 2019, Monthly Notices of the Royal Astronomical Society, 485, 1651

[141] Longair M. S., 2011, High Energy Astrophysics

[142] Malyshkin L., 2001, The Astrophysical Journal, 554, 561–570

[143] Markevitch M., et al., 2000, The Astrophysical Journal, 541, 542

[144] Markevitch M., Gonzalez A. H., David L., Vikhlinin A., Murray S., Forman W., Jones C., Tucker W., 2002, The Astrophysical Journal, 567, L27

[145] McNamara B., Nulsen P., 2007, Annual Review of Astronomy and Astrophysics, 45, 117–175

[146] Mitchell R. J., Culhane J. L., Davison P. J. N., Ives J. C., 1976, Monthly Notices of the Royal Astronomical Society, 175, 29P

[147] Molendi S., Pizzolato F., 2001, The Astrophysical Journal, 560, 194

[148] Munari E., Biviano A., Mamon G. A., 2014, Astronomy & Astrophysics, 566, A68

[149] Murgia M., Govoni F., Feretti L., Giovannini G., Dallacasa D., Fanti R., Taylor G. B., Dolag K., 2004, Astronomy & Astrophysics, 424, 429–446

[150] Murgia M., Govoni F., Markevitch M., Feretti L., Giovannini G., Taylor G., Carretti E., 2009, Astronomy & Astrophysics, 499, 679

[151] Oegerle W. R., Hill J. M., Fitchett M. J., 1995, The Astrophysical Journal, 110, 32

[152] Oemler A., 1977, Highlights of Astronomy, 4, 253–260

[153] Offringa A. R., Smirnov O., 2017, Monthly Notices of the Royal Astronomical Society, 471, 301–316

[154] Offringa A. R., et al., 2014, Monthly Notices of the Royal Astronomical Society, 444, 606–619

[155] Okabe N., Umetsu K., 2008, Publications of the Astronomical Society of Japan, 60, 345

[156] Osinga E., et al., 2022, Astronomy & Astrophysics, 665, A71

[157] Owen F. N., Rudnick L., 1976, The Astrophysical Journal, 205, L1

[158] Owers M. S., Nulsen P. E. J., Couch W. J., 2011, The Astrophysical Journal, 741, 122

[159] Pearce C. J. J., et al., 2017, The Astrophysical Journal, 845, 81

[160] Peres C. B., Fabian A. C., Edge A. C., Allen S. W., Johnstone R. M., White D. A., 1998, Monthly Notices of the Royal Astronomical Society, 298, 416

[161] Perlicki K., 2015, in Yasin M., Arof H., Harun S. W., eds, , Advances in Optical Fiber Technology. IntechOpen, Chapt. 4, doi:10.5772/59000

[162] Peterson J. R., Kahn S. M., Paerels F. B. S., Kaastra J. S., Tamura T., Bleeker J. A. M., Ferrigno C., Jernigan J. G., 2003, The Astrophysical Journal, 590, 207

[163] Pfrommer C., Enßlin T. A., 2004, Astronomy & Astrophysics, 413, 17

[164] Pignataro G. V., Bonafede A., Bernardi G., Riseley C. J., Dallacasa D., Venturi T., 2024, Astronomy & Astrophysics, 682, A105

[165] Planck Collaboration et al., 2011, Astronomy & Astrophysics, 536, A8

[166] Planck Collaboration et al., 2016, Astronomy & Astrophysics, 594, A27

[167] Poopakun K., Kriwattanawong W., 2019, Journal of Physics: Conference Series, 1380, 012064

[168] Pratt G. W., Böhringer H., Croston J. H., Arnaud M., Borgani S., Finoguenov A., Temple R. F., 2007, Astronomy & Astrophysics, 461, 71

[169] Rafferty D. A., McNamara B. R., Nulsen P. E. J., 2008, The Astrophysical Journal, 687, 899

[170] Rajpurohit K., et al., 2022, The Astrophysical Journal, 927, 80

[171] Rephaeli Y., Sadeh S., Shimon M., 2006, Nuovo Cimento Rivista Serie, 29, 1

[172] Reynolds C. S., David Marsh M. C., Russell H. R., Fabian A. C., Smith R., Tombesi F., Veilleux S., 2020, The Astrophysical Journal, 890, 59

[173] Riseley C. J., et al., 2024, Astronomy & Astrophysics, 686, A44

[174] Roberg-Clark G. T., Drake J. F., Reynolds C. S., Swisdak M., 2016, The Astrophysical Journal, 830, L9

[175] Roettiger K., Stone J. M., Burns J. O., 1999, The Astrophysical Journal, 518, 594

[176] Rossetti M., Molendi S., 2004, Astronomy & Astrophysics, 414, L41

[177] Rossetti M., Eckert D., De Grandi S., Gastaldello F., Ghizzardi S., Roediger E., Molendi S., 2013, Astronomy & Astrophysics, 556, A44

[178] Rossetti M., et al., 2016, Monthly Notices of the Royal Astronomical Society, 457, 4515

[179] Rudnick L., Owen F. N., 2014, The Astrophysical Journal, 785, 45

[180] Ruszkowski M., Begelman M. C., 2002, The Astrophysical Journal, 573, 485

[181] Rybicki G. B., Lightman A. P., 1986, Radiative Processes in Astrophysics

[182] Ryle M., Windram M. D., 1968, Monthly Notices of the Royal Astronomical Society, 138, 1

[183] Ryu D., Kang H., Cho J., Das S., 2008, Science, 320, 909

[184] Ryu D., Schleicher D. R., Treumann R. A., Tsagas C. G., Widrow L. M., 2012, Space Science Reviews, 166, 1

[185] Saikia D. J., Salter C. J., 1988, Annual Review of Astronomy and Astrophysics, 26, 93

[186] Sanders J. S., Fabian A. C., Churazov E., Schekochihin A. A., Simionescu A., Walker S. A., Werner N., 2013, Science, 341, 1365–1368

[187] Santos J. S., Tozzi P., Rosati P., Böhringer H., 2010, Astronomy & Astrophysics, 521, A64

[188] Sarazin C. L., 1988, X-ray emission from clusters of galaxies

[189] Schaefer B., Collett E., Smyth R., Barrett D., Fraher B., 2007, American Journal of Physics, 75, 163

[190] Schwab F., 1984, in Roberts J. A., ed., Indirect Imaging. Measurement and Processing for Indirect Imaging. pp 333–346

[191] Sokoloff D. D., Bykov A. A., Shukurov A., Berkhuijsen E. M., Beck R., Poezd A. D., 1998, Monthly Notices of the Royal Astronomical Society, 299, 189

[192] Spitzer L., Greenstein J. L., 1951, Astrophysical Journal, 114, 407

[193] Strateva I., et al., 2001, The Astronomical Journal, 122, 1861

[194] Stuardi C., Bonafede A., Lovisari L., Domínguez-Fernández P., Vazza F., Brüggen M., van Weeren R. J., de Gasperin F., 2021, Monthly Notices of the Royal Astronomical Society, 502, 2518

[195] Subramanian K., 2016, Reports on Progress in Physics, 79, 076901

[196] Sunyaev R. A., 1977, Soviet Astronomy Letters, 3, 268

[197] Sunyaev R. A., Zel'dovich Y. B., 1972, Comments on Astrophysics and Space Physics, 4, 173

[198] Sunyaev R. A., Zel'dovich Y. B., 1980, Annual Review of Astronomy and Astrophysics, 18, 537

[199] Taylor A. R., Stil J. M., Sunstrum C., 2009, The Astrophysical Journal, 702, 1230

[200] Tchernin C., et al., 2016, Astronomy & Astrophysics, 595, A42

[201] Thompson A. R., Moran J. M., Swenson G. W. J., 2017, Interferometry and Synthesis in Radio Astronomy, 3rd Edition

[202] Tinbergen J., 1996, Astronomical Polarimetry. Cambridge University Press

[203] Tribble P. C., 1991, Monthly Notices of the Royal Astronomical Society, 250, 726

[204] Trippe S., 2014, Journal of The Korean Astronomical Society, 47, 15

[205] Tucker W. H., Tananbaum H., Remillard R. A., 1995, The Astrophysical Journal, 444, 532

[206] Ubertosi F., Gitti M., Brighenti F., Olivares V., O'Sullivan E., Schellenberger G., 2023, Astronomy & Astrophysics, 673, A52

[207] Vacca V., Murgia M., Govoni F., Feretti L., Giovannini G., Orrù E., Bonafede A., 2010, Astronomy & Astrophysics, 514, A71

[208] Vacca V., Murgia M., Govoni F., Feretti L., Giovannini G., Perley R. A., Taylor G. B., 2012, Astronomy & Astrophysics, 540, A38

[209] Vazza F., Brüggen M., Gheller C., Wang P., 2014, Monthly Notices of the Royal Astronomical Society, 445, 3706

[210] Vazza F., Brüggen M., Gheller C., Hackstein S., Wittor D., Hinz P. M., 2017, Classical and Quantum Gravity, 34, 234001

[211] Vazza F., Brunetti G., Brüggen M., Bonafede A., 2018, Monthly Notices of the Royal Astronomical Society, 474, 1672

[212] Venturi T., et al., 2017, Astronomy & Astrophysics, 603, A125

[213] Vikhlinin A., Markevitch M., Murray S. S., Jones C., Forman W., Van Speybroeck L., 2005, The Astrophysical Journal, 628, 655

[214] Vikhlinin A., Kravtsov A., Forman W., Jones C., Markevitch M., Murray S. S., Van Speybroeck L., 2006, The Astrophysical Journal, 640, 691

[215] Vogt C., Enßlin T. A., 2003, Astronomy & Astrophysics, 412, 373

[216] Wang Q. H. S., Markevitch M., 2018, The Astrophysical Journal, 868, 45

[217] Wardle J. F. C., Kronberg P. P., 1974, Astrophysical Journal, 194, 249

[218] Westfold K., 1959, The Astrophysical Journal, 130, 241

[219] Wik D. R., et al., 2014, The Astrophysical Journal, 792, 48

[220] Xu H., O'Shea B. W., Collins D. C., Norman M. L., Li H., Li S., 2008, The Astrophysical Journal, 688, L57

[221] Xu H., Li H., Collins D. C., Li S., Norman M. L., 2011, The Astrophysical Journal, 739, 77

[222] Zwicky F., 1933, Helv. Phys. Acta, 6, 110

[223] de Gasperin F., van Weeren R. J., Brüggen M., Vazza F., Bonafede A., Intema H. T., 2014, Monthly Notices of the Royal Astronomical Society, 444, 3130

[224] van Weeren R. J., Röttgering H. J. A., Brüggen M., Cohen A., 2009, Astronomy & Astrophysics, 505, 991

[225] van Weeren R. J., Roettgering H. J. A., Brueggen M., Hoeft M., 2010, Science, 330, 347

[226] van Weeren R. J., Brüggen M., Röttgering H. J. A., Hoeft M., 2011a, Monthly Notices of the Royal Astronomical Society, 418, 230

[227] van Weeren R. J., Hoeft M., Rottgering H. J. A., Bruggen M., Intema H. T., van Velzen S., 2011b, Astronomy & Astrophysics, 528, A38

[228] van Weeren R. J., de Gasperin F., Akamatsu H., Brüggen M., Feretti L., Kang H., Stroe A., Zandanel F., 2019, Space Science Reviews, 215